Institute of Physics
Fluminense Federal University

Ph.D. Thesis

Spin-Orbit Coupling Effect over Kondo Temperature and Thermoelectric Transport Properties of a Quantum Dot

---

by

Marco Antonio Manya Suni

Supervisor: **Dr. Marcos Sergio Figueira da Silva**
Co-Supervisor: **Dr. George Balster Martins**

November, 2021

Ficha catalográfica automática - SDC/BIF
Gerada com informações fornecidas pelo autor

M266s Manya suni, Marco Antonio
Spin-Orbit Coupling Effect over Kondo Temperature and Thermoelectric Transport Properties of a Quantum Dot : Spin-Orbit Coupling Effect over Kondo Temperature and Thermoelectric Transport Properties of a Quantum Dot / Marco Antonio Manya suni ; Marcos Sergio Da Silva, orientador ; George Balster Martins, coorientador. Niterói, 2021.
114 f.

Tese (doutorado)-Universidade Federal Fluminense, Niterói, 2021.

DOI: http://dx.doi.org/10.22409/PPGF.2021.d.07226885123

1. Spin-Orbit coupling. 2. Kondo effect. 3. Seebeck effect. 4. Wiedemann-Franz Law. 5. Produção intelectual. I. Da Silva, Marcos Sergio, orientador. II. Martins, George Balster, coorientador. III. Universidade Federal Fluminense. Instituto de Física. IV. Título.

CDD -

Bibliotecário responsável: Debora do Nascimento - CRB7/6368

INSTITUTO DE FÍSICA
Universidade Federal Fluminense
CURSO DE PÓS-GRADUAÇÃO EM FÍSICA
RUA GAL MILTON TAVARES DE SOUZA, SN
24210-346 – NITERÓI - RIO DE JANEIRO
TEL: (21)2629-5878 - FAX: 2629-5887
E-MAIL: cpg@ if.uff.br

Ata dos trabalhos finais da Comissão Examinadora da tese de doutorado apresentada por **Marco Antonio Manya Suni**. No terceiro dia do mês de novembro de dois mil e vinte e um, às quatorze horas, reuniram-se de forma remota, os membros da Comissão Examinadora constituída pelos professores doutores Marcos Sergio Figueira da Silva(IF/UFF), Andrea Brito Latgé (IF-UFF), Antonio Carlos Ferreira Seridonio (UNESP), Caio Henrique Lewenkopf (IF-UFF) e Ginetom Souza Diniz (UFJ); sob a presidência do primeiro, para prova pública de apresentação de tese de doutorado intitulada ***"Spin-Orbit Coupling Effect over Kondo Temperature and Thermoelectric Transport Properties of a Quantum Dot",*** tendo em vista as exigências do Regulamento Específico do curso de Física relacionadas com a conclusão do Doutorado em Física pela Universidade Federal Fluminense. A tese foi elaborada sob a orientação do professor Marcos Sergio Figueira da Silva e coorientação do Prof. George Balster Martins. Após a exposição do trabalho, o aluno respondeu às questões formuladas pelos integrantes da Comissão Examinadora, que apresentou parecer no sentido de aprová-lo. Para constar, foi lavrada a presente ata, que vai assinada pelos membros da Comissão Examinadora e pelo doutorando.

Niterói, três de novembro de dois mil e vinte e um.

Dr. Marcos Sergio Figueira da Silva 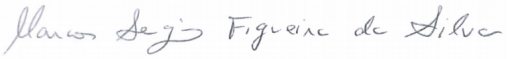

Dr.ª Andrea Brito Latgé 

Dr. Antonio Carlos Ferreira Seridonio 

Dr. Caio Henrique Lewenkopf 

Dr. Ginetom Souza Diniz 

Marco Antonio Manya Suni 

Tukuysonqoymanta, Taytaypaq Mamaypaqwan

Acknowledgements

First of all, I would like to thank God for allowing me this wonderful experience and meeting people full of charisma during my journey through Brazil. Right away, I would like to thank my advisor, Prof. Marcos Sergio Figueira, and my co-advisor Prof. Geroge Balster Martins. Both are truly great people and are a great example for me of how to be a scientist. I would like to thank them for believing in my potential and for giving me the opportunity to continue with my study. For their patience on the way to post-graduation despite my difficulties. It is great luck to have met them, for having taught me to enjoy science. I would also like to thank professor Zitko, author of the NRG Ljubljana program for the help whenever there is a difficulty in the program, professor Edson Vernek for his availability for physical discussions and with the NRG program, and how not to thank professor Enrique Anda also for the availability for the physical discussions of the problem.

I thank my family, everyone really, for having made this postgraduate trip possible outside my country. I thank my parents Dominga and Antonio, for being the main actors for me to reach this wonderful Brazil, my brother Nilson for his generosity and unconditional support, sister Maritza for that affection and for having believed in me, and finally my cousin Manuel, to each and every one of them I am infinitely grateful.

And finally, I would also like to thank the professors and the friends of the university who have directly or indirectly contributed and are contributing to my formation.

Thank you so much, everybody!

Abstract

Spin-Orbit Coupling Effect over Kondo Temperature and Thermoelectric Transport Properties of a Quantum Dot

This thesis presents the research results of a quantum dot coupled to a conduction band with spin-orbit coupling (SOC), Specifically, a simgle electron transistor (SET). We study the dependence of the Kondo temperature and the thermoelectric transport properties with SOC. The problem is modeled as a single impurity Anderson model in the presence of the conduction band spin-orbit interaction. The SOC mixes the spins of the conducting electrons, and as a consequence, the SU(2) spin symmetry of the Anderson Hamiltonian is broken. We recover the Anderson Hamiltonian SU(2) symmetry through a rotation of the system's spins along with $\hat{r}$ axis, where the ground state of the problem can be considered the Kondo many-body singlet state. On this quantization axis, the Anderson Hamiltonian can be rewritten in the same way as the original Anderson Hamiltonian, with which we obtain a continuous density of states of the conduction band, a diagonal hybridization function on the spin rotated basis, and that the Haldane formula for the Kondo temperature can be rewritten, renormalized by the conduction band SOC.

In the study of thermoelectric transport properties, we observe that in both: the atomic and the numerical renormalization group (NRG) methods, the Kondo temperature decreases with the increasing of the SOC. It is because the Friedel sum rule is satisfied under conduction band SOC. In the transport properties, we obtain that the electrical, thermal conductance, and thermopower exhibit universality in the presence of spin-orbit coupling. Similarly, we observe the violation of the Wiedemann-Franz law, and the figure of merit ZT increases with the presence of de conduction band SOC. In short, the SOC interaction drives the system to the Kondo regime.

Abstract

Efeito do acoplamento spin-órbita sobre a temperatura Kondo e propriedades de transporte termoelétrico de um ponto quântico

Esta tese apresenta os resultados da pesquisa de um ponto quântico acoplado a uma banda de condução com acoplamento spin-órbita (SOC). Estudamos a dependência da temperatura de Kondo e as propriedades de transporte termoelétrico com este tipo de SOC. O problema é modelado como um modelo de Anderson de impureza única na presença da interação spin-órbita da banda de condução. O SOC mistura os spins dos elétrons de condução e, como consequência, a simetria do spin SU (2) do hamiltoniano de Anderson é quebrada. Recuperamos a simetria SU (2) da hamiltoniana de anderson por meio de uma rotação dos spins do sistema junto com o eixo $\hat{r}$, onde o estado fundamental do problema pode ser considerado como sendo o estado singlete de muitos corpos de Kondo. Neste eixo de quantização, o Hamiltoniano de Anderson pode ser reescrito da mesma forma que o hamiltoniano de Anderson original, com o qual obtemos uma densidade contínua de estados da banda de condução, uma função de hibridização diagonal com base na rotação de spin, e que a fórmula de Haldane para a temperatura Kondo pode ser reescrita, renormalizada pela banda de condução SOC.

No estudo das propriedades de transporte termoelétrico, observamos que em ambos: o método atômico e o método NRG, a temperatura de Kondo diminui com o aumento do SOC. Isso ocorre devido a satisfação da regra da soma de Friedel na presença da banda de condução SOC. Nas propriedades de transporte, obtemos que as condutâncias elétrica e térmica, assim comoa termopotência exibem universalidade na presença de acoplamento spin-órbita. Da mesma forma, observamos a violação da lei de Wiedemann-Franz, e um aumento do ZT com a presença da banda de condução SOC. Resumindo, a interação do SOC conduz o sistema ao regime de Kondo.

Contents

List of Figures

Chapter 1

Introduction

The enormous growth of technology in the last 20 years has led to the construction of electronic devices of increasingly smaller sizes, more sophisticated, and efficient. These reduced-size devices are quantum dots (QD), quantum wires (QW), and the quantum wells, commonly called nanostructures. The physical properties of the nanoscopic systems due to their nanometric scale exhibits quantum confinement effects. Moreover, experimentally, it has been shown that their mechanical, optical, and transport properties become size dependent [9]. In a correlated QD, it is possible to attain complete control of all the Kondo impurity problem parameters [10].

Thermoelectricity began with the discovery of the Seebeck and Peltier effects [11] that evolved slowly in trying to realize the dream of transforming thermal energy directly into electrical energy in an effective way. The Seebeck effect Figure 1.1a generates a bias voltage when two different metallic surfaces, at different temperatures, are put into contact, and the Peltier effect Figure 1.1b is associated with heat absorption or rejection when an electric current flows through a Seebeck device.

The Peltier and Seebeck effects constitute the basis for many thermoelectric (TE) generators (TEGs) and cooling (TECs) devices, respectively [12–14]. Since its discovery [15], the narrow-gap layered Bi_2Te_3 compound, when alloyed with antimony or selenium, has been employed as the basic material for TEGs and TECs at room temperature. In the last years, it was experimentally shown that Bi_2Te_3 is a three-dimensional topological insulator with a single Dirac cone on its surface [16]. Other good TE materials are also topological insulators, like Bi_2Se_3, Sb_2Te_3, and $FeSb_2$ [17–

20]. The topological nature of these materials can shed some light on their TE properties because most of their behavior is due to strong spin-orbit coupling [21, 22] or their conducting surface states [23–25].

Until now, the use of TE devices has been confined to low-power energy generation applications, where the advantages of not having movable parts, which increases the TE device lifetime by avoiding maintenance, compensates for their low efficiency and higher cost [26]. In addition, TE devices can be employed as auxiliary systems to recover the heat wasted in traditional large-scale electrical energy generation systems that employ natural gas, fossil fuels, coal, and nuclear power, and thus help to control pollution and waste of dangerous chemical products, which are hazardous to the environment [27]. The importance of direct conversion between thermal and electrical energy employing TE devices has increased continuously, and there are some niche applications where TE devices are dominant. One recent use of TE devices is wearable and implanted medical devices that exploit body heat as an energy source. Generally, these devices are composed of two parts: an interface between the skin and the TEG module and a thermal sink to dissipate heat to the air [27]. Another recent application of TEGs is to convert the heat wasted in industrial machinery or vehicles into electrical energy. In a vehicle, this energy could be used to power its electrical devices and improve engine performance. Another application of TECs is to act as a cooling device for high-performance CPU processors, where a Bi_2Te_3 TEC module is placed between the hot spot of the processor and an air-cooled heat sink [28].

Then, a thermoelectric module is a complex thermoelectric device [1] such as illustrated in Figure 1.1. It consists of many thermocouples connected electrically in series and thermally in parallel by a metallic contact. A thermocouple is composed of n-type and p-type semiconductors whose Seebeck coefficients are negative and positive, respectively. The thermocouple comprises two modes, power generating mode and refrigeration mode. In the first case, charge carriers flow from the hot to the cold side due to the applied gradient temperature, Figure 1.1(a). However, in the second case, the charge carriers flow due to applied electrical voltage, Figure 1.1(b). Therefore, the state-of-the-art thermoelectric devices are built containing many thousand thermocouples, whose electrical and thermal properties are controlled by adjusting the number of thermocouples according to their application [1, 29].

At the beginning of the 1990s, the research field of thermoelectric materials was expanded into low-dimensional electron systems, and it has been reported the improve-

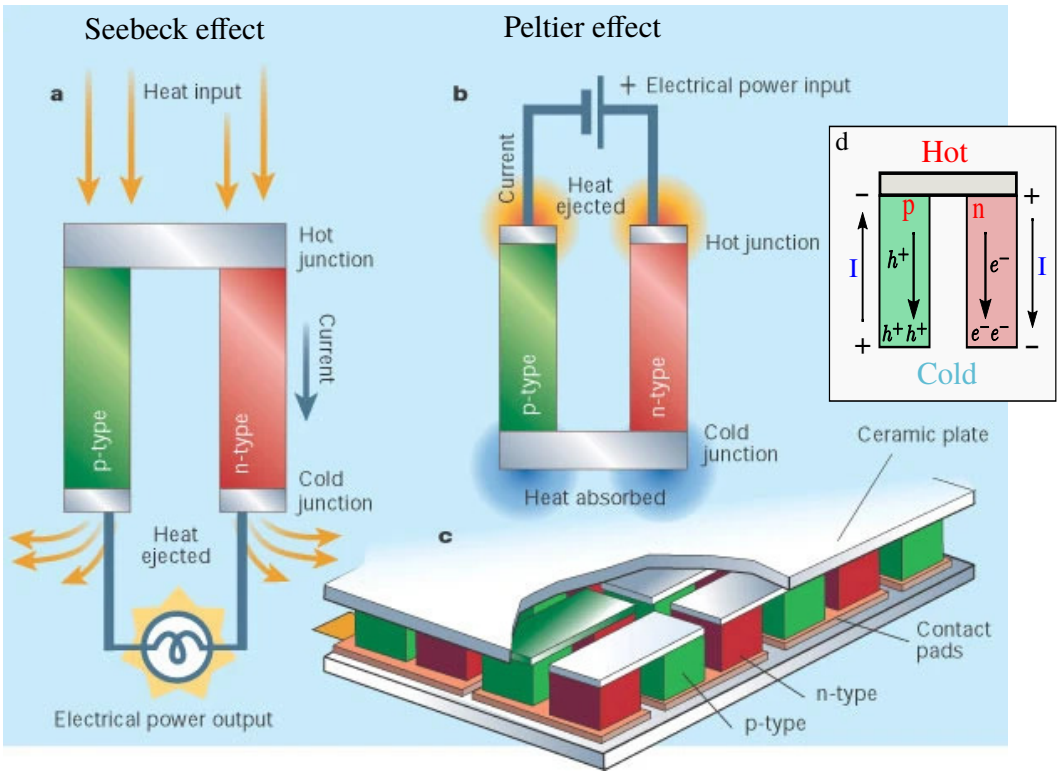

Figure 1.1: Thermoelectric couple [1] application in a thermocouple. (a) power generation mode (Seebeck effect), (b) Refrigeration mode (Peltier effect), (c) is a thermocouple device, and (d) Direction of charge carriers when the ends of p- and n-type semiconductors are under different temperatures.

ment of the figure of merit ZT in quantum wells [30] and a quantum wires [31]. This discovery opened a new path in researching high-performance thermoelectric devices based on quantum structures that make it possible to take advantage of quantum effects due to their sizes. Nowadays, quantum structures, mainly quantum dots, enjoy great popularity in the field of thermoelectricity. Since then, in the last years, the interest in the TE properties of QDs has greatly increased, yielding several papers, originating from theoretical [8, 32–40] as well as experimental groups [41–49]. Recent reviews can be found in Refs. [11, 26, 50].

Recently, one system that has attracted particular attention is a three-terminal TE device that directly transforms thermal into electrical energy [51]. The system is composed of two QDs capacitively coupled to each other, where one of the QDs is immersed into two metallic leads, forming a semiconductor electron transistor (SET), and the other QD is connected to an electronic heat reservoir [51] in such a way that only thermal energy is exchanged between the heat reservoir and the SET. One striking characteristic of this geometry is that the electrical and thermal reservoirs

become isolated from each other. A review of that type of system, in which the heat reservoir includes bosonic degrees of freedom such as phonons, magnons, or microwave photons, is presented in Ref. [52]. Another physical system in which has been reported for the thermoelectric performance and the figure of merit a good result is the BiSb two-dimensional system under Rashba spin-orbit coupling (SOC). In this work, the SOC promotes thermoelectric performance and doubles the figure of merit ZT concerning the spin degenerate case [53]. Therefore, the SOC plays a crucial role when the electron's spin degree of freedom are considered, for example, in the spintronic field.

Since 1994, starting with the work by Meir and Wingreen [54], the effect of SOC over the Kondo state has been studied. After that, close to a dozen different groups have studied this subject [55–63]. The reason why this issue has attracted so much interest is reasonably straightforward. As SOC affects the spin degree of freedom of the conduction electrons (by coupling it to the linear momentum), and since the Kondo state is a many-body phenomenon that involves the conduction electrons' spins in a non-trivial manner, it was only natural to ask what consequences SOC could have over the Kondo effect.

Another way of approaching that is through symmetry arguments: since SOC breaks the spin $SU(2)$ symmetry of the conduction band, what effect could this have over the many-body spin-singlet (formed between the magnetic impurity and the conduction electrons) that characterizes the Kondo state? While the work by Meir and Wingreen [54], using general arguments, concluded that SOC did not suppress the Kondo effect, many subsequent works [55–63] have shown that the answer to this question is quite more nuanced. For example, Žitko and Bonča [56], using NRG to study the Kondo effect of a magnetic impurity coupled to a two-dimensional electron gas subjected to Rashba SOC, have shown that the Kondo temperature T_K varies with SOC, having behavior that depends on the parameters of the SIAM (see, for example, Figure 3 in Ref. [56]). On the other hand, Sousa *et al.* [61], analyzing a one-dimensional band subjected to Rashba+Dresselhaus SOC, using NRG arguments, have found that SOC exponentially increases T_K, besides generating a Dzyaloshinskii-Moriya interaction between the impurity and the conduction electrons (caused by the loss of $SU(2)$ symmetry of the conduction band). For a more detailed discussion of the extensive literature on Kondo+SOC, see Ref. [63]. Previous works that analyzed the SOC influence over TE properties of QDs in the Kondo regime [64, 65] have considered SOC just to coupling the QD to the conduction band, while here it is considered SOC in

the conduction band itself, and the following question is asked: How is the SOC effect on the thermoelectric properties of a quantum dot?

In this thesis, employing the numerical renormalization group (NRG) method [66, 67], it is studied the effect of conduction band spin-orbit coupling (SOC) over the SET's Kondo effect and TE transport properties. In the first case, viz., spin rotation and SIAM Hamiltonian in the σ_r basis, time-reversal and hybridization function, pseudo-spin SU(2) symmetry, and renormalized Haldane expression. The critical result is that under spin-rotation, The Hamiltonian, including the SOC, can be expressed similarly without SOC after a spin rotation about an arbitrary σ_r axis. Thus the hybridization function does not have any spin dependence on the new basis, and finally, the Kondo temperature is renormalized by the parameters of Anderson and spin-orbit. Second, electrical and thermal conductances, thermopower, Wiedemann-Franz law, and the dimensionless TE figure of merit. As main results, we show that SOC drives the system into the Kondo regime, where the universality of those properties is satisfied [8, 68–72], although we have found the interesting result that the universality of the thermopower is better fulfilled at the intermediate valence regime than at the Kondo regime. More importantly, we show that SOC causes a notable increase in the dimensionless figure of merit of a SET. Our analysis is done at low enough temperatures to warrant the neglect of the phononic contribution to the SET TE properties [73]. In addition, it is worth noting that there are also ways of decreasing the detrimental influence of phonons in the thermal efficiency of SETs by, for example, alloying the SET tunnel barriers to scatter phonons away from the QD [73–75].

The Thesis is organized as follows: in chapter 1, we contextualize our field of study and present our objectives. In chapter 2, we present the background necessary to understand about impurity problem from dilute magnetic alloys to confined nanostructures *Evolution of the Kondo Effect*. In chapter 3, we introduce the model in the presence of SOC, and we study the spin rotation, persistent spin helix (PSH). In chapter 4, we introduce the fundamental equations of thermoelectric transport properties. In chapter 5, we present the atomic approach method. In chapter 6, we present a discussion about the theory of the NRG method. In chapter 6.2, We discuss the "NRG Ljubljana" - open-source numerical renormalization group code employed in the calculations. In chapter 7, we present our results for Kondo temperature using NRG, the thermoelectric transport properties with atomic approach method and NRG method. Finally, in chapter 8, we present our conclusion and perspectives

Chapter 2

Background theory

2.1 Impurity problem

The magnetic impurities diluted in metallic samples are a long-standing problem. Its origin can be traced to the thirties when Wander de Haas and colleagues at the Kamerlingh Onnes Laboratory in Leiden, The Netherlands, measured the resistance of gold, copper, and lead as a function of temperature. They reported that the gold sample (not very pure) resistance was problematic because it presented a minimum at low temperatures [2] as indicated in Figure 2.1. The primary source of resistance in those systems is the scattering of electrons by lattice vibrations (phonons). The resistance should decrease as the temperature is lowered until it attains some residual value, at very low temperatures, due to impurities and defects present in the samples. This is what happened with the cooper sample, and just before the lead becomes a superconductor at around $7.2K$ [2]. The prime suspect for the scattering process responsible for the minimum in gold's resistance samples was the presence of impurities. In the 1960s, it was established that the effect was due to the presence of magnetic impurities in the metallic matrix that, under certain conditions, allow the formation of magnetic moments that act as new scatterer centers [76].

Experimentally the formation of magnetic moments in the alloys of the d-orbital transition elements with impurities does not occur in all cases, as shown in Figure 2.2. The Figure shows a series of susceptibility measurements performed on samples from zirconium to silver with a 1% impurity of iron by Clogston et al. [3]. The

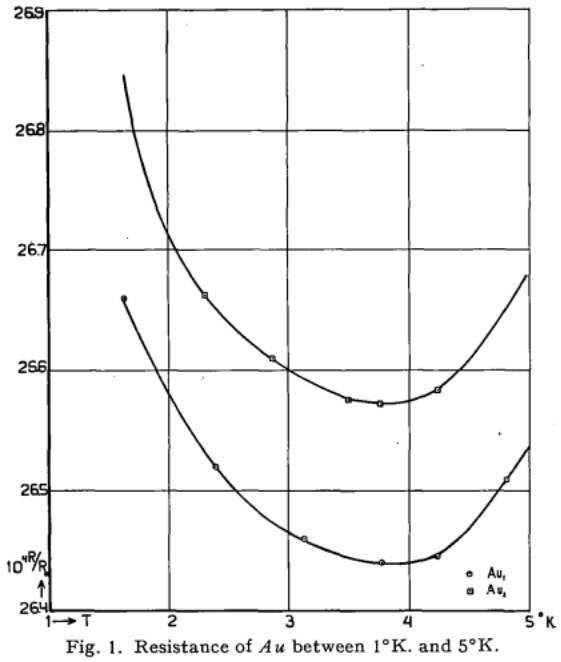

Fig. 1. Resistance of Au between 1°K. and 5°K.

Figure 2.1: First measurements concerning the Kondo effect: Resistance of Au between $1°K$ and $5°K$ [2]

Figure shows the susceptibility as a function of temperature; the elements with zero susceptibility(Zr, Nb, Re, Ru) have a susceptibility independent of temperature. The elements for which the susceptibility value is different from zero (Mo, Rh, Pd) have a temperature-dependent susceptibility. In the alloys, the magnetic susceptibility measurements show the local magnetic moments formation. In addition to the usual Pauli susceptibility, the system has a susceptibility dependent on the temperature expressed by the Curie-Weiss term

$$\chi = \frac{\mu_{eff}^2}{3k(T-\Theta)}, \tag{2.1}$$

where μ_{eff}, and Θ are the effective magnetic moment and the Curie temperature, respectively; the magnetic moment formation in this type of system was accepted for a long time as an experimental fact, without questioning how and under what conditions they appear. However, in the fifties, Friedel et al. [76] observed that the conducting bands of the metals were so large that the energy levels of the impurities were located inside them. Consequently, these states could not be truly located. To describe these localized states, Fridel introduced an essential concept of the *virtual bound states* i.e., a state that is obtained from the continuous free electron states. Such states cannot

stay eternally localized because they return to the continuous conduction band after a specific time τ. The local moments are determined by the condition in which the virtual states of the electrons with spin-up are different from the virtual states of spin-down

$$\langle n_\sigma \rangle \neq \langle n_{\bar{\sigma}} \rangle, \tag{2.2}$$

and the magnetic moment will exist on the impurity state. According to [77], a localized magnetic moment will be formed if the contribution of the impurity to the susceptibility follows the Curie-Weiss (2.1). In other ways, there will be no localized moment formation.

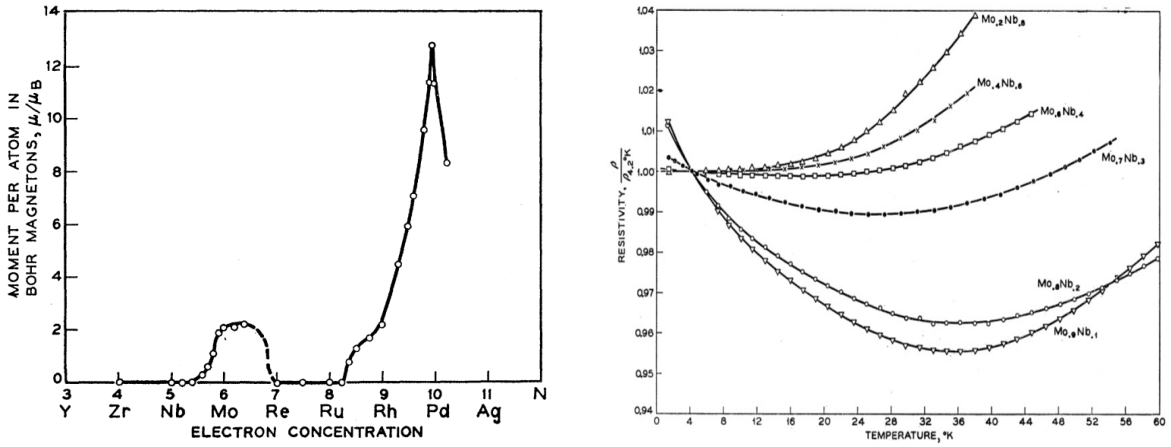

Figure 2.2: The left side Figure is the magnetic moment in Bohr magnetons of an iron atom diluted in various second-row transitions metals and alloys as a function of the electron concentration [3]. The Figure on the right side, measured in 1964, shows the minimum resistivity in alloys with 1% iron impurity concentrations [4], which confirms the earlier observations of the minimum in Figure 2.1.

Some dilute copper-iron alloys show the local magnetic moment formation and also the minimum in the electrical resistivity at low temperatures [78]. In Figure 2.2 [4] we show the local magnetic moment formation of Fe impurities in alloys of $Mo - Nb$ and $Mo - Re$ with 1% Fe impurities concentrations.

According to Figures. 2.2, the behavior of resistivity decreases monotonically with temperature up to a minimum that defines a characteristic temperature. Below this minimum temperature, the resistivity increases again with the logarithm of the temperature $ln(T)$. J. Kondo [79] was the first to associate the magnetic moment of the impurity with the occurrence of a minimum in the resistivity. He calculated, through a second-order perturbation theory, the electrical resistivity produced by the spin-flip

scattering of the conduction electrons with the localized magnetic moments and obtained the dependence of the resistivity with temperature as $J^3 ln(T)$, where J is the exchange coupling. When the exchange coupling parameter is negative (antiferromagnetic interaction), below a characteristic temperature known as the Kondo temperature T_K, this term diverges when $T \to 0$. This behavior does not have physical meaning; it only indicates that the perturbation theory is no longer valid under this temperature. Nevertheless, the experimental result shows that the resistivity was saturated to a finite value as shown in Figure 2.3.

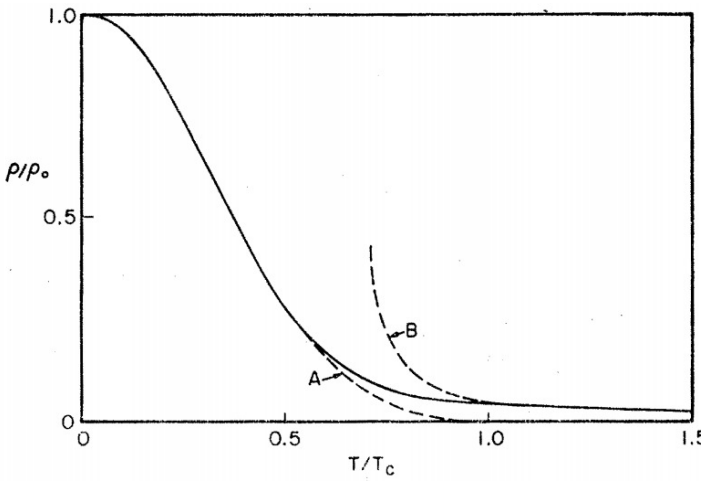

Figure 2.3: Temperature dependence of the resistivity and saturation when the $T \to 0$. Figure extracted from the reference [5].

At $T < T_K$, the conduction electrons' impurity is completely screened and loses its magnetic moment. Although susceptibility exceeds the Pauli-type contribution of the host metal, there is no temperature-dependent magnetism. Generally, it is accepted that the Kondo effect leads to total compensation of the localized moment by the polarization of the conduction electrons cloud around the impurity through the antiferromagnetic coupling. This collective effect is destroyed when the temperature increase. The Kondo transition from the magnetic regime to the nonmagnetic regime occurs gradually. Of course, such phase transition cannot be drastic after electrons conductions condense around an impurity in the real space are localized with few degrees of freedom involved in the process. Thus we should expect smooth variations in the properties of these systems when the temperature varies.

At the Kondo regime, the impurities are so far apart that their interaction is almost negligible. When the concentration increases, the interaction between the localized moments becomes essential, and at the same time, the disordered character of the

system appears more intensely. In this region, impurities interact strongly via $RKKY$ interaction (interaction between magnetic moments is mediated by conducting electrons and tends to zero and are proportional to r^{-3}). At this highly disordered regime a phase transition occurs known as the "Spin Glass". In the region of high concentrations, the impurities are closer and interact via direct exchange coupling, and the system pass to acquire some magnetic order (ferromagnetic or antiferromagnetic).

2.2 Anderson model

The usual band theory is not able to adequately describe metallic systems with diluted magnetic impurities; it is because, in a general way, the energies of the localized states are located inside the conduction band of the host metal, and the band theory is not able to describe the localization of the impurity state. To solve this theoretical difficulty, Anderson in 1961 [6] proposed an essential model to study the magnetic impurity problem of the condensate matter physics. His model was motivated by the experimental observation that the magnetic moment of a transition metal atom in a dilute solution of transition metals remains localized [80] and plays a crucial role in the understanding the physics behind the local magnetic moment.

He assumed that localized moments in metals originated from the Coulomb correlation between electrons from inner orbitals of the magnetic impurity. Under this assumption, he described the conduction electrons by Bloch states $\phi_k(\boldsymbol{r})$ at the position $\boldsymbol{r}$

$$\psi_{r_n} = \frac{1}{\sqrt{N}} \sum_{\boldsymbol{k}} e^{-i\boldsymbol{k}\cdot\boldsymbol{r}_n} \phi_{\boldsymbol{k}}(\boldsymbol{r}), \tag{2.3}$$

while the impurity as a local state site represented by an atomic orbital function ϕ_d, and $\psi_{\boldsymbol{r}_n}(\boldsymbol{r})$ is the Wannier function at the site $\boldsymbol{r}_n$. The interaction between localized site and electron conduction is given by hybridization matrix elements $V_{\boldsymbol{k}}$,

$$V_{\boldsymbol{k}} = \sum_{\boldsymbol{r}_n} e^{i\boldsymbol{k}\cdot\boldsymbol{r}_n} \langle \phi_d | H | \psi_{\boldsymbol{r}_n} \rangle. \tag{2.4}$$

Additionally, in the localized state, we have a configuration of four states, one unoccupied with energy $\epsilon_d = 0$, two occupied by one electron with spin up or spin

down and energy ϵ_d, respectively and finally the double occupied state with electrons with spin up and down with an energy $\epsilon_d + U$, where U is introduced due to the interaction between electrons with spin up and spin down in the localized site

$$U = \int \phi_d^*(\boldsymbol{r}).\phi_d^*(\boldsymbol{r'})\frac{e^2}{|\boldsymbol{r}-\boldsymbol{r'}|}\phi_d(\boldsymbol{r})\phi_d(\boldsymbol{r'})d\boldsymbol{r}d\boldsymbol{r'}. \tag{2.5}$$

Another point that should be stressed is that the atomic state $|d\rangle$ and the Bloch states are not orthogonal. However, imposing the orthogonality condition $\langle d|k\rangle = 0$ and considering that the orbitals d, f have spheric symmetry, Anderson's model for the impurity is described by the Hamiltonian

$$H_A = \sum_\sigma \epsilon_d n_{d,\sigma} + U n_{d,\uparrow} n_{d,\downarrow} + \sum_{\boldsymbol{k},\sigma} \epsilon_{\boldsymbol{k}} c^\dagger_{\boldsymbol{k},\sigma} c_{\boldsymbol{k},\sigma} + \sum_{\boldsymbol{k},\sigma} (V_{\boldsymbol{k}} c^\dagger_{d,\sigma} c_{\boldsymbol{k},\sigma} + V^\dagger_{\boldsymbol{k}} c^\dagger_{\boldsymbol{k},\sigma} c_{d,\sigma}), \tag{2.6}$$

where the first two terms describe the impurity energy, with local site energy ϵ_d and spin σ, and the interaction U between electrons with spin up and spin down. The number operator $n_{d\sigma} = d^\dagger_\sigma d_\sigma$, where $d^\uparrow, d_\sigma$ creates and destroys electrons on the local site. The third term describes the conduction electrons with energy ϵ_k and momentum $\boldsymbol{k}$, the $c^\dagger_{\boldsymbol{k}\sigma} c_{\boldsymbol{k}\sigma}$ operators create and annihilate conduction electrons with $\boldsymbol{k}, \sigma$ momentum and spin, respectively. Finally, the last term represents the coupling between conduction and impurity electrons described by the hybridization $V_{\boldsymbol{k}d}$.

To solve the Hamiltonian, Anderson employed the equation of movement method (EOM) [81], considering the Hartree- Fock approximation, he obtained the Green function for the localized states, corresponding to the Equation 2.6 as

$$G^\sigma_d(\omega) = \frac{1}{\omega - \varepsilon_\sigma - \sum(\omega)}, \tag{2.7}$$

where $\varepsilon_\sigma = \epsilon_d + U\langle n_{d,\bar{\sigma}}\rangle$, with the $\langle n_{d,\bar{\sigma}}\rangle$, representing the average number of electrons with spin $\bar{\sigma}$, and the self-energy term is given by

$$\sum(\omega) = \sum_{\boldsymbol{k}} \frac{|V_{\boldsymbol{k}d}|^2}{\omega - \epsilon_{\boldsymbol{k}} + i\eta}, \tag{2.8}$$

where the small quantity $\eta \to 0^+$ was introduced to turn the Green's functions retarded.

The density of localized states is given by

$$\rho_{d\sigma}(\omega) = -\frac{1}{\pi} ImG^{\sigma}_{dd}(\omega). \tag{2.9}$$

Substituting Eq. (2.8) in Eq. (2.7), the explicit form of the localized density of states is given by

$$\rho_{d\sigma} = \frac{1}{\pi} \frac{\Delta}{(\omega - \varepsilon_{\sigma})^2 + \Delta^2}, \tag{2.10}$$

that means the localized density of states is modified by the *virual bound state energy* at $\omega = \varepsilon_{\sigma}$, and by the width Δ, where

$$\Delta(\omega) = \pi \langle V^2 \rangle \rho_{\boldsymbol{k}}(\omega), \tag{2.11}$$

where $\rho_{\boldsymbol{k}}(\omega)$ is the density of state of the host metal conduction electrons. At $T = 0$ the occupation number of the local site is obtained from (2.9)

$$\langle n_{d\sigma} \rangle = \int_{-\infty}^{\epsilon_f} ImG^{\sigma}_{dd}(\omega) d\omega, \tag{2.12}$$

eliminating the average value representation and specifying the spin up and down as $\pm$ respectively, we obtain a system of equations that can be solved selfconsistently

$$n_{d\pm} = \frac{1}{\pi} \tan^{-1}[y(n_{d\pm} - x)], \tag{2.13}$$

where x and y are adimensional parameters given by

$$x = \frac{\epsilon_F - \epsilon_d}{\Delta}, \tag{2.14}$$

$$y = \frac{U}{\Delta}. \tag{2.15}$$

The transition curve that separates the magnetic from the nonmagnetic region can be obtained from (2.13), as a relation between the x and y parameters for which the magnetic solutions degenerate into a single solution $n_{d+} = n_{d-} = n$, together with the

conditions $f(n) = 0$ and $f'(n) = 0$ that gives the cycloid parametric equation

$$x = \frac{1}{2\pi}(\theta - sin(\theta)), \tag{2.16}$$

$$\frac{\pi}{y} = \frac{1}{2}(1 - \cos(\theta)), \tag{2.17}$$

$$\theta = 2\pi n_c, \tag{2.18}$$

where n_c is the critical concentration. The cycloid solution is shown Figure 2.4, where there is high tendency to magnetism ($\langle n_{d+}\rangle \neq \langle n_{d-}\rangle$), when the system is in the strong correlation regime, when y is large and x is near to the $1/2$. This situation corresponds to the case where the localized level ϵ_d and $U + \epsilon_d$ are symmetric to the Fermi level.

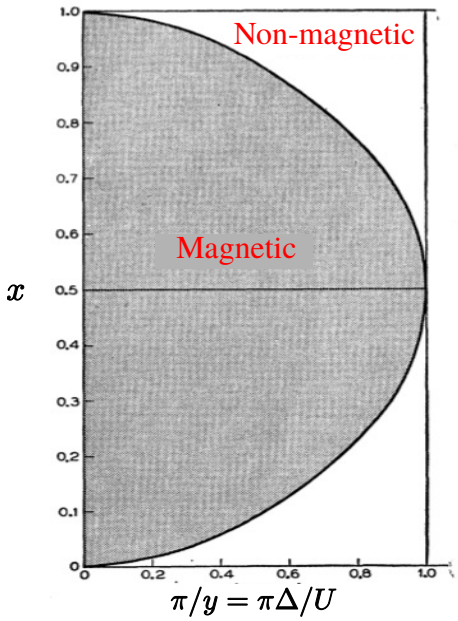

Figure 2.4: Phase transition from the magnetic to the non-magnetic region [6].

In this limit just one electron is occupying the local state $\langle n_{d+}\rangle$, while the state $\langle n_{d-}\rangle = 0$. The nonmagnetic case ($\langle n_{d+}\rangle = \langle n_{d-}\rangle = n$), corresponds to the weak correlation regime, when y is small. The localized site that was initially occupied by one electron with spin σ is also occupied by another electron with opposite spin, and thus given the double occupation $\langle n_{d+}\rangle = \langle n_{d-}\rangle = 1/2$.

2.3 Kondo effect

Motivated by the experimental observation of the electrical resistivity minimum that appears, at low temperatures, in a magnetic impurity diluted in metallic matrix systems [4, 82, 83], J.Kondo in 1964 [79] introduced a model to describe the scattering of conduction electrons from a localized magnetic impurity. He calculated the minimum in electrical resistivity measurements at a low temperature. The initial proposal was made by Zener [84] to describe the ferromagnetic metal transitions in a sample constituted of d electrons localized in the ionic site and itinerant electrons s on the crystal. He considered the exchange interaction between d and s electrons responsible for their magnetic properties. This model can be applied to rare earth metals due to the $4f$ localized states immersed in the large conduction band. Therefore, the corresponding Hamiltonian can be written as

$$\mathcal{H} = \mathcal{H}_c + \mathcal{H}'_{sd}, \tag{2.19}$$

with $\mathcal{H}_c$ describing the conduction band of the itinerant electrons

$$\mathcal{H}_c = \sum_{k,\sigma} \epsilon_k c^\dagger_{k,\sigma} c_{k,\sigma}, \tag{2.20}$$

and $\mathcal{H}'_{sd}$ represents the interaction of the conduction electrons with the spins of the localized impurity, with $c^\dagger_{k\sigma}(c_{k\sigma})$ being the conduction electron annihilation(creation) operators with spin σ and momentum k

$$\mathcal{H}'_{sd} = \sum_{k,k'} J_{k,k'} \left[S^z (c^\dagger_{k,\uparrow} c_{k',\uparrow} - c^\dagger_{k,\downarrow} c_{k',\downarrow}) + S^+ c^\dagger_{k,\downarrow} c_{k',\uparrow} + S^- c^\dagger_{k,\uparrow} c_{k',\downarrow} \right], \tag{2.21}$$

where the S^z and S^+, S^- are the spin operators defined as $S^\pm = S_x \pm iS_y$, for a state of the spin S, $J_{k,k'}$ is the exchange coupling constant that characterizes the coupling between localized spins ions with conduction band electrons. The first term represents the direct scattering process between conduction electrons with impurity ions. While the second and the third terms represent the scattering spin-flip process with coupling $J_{k,k'}$, which according to Kondo [79] produces the unusual resistance electric behavior at low temperatures. The scattering processes that occur in this model are:

1. The electron $(\vec{k}, \sigma)$ is scattered to state $(\vec{q}', \sigma)$ and after suffers a second scatter to state $(\vec{k}', \sigma)$.

2. One of the electrons from the state $(\vec{q}, \sigma)$ is scattered to $(\vec{k}', \sigma)$, then the electron of the state $(\vec{k}, \sigma)$ occupy the state $(\vec{q}, \sigma)$ that was previously unoccupied.

3. The electron $\vec{k}, \sigma$ is scattered to state $\vec{q}', \bar{\sigma}$, while the spin component z is of the *nth*-impurity atom represented by M_n increases from M_n to $M_n + 1$. The electron is scattered again to state $\vec{k}', \sigma$ while the z component of the localized electron returns to the M_n value.

4. One of the two electrons is scattered from occupied state $\vec{q}, \bar{\sigma}$ to $\vec{k}', \sigma$ and at same time M_n decrease ($M_n \rightarrow M_n - 1$). The electron with $(\vec{k}, \sigma)$ occupy the state $(\vec{q}, \bar{\sigma})$ that was unoccupied and the impurity atom returns to the original value M_n.

In the second order scattering processes the electrons $(\vec{k}, \sigma)$ are scattered to final state $(\vec{k}', \bar{\sigma})$. These intermediate states processes are:

1. The electron $(\vec{k}, \sigma)$ is scattered to state $(\vec{q}', \bar{\sigma})$, while the z spin component of the *nth*-impurity atom increases from M_n to $M_n + 1$.

2. One electron from the occupied state indicated by $(\vec{q}, \bar{\sigma})$, is scattered to the state $(\vec{k}', \bar{\sigma})$ and the z electron localized component M_n remains unaltered. After an electron with $(\vec{k}, \sigma)$ occupies the state $(\vec{q}, \bar{\sigma})$ that was unoccupied, the impurity atom increase to $M_n + 1$.

3. The electron $(\vec{k}, \sigma)$ is scattered to an unoccupied state $(\vec{q}', \sigma)$ and the z component of the localized electron spin remains M_n. After the conduction electron is scattered to state $(\vec{k}, \bar{\sigma})$, and the z spin component of the impurity atom changes from M_n to $M_n + 1$.

4. One of the two electrons that occupies the state, indicated by $(\vec{q}, \sigma)$, is scattered to state $(\vec{k}', \bar{\sigma})$ and M_n changes to $M_n + 1$, subsequently the electron with $(\vec{k}, \sigma)$ occupies the state $(\vec{q}, \bar{\sigma})$ that was unoccupied and the z component of the impurity atom remains $M_n + 1$.

To simplify the calculations, Kondo [79] considered just one impurity atom with a scattered process $(\vec{k},\sigma) \rightarrow (\vec{k}',\sigma)$ and a flat band to the conduction electrons that is

$$\rho(\epsilon) = \begin{cases} \rho & -D \leq \epsilon \leq D \\ 0 & otherside \end{cases}, \tag{2.22}$$

where the ρ is a constant and $2D$ is the bandwidth. Then, considering the scattering processes with the change of the electron spins in the intermediate states, he calculated the electrical resistivity until second order on J through the perturbation theory and obtained the result

$$R = c\rho\ J^2 S(S+1)A\left[1 + 4J\rho\ ln\left(\frac{k_B T}{D}\right)\right], \tag{2.23}$$

where the c and A are the impurity concentrations and a constant, respectively. To an antiferromagnetic coupling $J < 0$, the logarithmic term in the Equation 2.23 grows when the temperature decreases and diverges $T \rightarrow 0$. The origin of this divergence resides in the Pauli principle for intermediate states because the spin operators cannot commute in the intermediate states. This means that the perturbation theory is not more valid under a certain temperature called Kondo temperature T_K. On the other hand, the scattering by the spin-flip process must be treated as a many-body problem because the electron scattered to the state $(\vec{k},\sigma)$ feel the occupation of the other electrons that are occupying the state $(\vec{q},\sigma')$.

If we add the logarithmic term to the contribution of the phonon resistivity that is proportional to T^5, and there will be a minimum in resistivity [78] at temperature T_K ($\frac{dR(T)}{dT} = 0$). For $T > T_K$ the resistivity is describes by $R(T) = A + Bc(lnT)$ with c impurity concentrations while A, B are constants, where the T_K is proportional to $c^{1/5}$. In this way, the resistivity agrees to the experimental results for $T > T_K$, but for $T < T_k$ the Equation (2.23) predict a logarithmic divergence which is not confirmed by the experimental results because it saturates in a finite value when the temperature goes to zero. This indicates that the perturbation theory does not work properly for temperatures below T_K. This problem was solved by [5, 85] and produced the correct behavior of the resistivity, according to experimental results, as shown in Figure (2.2), and the Kondo temperature is given by

$$k_B T_K = D e^{\frac{D}{2J}}, \tag{2.24}$$

with J being the antiferromagnetic coupling parameter. In this case, it was shown that the Hamiltonian has a degenerated ground state of the singlet type. The Kondo effect carries the total compensation of the conduction electrons cloud, which is the polarization around the impurity. Finally, the Kondo problem was solved by the numerical renormalization group (NRG), introduced by K. Wilson in 1975, [86].

In summary, the Kondo problem:

1. Exhibits a characteristic temperature T_K given by the Equation 2.24 that separates two physically different regimes.
2. For $T > T_K$, the impurity spin fluctuates freely due to metal thermal agitation. In this limit, the perturbation theory works without problem.
3. For $T < T_K$, the impurity spin form a singlet state with a complete compensation of the moments by the conduction electrons cloud.
4. The results corresponding to the crossover region $T \approx T_K$ are obtained by the numerical renormalization group [86].

Chapter 3

Conduction band spin-orbit coupling (SOC)

In this section, we propose to study the problem of a quantum impurity interacting with a Fermi sea of conduction electrons. The impurity models either a quantum dot or an actual magnetic atom adsorbed into the Fermi sea. We will consider a one-dimensional Fermi sea that models, for example, a quantum wire (QW). The quantum impurity coupled to the QW will be modeled by the single impurity Anderson model (SIAM) [6], whose 'traditional' Hamiltonian is SU(2)-symmetric, thus diagonal in the S_z spin basis. However, since our QW is under the influence of spin-orbit coupling (SOC), the Hamiltonian is no more diagonal. The SOC is a fantastic phenomenon that arises from the interaction of the electron spin with self linear momentum. It arises naturally from the Dirac equation as a correction due to relativistic effects. On the other hand, from the theory of symmetries in quantum mechanics, the SOC obeys the time-reversal symmetry. This means that, time-reversal symmetry,when applied over an arbitrary eigenstate of the Hamiltonian, produces another eigenstate with the same energy. This pair of states is called a Kramers' doublet, which is composed by $|k,\uparrow\rangle$ and $|-k,\downarrow\rangle$ states, i.e., states with opposite linear momenta and spin. In the next section we provide details about SOC.

3.1 Spin-orbit coupling

SOC arises for the first time as an attempt to explain the spectral lines of the anomalous Zeeman effect and the fine structure interaction. It was then that the idea of the electron spin was introduced, showing that, if the electron had a g factor of 2, the anomalous effect could be explained consistently, while for the fine structure interaction, it was still necessary to consider $g = 1$. That was until 1926, when L. H. Thomas [87] showed that the origin of the discrepancy was a relativistic kinematic effect and that the proper inclusion of a g-factor could explain both phenomena at once (a detailed explanation about Thomas' treatment can be found in Ref. [88]). A complete comprehension of the spin only came through relativistic quantum mechanics, where the factor g arises naturally from the Dirac theory of the relativistic electron [89].

The Dirac theory results in an equation that describes the relativistic electron, with mass m and charge e, moving in an external electric field, by a four-component spinor wave function. The non-relativistic limit is the so-called Pauli equation, with a two-component spinor wave function, where a spin-orbit coupling term appears naturally as a correction of order v^2/c^2, which can be written as

$$\frac{-e\hbar}{4mc^2}\boldsymbol{\sigma}\cdot(\boldsymbol{E}\times\boldsymbol{p}), \tag{3.1}$$

where v is the electron velocity, c is the speed of light, and $\hbar$ is the reduced Plank constant. Then, this term describes the interaction of the electron spin with an effective magnetic field $\boldsymbol{B}_{soc}$. Thus, the electron moves in the electric field produced by the nucleus charge, and, in its rest frame it feels an apparent magnetic field $\boldsymbol{B}_{soc} \propto \boldsymbol{E}\times\boldsymbol{v}/c$, where $\boldsymbol{E}$ is the electric field due to the nuclear charge, and $\boldsymbol{\sigma}$ are the Pauli spin matrices. The principal ingredient here is the nuclear electric field $\boldsymbol{E}$, because in Condensed Matter systems it can be manipulated externally through a potential gradient $-\nabla V$. Thus the typical expression for SOC is obtained

$$\mathcal{H}_{so} = -\frac{\hbar}{4m_0^2c^2}\boldsymbol{\sigma}\cdot(\boldsymbol{p}\times\nabla V_0), \tag{3.2}$$

where V_0 is the atomic potential, which can be modified externally, and $\boldsymbol{\sigma} = (\sigma_x, \sigma_y, \sigma_z)$ is a vector of Pauli spin matrices. In many semiconductors, the spin degeneracy is the

combined effect of the inversion symmetry in space and time [90] and, consequently, it has quadruple energy level degeneracy $E(k,\uparrow\downarrow) = E(-k,\downarrow\uparrow)$. Such spin degeneracy can be lifted by applying an external magnetic field (Zeeman effect). In systems where the electron is subjected to an electric field produced by an inversion *asymmetric* potential, the splitting of the degeneracy can take place even without an external magnetic field, that is $B = 0$, through SOC. In other words, we still have that $E(k,\uparrow) = E(-k\downarrow)$ and $E(k,\downarrow) = E(-k\uparrow)$, due to *time-reversal* symmetry, which is not broken by SOC. However, due to broken *spatial inversion*, we do not have anymore that $E(k) = E(-k)$, independently of spin. In quasi-2D quantum wells, the spin-split degeneracy can appear in two different ways, one is due to bulk inversion asymmetry (BIA) [91], studied initially in zinc-blende structures, and another way is due to the electric field produced by an asymmetric potential, called structure inversion asymmetry (SIA) [92, 93]. Thus, because of lack of spatial inversion symmetry in the material, SOC splits spin degeneracy, and the SOC contribution to the Hamiltonian can be written as $H_{soc} = H_R + H_D$. Considering only the linear terms on $\boldsymbol{k}$, the H_{SOC} can be written as,

$$H_R = \alpha_R \left(k_y\sigma_x - k_x\sigma_y\right), \tag{3.3}$$

$$H_D = \beta \left(k_x\sigma_x - k_y\sigma_y\right), \tag{3.4}$$

where α_R, β are the Rashba and Dresselhaus SOC constants, respectively, and k_x, k_y are the conduction electron wave vector components in the x-axis and y-axis directions. In materials without an inversion center, the Dresselhaus spin-orbit magnetic field B_{soc} arises purely from microscopic effects [90], where the electric field E and the momentum $\boldsymbol{p}$ are odd under the parity symmetry-operation, thus, around the Brillouin zone center, the Γ-point, like in GaAs or InSb [21], the Dresselhaus SOC has the form (3.4). On the other hand, Rashba-type SOC (which can be manipulated externally) arises because of an $E \cdot \boldsymbol{r}$ term that appears in the Taylor's expansion of the $V(\boldsymbol{r})$ potential.

The effects mentioned until now were limited just to 2D systems, and have been intensively studied in different areas of Condensed Matter Physics. But we are interested in the 1D case, due to the current interest in QWs. A quasi-1D system with SOC was presented in Ref. [94], where the Rashba and Dresselhaus terms are reduced to $H_R = -\alpha_R\sigma_y k_x$, and $H_D = \beta\sigma_x k_x$, in a way that $H_{soc} = H_R + H_D$ can be written

compactly, in real space, as

$$H_{soc} = -\sum_{l,\sigma'\sigma} c^{\dagger}_{l+1,\sigma}(i\boldsymbol{\tau})_{\sigma\sigma'}c_{l\sigma'} + h.c., \tag{3.5}$$

where $c_{l,\sigma}$ annihilates a spin σ electron in site l, $c^{\dagger}_{l+1,\sigma'}$ creates a spin σ' electron in site $l+1$, $(i\boldsymbol{\tau})_{\sigma\sigma'}$ is a matrix element of the SOC matrix $\boldsymbol{\tau}$, defined below, and $h.c.$ means Hermitian conjugate. The $\boldsymbol{\tau}$ matrix is given by

$$\boldsymbol{\tau} = \begin{pmatrix} 0 & \gamma \\ \gamma^{*} & 0 \end{pmatrix}, \tag{3.6}$$

where $\gamma = \beta + i\alpha_R$. In our problem, we also consider that a *local* SOC interaction $\boldsymbol{\tau}_{imp}$ can promote a spin-flip of an electron that hops from the site $l = 0$ of the linear chain to the quantum dot

$$H_{hyb-soc} = \sum_{\sigma,\sigma'} c^{\dagger}_{0\sigma}\left(i\boldsymbol{\tau}_{imp}\right)_{\sigma\sigma'} d_{\sigma'} + h.c., \tag{3.7}$$

where $\boldsymbol{\tau}_{imp}$ is defined in the same way as the matrix $\boldsymbol{\tau}$, with elements $\gamma_{imp} = \beta_{imp} + i\alpha_{R,imp}$, and d_σ is the operator that annihilates a spin σ electron in the quantum dot. Then, applying a Fourier transform to the linear chain second quantization operators, the H_{soc} can be written in k space as

$$H_{soc} = \sum_{k} -2\sin(ka)(\gamma c^{\dagger}_{k\uparrow}c_{k\downarrow} + \gamma^{*}c^{\dagger}_{k\downarrow}c_{k\uparrow}), \tag{3.8}$$

and, as well, Eq. (3.7) can be rewritten as

$$H_{hyb-soc} = \sum_{k} i(\gamma_{imp,k}c^{\dagger}_{k\uparrow}d_{\downarrow} + \gamma^{*}_{imp,k}c^{\dagger}_{k\downarrow}d_{\uparrow} - \gamma_{imp,k}d^{\dagger}_{\uparrow}c_{k\downarrow} - \gamma^{*}_{imp,k}d^{\dagger}_{\downarrow}c_{k\uparrow}), \tag{3.9}$$

where a is the lattice constant parameter and $c^{\dagger}_{k\uparrow}(c_{k,\downarrow})$ is an electron creation (annihi-

lation) operator with momentum k and spin up (down).

3.2 Model

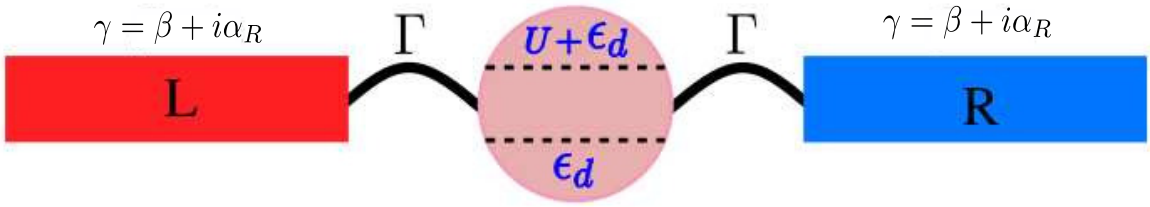

Figure 3.1: Single SET model. SOC is considered in the left and right conduction band $\gamma = \beta + i\alpha_R$, with β and α_R are Dresselahaus and Rashba SOC respectively, which is coupled to center QD with single ϵ_d a double $U + \epsilon_d$ occupation levels, and Γ is the hybridization between QD and QW.

The Figure 3.1, the SIAM for our system, including SOC in the left and right side conduction band, is constituted by a semi-infinte chain with SOC modeled as a QW, coupled to an embeded QD. The total Hamiltonian is then given by

$$H = H_{wire} + H_{imp} + H_{hyb}, \tag{3.10}$$

where H_{wire} describes the QW electrons, H_{imp} describes the quantum dot, while H_{hyb} is the coupling between the wire and the quantum dot:

$$H_{wire} = \sum_{k,\sigma}(\epsilon_k + \mu)n_{k\sigma} + \sum_{k} -2\sin(ka)(\gamma c^{\dagger}_{k\uparrow}c_{k\downarrow} + \gamma^* c^{\dagger}_{k\downarrow}c_{k\uparrow}), \tag{3.11}$$

$$H_{imp} = \sum_{\sigma}\epsilon_d n_{d\sigma} + U n_{d\uparrow}n_{d\downarrow}, \tag{3.12}$$

$$H_{hyb} = \sum_{k,\sigma} V_k(c^{\dagger}_{k\sigma}d_{\sigma} + d^{\dagger}_{\sigma}c_{k\sigma}) + H_{hyb-soc}, \tag{3.13}$$

where $\epsilon_k = -2t\cos(ka)$ is the dispersion relation, t is the nearest-neighbor hopping parameter, μ is the chemical potential, $n_{k\sigma} = c^{\dagger}_{k\sigma}c_{k\sigma}$ and $n_{d\sigma} = d^{\dagger}_{\sigma}d_{\sigma}$ are the occupation number operators for conduction electrons and quantum dot electrons, ϵ_d and U are the

localized energy level and Coulomb repulsion energy in the quantum dot, respectively. Finally, the hybridization term is given by two contributions, V_k and the elements of $H_{hyb-soc}$. For simplicity's sake, both hybridization terms are considered k-independent, and therefore, from now on we can remove their k-indexes, resulting in $V_k \to V$ and $\gamma_{imp,k} \to \gamma_{imp}$.

Because of the spin-flip terms caused by SOC, the conduction electron spin is no more a good quantum number. It is well-known that in the original SIAM the spin is a good quantum number, or, in other words, the original SIAM is SU(2)-symmetric. As shown by Haldane [95], in the SU(2)-symmetric case the Kondo temperature T_K can be expressed using the so-called Haldane formula, which expresses T_K in terms of the SIAM parameters U, D, and $\Gamma = \pi\rho_0 V^2$, i.e., Coulomb repulsion, half band-width, and hybridization, being ρ_0 the conduction band density of states at the Fermi energy.

Therefore, as SOC breaks spin SU(2) symmetry, one may be inclined to assume that the Kondo temperature probably may not be computed by the Haldane expression [95]. This is because the Kondo singlet state occurs when the impurity is coupled to the conduction electrons through a hybridization function which is diagonal in spin and independent of it. In other words, when the hybridization function is a scalar function. It turns out that, as will be shown below, because SOC preserves time-reversal symmetry, the hybridization function for a finite-SOC model like ours is still a scalar function, despite the loss of SU(2) symmetry.

Now, the 2×2 matrix in Eq. (3.11) is composed by the diagonal elements of its first term, i.e., $\langle k\uparrow|H_{wire}|k\uparrow\rangle = \langle k\downarrow|H_{wire}|k\downarrow\rangle = -2t\cos(ka)+\mu$, and the non-diagonal elements of its second term $\langle k\uparrow|H_{wire}|k\downarrow\rangle = \langle k\uparrow|H_{soc}|k\downarrow\rangle = -2\gamma\sin(ka)$, and $\langle k\uparrow|H_{wire}|k\downarrow\rangle = \langle k\downarrow|H_{soc}|k\uparrow\rangle = -2\gamma^*\sin(ka)$, i.e., the spin-flip terms caused by SOC. The eigenvalues of Eq. (3.11) are given by

$$\epsilon_{k\pm} = -2t\cos(ka) \mp 2|\gamma||\sin(ka)| + \mu, \tag{3.14}$$

while its eigenvectors are given by

$$|\epsilon_{k\pm}\rangle = \frac{1}{\sqrt{2}}\left(|\uparrow\rangle \mp S_k e^{-i\phi}|\downarrow\rangle\right), \tag{3.15}$$

where $\phi = \tan^{-1}(\alpha_R/\beta)$, and $S_k = sign(k)$ is the signal function, which comes from the $|\sin(ka)|$ term in equation (3.14) and is defined as

$$S_k = \begin{cases} 1 & if \quad k > 0 \\ 0 & if \quad k = 0 \\ -1 & if \quad k < 0 \end{cases}, \tag{3.16}$$

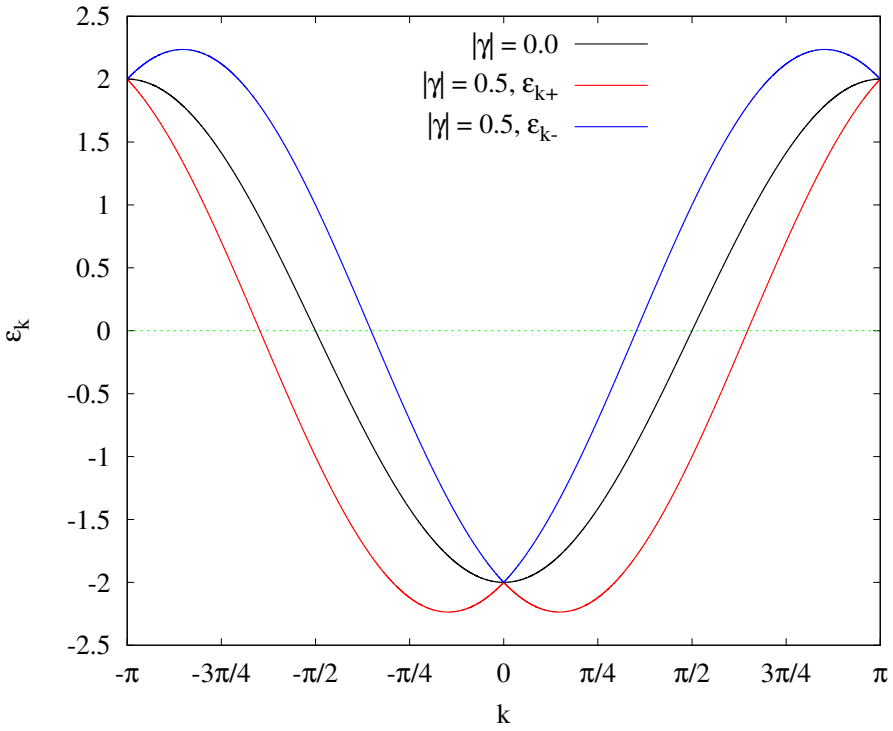

Figure 3.2: Dispersion relation including the SOC contribution to the energy, the black curve is the case without SOC while the blue and red curves are with SOC $|\gamma| = 0.5$, with the hopping parameter t as units.

The dispersion relation 3.14 is shown in Fig. 3.2. The black curve is for zero-SOC and the red and blue curves (defined according to their helicity $\mu = +$ (red) and $\mu = -$ (blue), see Appendix A) are for finite-SOC. It can be easily seen, by comparing the black curve with the red and blue curves in Fig. 3.2, that SOC increases the bandwidth of the conduction electrons. The study of the density of states using the helicity quantum number ν is done in Appendix A. As discussed below, the use of the helicity quantum number ν to diagonalize the conduction bands does not help us once H_{imp} and H_{hyb} are taken in account, since this quantum number (as it depends on the conduction electron spin *and* the sign of k) cannot be defined for electrons in the quantum dot. The strategy

to circumvent this problem is to do a change of basis so that the Hamiltonian (3.11) is still diagonal, but the eigenstates can be defined through the spin quantum number, however, for a different orientation of the spin z-axis, as shown below.

3.3 Spin rotation and SIAM Hamiltonian in the σ_r basis

Let us first analyze the decoupled (no impurity) QW. In Fig. 3.3(a), it is shown the dispersion when there is no SOC, $\gamma = 0$ (solid-red/dashed-blue curve for spin up/down). In this case, the Hamiltonian has spin SU(2) symmetry, i.e., the spin is a good quantum number and the energy dispersion does not depend upon it. Thus, due to combined time-reversal and spatial-inversion symmetries, the eigenstates $|k\uparrow\rangle$ and $|k\downarrow\rangle$ are degenerate and the spin quantization z-axis can be chosen to point in any direction. However, for finite-SOC, the spin angular momentum, for an arbitrary quantization axis, is no longer a good quantum number, because of the spin-mixing term in Eq. (3.8). Nonetheless, as SOC preserves time-reversal symmetry, we can define a helicity operator $\hat{h}$ (see Eq. A.5 in Appendix A) such that $[\hat{h}, H_{wire}] = 0$, and whose eigenvalues $\nu = \pm$ are thus good quantum numbers for the eigenstates of H_{wire}. Indeed, in the helicity basis (see Eq. A.6 in Appendix A), given by

$$c^\dagger_{k\nu} = \frac{1}{\sqrt{2}}\left(c^\dagger_{k\uparrow} + \nu s_k e^{i\phi} c^\dagger_{k\downarrow}\right), \tag{3.17}$$

where $\phi = \tan^{-1}(\alpha/\beta)$ and $s_k = \mathrm{sgn}(k)$, the Hamiltonian $H_{wire} = \sum_{k,\nu} \epsilon_{k\nu} c^\dagger_{k\nu} c_{k\nu}$ is diagonal, with a dispersion relation given by

$$\epsilon_{k\nu} = -2t\cos k - 2\nu|\gamma||\sin k| + \mu. \tag{3.18}$$

Figure 3.3(b) shows $\epsilon_{k\nu}$, for $|\gamma| = 0.5$, plotted as a function of k for each ν: the lower band (solid-red curve) is associated to the quantum number $\nu = +$, and the upper band (dashed-blue curve) is associated to $\nu = -$. As SOC preserves time-reversal symmetry, i.e., $[\Theta, H_{wire}] = 0$, where Θ is the time-reversal operator, we have degenerate Kramer's doublets [89] in the same helicity band, $\epsilon_{k\nu} = \epsilon_{-k\nu}$.

However, as the helicity ν is not defined for the impurity, its coupling to the QW

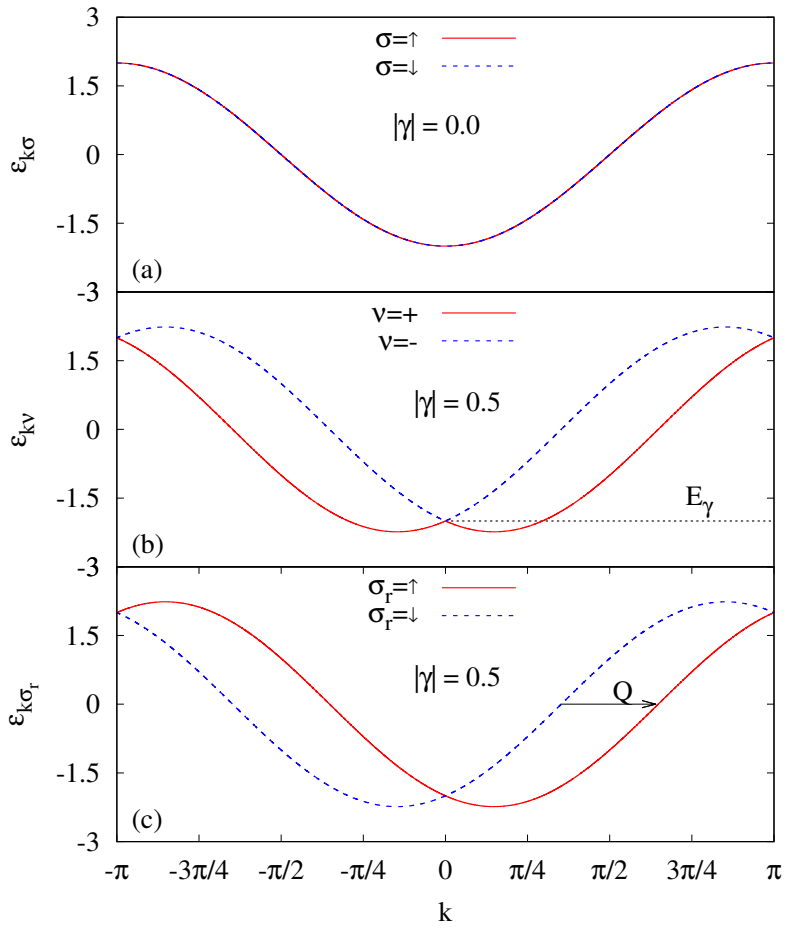

Figure 3.3: (a) Quantum wire dispersion $\epsilon_{k\sigma} + \mu$ for zero-SOC. Solid/dashed (red/blue) curve for $\sigma = \uparrow / \downarrow$ (b) Dispersion $\epsilon_{k\nu}$ for $|\gamma| = 0.5$. Here, the bands are characterized by the helicity quantum number ν: solid/dashed (red/blue) curve for $\nu = +/-$ (c) Same as in (b), but now the bands are characterized by the quantum number σ_r: solid/dashed (red/blue) curve for $\sigma_r = \uparrow / \downarrow$. Wave vector Q, connecting both bands, is discussed in the text.

mixes helicity channels and ν is no longer a good quantum number once we add the impurity to the problem. However, we can rewrite $H_{wire} + H_{hyb}$ in a more convenient form by choosing another basis. The key here is to realize that the $|k\nu\rangle = c^\dagger_{k\nu}|0\rangle$ (see Eq. (3.17)) are eigenstates of the S_r component of the spin angular momentum pointing along the direction $\hat{\boldsymbol{r}} \equiv [\theta = \pi/2, \phi]$, for $s_k = +$, and along the opposite direction $-\hat{\boldsymbol{r}} \equiv [\theta = \pi/2, \phi + \pi]$, for $s_k = -$. Thus, $\hat{\boldsymbol{r}}$ determines the direction of what is conventionally called the effective "spin-orbit magnetic field" [21], i.e., $\boldsymbol{B}^{\text{eff}}_{\text{SOC}}(k) = |\gamma| \sin(k)\, \hat{\boldsymbol{r}}$ [see Eq. (3.18)], such that when k changes to $-k$ the effective magnetic field points in the opposite direction, thus conserving time-reversal symmetry. Note that, in this context, 'up' and 'down' refers to spin quantization 'along $\hat{\boldsymbol{r}}$', where $\hat{\boldsymbol{r}}$ lays on the xy plane,

somewhere in its first quadrant, depending on the ratio α/β. Thus, as we will see next, for finite-SOC, the presence of the impurity will make it advantageous to work in the S_r basis, with spin quantum number σ_r.

The ground state of the Kondo regime is a singlet formed between the impurity and the conduction electrons, whose spins in the finite-SOC QW are good quantum numbers when quantized along the $\hat{\boldsymbol{r}}$ direction. As a consequence, it is natural to expect that it will be advantageous to choose a quantization axis along $\hat{\boldsymbol{r}}$ for the impurity as well. Thus, if we take $\hat{\boldsymbol{r}} \equiv [\theta = \pi/2, \phi]$ as the spin quantization axis for the impurity, then the spin up ($\sigma_r = \uparrow \equiv +$) and spin down ($\sigma_r = \downarrow \equiv -$) impurity states are given by $d^\dagger_{\sigma_r} = 1/\sqrt{2}(d^\dagger_\uparrow + \sigma_r e^{i\phi} d^\dagger_\downarrow)$, where $d^\dagger_{\sigma_r}(d_{\sigma_r})$ creates (annihilates) an electron at the impurity with spin σ_r, quantized along the $\hat{\boldsymbol{r}}$ direction, with the understanding that when σ_r appears as a subscript it means $(\uparrow, \downarrow)$, and when it appears in an equation it means $(+, -)$, respectively.

The total Hamiltonian in this new basis is written as

$$H = \sum_{k,\sigma_r} \epsilon_{k\sigma_r} c^\dagger_{k\sigma_r} c_{k\sigma_r} + \sum_{\sigma_r} \epsilon_d n_{d\sigma_r} + \sum_{\sigma_r} U\ n_{d\sigma_r} n_{d\bar{\sigma}_r} + \sum_{k,\sigma_r} \Upsilon \left(c^\dagger_{k\sigma_r} d_{\sigma_r} + d^\dagger_{\sigma_r} c_{k\sigma_r} \right), \tag{3.19}$$

where $n_{d\sigma_r} = d^\dagger_{\sigma_r} d_{\sigma_r}$ is the impurity number operator, $c^\dagger_{k\sigma_r}(c_{k\sigma_r})$ creates (annihilates) an electron at the Fermi sea with momentum k and spin σ_r, $\Upsilon = (V^2 + |\gamma_{imp}|^2)^{1/2}$, and the QW dispersion is given by

$$\epsilon_{k\sigma_r} = -2\sqrt{t^2 + |\gamma|^2} \cos\left(k - \sigma_r \varphi\right) + \mu, \tag{3.20}$$

where $\varphi = \tan^{-1}(|\gamma|/t)$. Each one of the bands in the dispersion $\epsilon_{k\sigma_r}$, displaced from each other along the k-axis by $Q = 2\varphi$, is associated to one of the S_r eigenvalues $\sigma_r = \uparrow, \downarrow$, as shown in Fig. 3.3(c).

As mentioned above, it is the choice of $\hat{r}$, with polar angle $\phi = \tan^{-1}\alpha/\beta$ [1], as the quantization axis for all spins (conduction electrons and impurity alike), that renders the SIAM Hamiltonian in a particularly simple form (Eq. (3.19)), *almost* SU(2) sym-

[1] Since both α and β are positive definite, then $0 \leq \phi \leq \pi/2$.

metric. To understand why is that so, let us look at Fig. 3.4, depicting the dispersion relation for vanishing α and finite β, thus $\phi = 0$. The SOC effective magnetic field B_{SOC} (green arrow) seen by $k > 0$ electrons points along the QW, in the positive direction. Thus, choosing the S_r basis for the conduction electrons results in two possibilities: $|\uparrow_r\rangle$ electrons (red arrow) will have energy $\epsilon_k - B_{SOC}$ [2] (red curve in Fig. 3.4, $k > 0$ branch) and $|\downarrow_r\rangle$ electrons (blue arrow) will have energy $\epsilon_k + B_{SOC}$ (blue curve, $k > 0$ branch). Note that for electrons with $k = 0$, $B_{SOC} = 0$, thus the red and blue curves cross at $k = 0$. On the other hand, $k < 0$ electrons see a B_{SOC} pointing in the *negative* direction of the QW (as mandated by time-reversal symmetry). Thus, the situation now is reversed: $|\uparrow_r\rangle$ electrons will have energy $\epsilon_k + B_{SOC}$ (red curve, $k < 0$ branch) and $|\downarrow_r\rangle$ electrons will have energy $\epsilon_k - B_{SOC}$ (blue curve, $k < 0$ branch).

Thus, contrary to what was said above, in general terms, viz., that for finite-SOC the conduction electron spin is not a good quantum number, in 1D this is not the case. That is so because B_{SOC} points along a single orientation, $\hat{r}$ (into the positive direction for $k > 0$ and the negative direction for $k < 0$). Thus, choosing a spin quantization axis along $\hat{r}$ results in energy states with well defined spin orientation (Figs. 3.3(c) and 3.4). Obviously, one cannot say that SU(2) symmetry was restored by this choice of basis, because $\epsilon_{k\sigma_r}$ depends on σ_r [see Eq. (3.20)], as can be clearly seen in Figs. 3.3(c) and 3.4. The advantage of this choice of spin basis is that, now, there is no spin-flip term anywhere in the SIAM Hamiltonian, Eq. (3.19).

In principle, Eq. (3.19) looks very similar to the original SIAM, but, the important question, regarding the Kondo effect, is 'how does the hybridization function depend on the quantum number σ_r?' The answer to this question will be discussed below.

3.4 Time-reversal and the hybridization function

It is well known that the hybridization function (which determines the properties of the Kondo state [66]) for the zero-SOC SIAM is a spin-independent scalar function, denoted by $\Delta(\omega)$. As the Hamiltonian shown in Eq. (3.19) is similar to that for the zero-SOC SIAM, one may be led to assume that this is still the case for the finite-SOC hybridization function. However, there is an important detail in Eq. (3.19): the QW

[2] Where we have taken the electron magnetic moment $\mu = 1$.

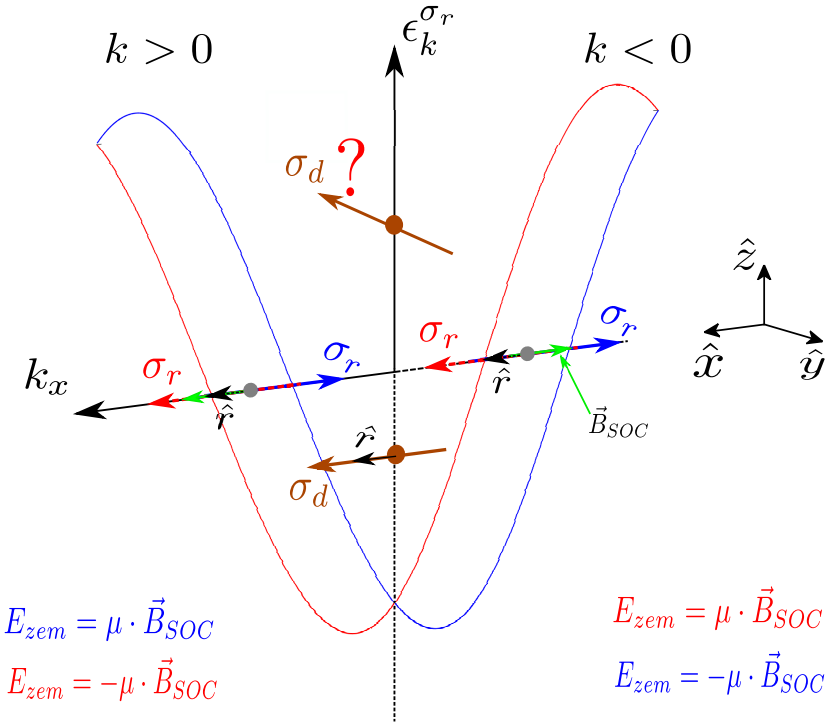

Figure 3.4: Dispersion relation (3.20) for quantization axis along the $\hat{r}$ axis. Here, $\sigma_r = \uparrow, \downarrow$ indicates the spin projection along the $\hat{r}$ axis. The red curve shows $\epsilon_{k,\uparrow_r}$, and the blue color is for $\epsilon_{k,\downarrow_r}$. The red and blue arrows represent the spin of the conduction electrons, the green arrow represents the magnetic field $\vec{B}_{soc}$, the brown arrow is the spin impurity, and the black arrow indicates $\hat{r}$. E_{zeem} gives the corresponding Zeeman energies.

dispersion $\epsilon_{k\sigma_r}$ *is* spin dependent [see Eq. (3.20) and Fig. 3.3(c)], which may imply that the hybridization function is spin dependent. A simple numerical calculation shows that this is not the case [see Fig. 3.5].

A general argument shows that time-reversal symmetry requires the finite-SOC SIAM hybridization matrix $\tilde{\Delta}_{\sigma\sigma'}(\omega)$ to be diagonal and spin-independent for any spin orientation σ along an arbitrary quantization axis, like the one for the zero-SOC SIAM [66] (we add a $\tilde{}$ to the hybridization function to indicate that we are treating the finite-SOC case). Indeed, the matrix elements of the 2×2 hybridization matrix can be written as $\tilde{\Delta}_{\sigma\sigma'}(\omega) = \sum_k \Sigma_{\sigma\sigma'}(k, \omega)$, where $\Sigma_{\sigma\sigma'}(k, \omega) = \Upsilon^2 G^{wire}_{\sigma\sigma'}(k, \omega)$, and $G^{wire}_{\sigma\sigma'}(k, \omega)$ is the single-particle Green's function for the QW. An analysis of the expressions for the matrix elements $\Sigma_{\sigma\sigma'}(k, \omega)$ indicates that their parity, in relation to k, can be readily obtained from Eq. (3.11): no-spin-flip terms $\Sigma_{\sigma\sigma}(k, \omega)$, produced by the first term in H_{wire}, which is associated to the kinetic energy $p^2/2m$, are even in k and spin independent, while non-diagonal spin-flip terms $\Sigma_{\sigma\bar{\sigma}}(k, \omega)$ are produced by the (SOC)

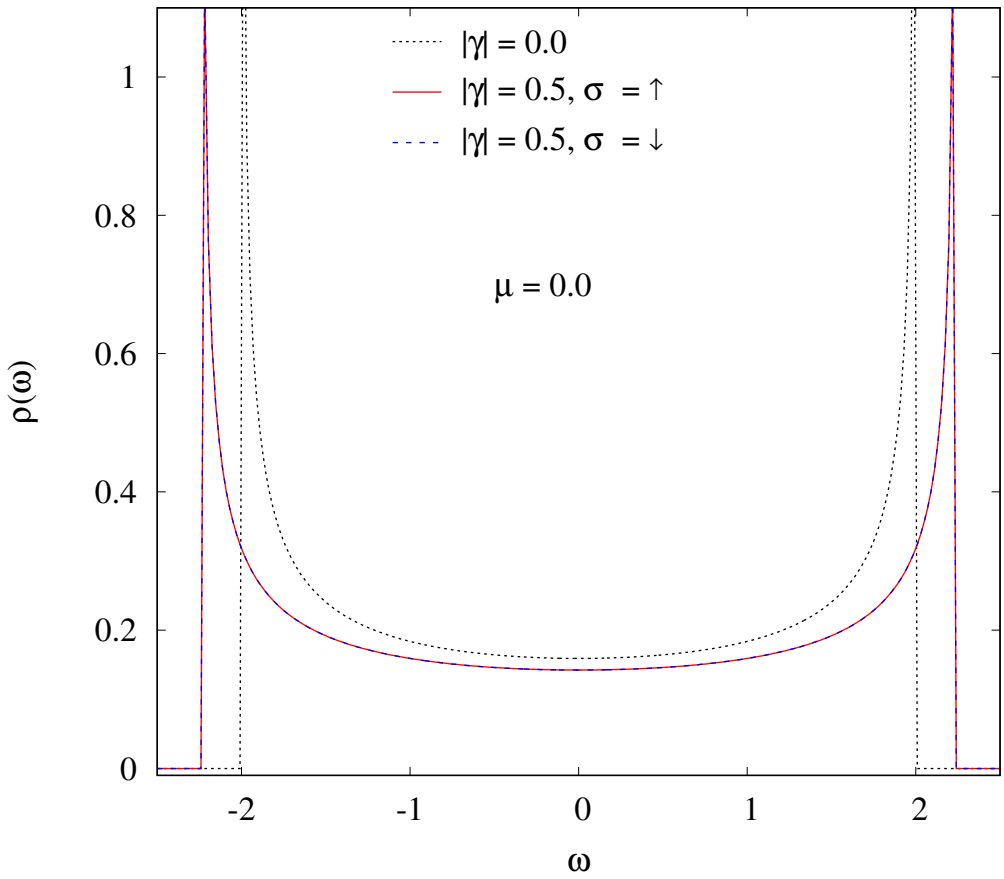

Figure 3.5: DOS $\rho(\omega) = -\mathrm{Im}\Delta_{\sigma\sigma}(\omega)/(\pi\Upsilon^2)$ with and without SOC. The dotted black curve corresponds to zero-SOC ($|\gamma| = 0$) and the solid/dashed (red/blue) curves correspond to $|\gamma| = 0.5$, for $\sigma = \uparrow / \downarrow$, for an arbitrary spin quantization axis. All results are shown for $\mu = 0$.

second term in H_{wire}, which, *to preserve time-reversal symmetry*, has to be odd in k. Thus, integrating $\Sigma_{\sigma\sigma'}(k,\omega)$ in k to obtain $\tilde{\Delta}_{\sigma\sigma'}(\omega)$ results in $\tilde{\Delta}_{\uparrow\uparrow}(\omega) = \tilde{\Delta}_{\downarrow\downarrow}(\omega) = \tilde{\Delta}(\omega)$ and $\tilde{\Delta}_{\uparrow\downarrow}(\omega) = \tilde{\Delta}_{\downarrow\uparrow}(\omega) = 0$. Therefore, as previously advertised, the spin independence of the hybridization function for the finite-SOC SIAM (despite the broken spin SU(2) symmetry) is guaranteed by the time-reversal symmetry. To illustrate these results, $-\mathrm{Im}\Delta_{\sigma\sigma}(\omega)/(\pi\Upsilon^2) = \rho(\omega)$ is plotted in Fig. 3.5 for finite-SOC (solid/dashed (red/blue) curve for an arbitrary spin orientation $\sigma = \uparrow / \downarrow$), and, as expected, it does not depend upon the spin orientation.

3.5 Pseudo-spin SU(2) symmetry

Due to the fact that the dispersion relation in Eq. (3.20) satisfies the identity $\epsilon_{k\sigma_r} = \epsilon_{k+Q\bar{\sigma}_r}$, which guarantees that a 2D Fermi sea has a pseudo-spin SU(2) symmetry (when $\alpha = \beta$) [96], we have analyzed if this is the case too for our system. To accomplish that, we generalize the problem to treat the Anderson model by introducing the spinor operators (in the σ_r basis) $\boldsymbol{c}^{\dagger}_{kQ} = \{c^{\dagger}_{k\uparrow} \;\; c^{\dagger}_{k+Q\downarrow}\}$ and $\boldsymbol{d}^{\dagger}_{r} = \{d^{\dagger}_{\uparrow r} \;\; d^{\dagger}_{\downarrow r}\}$, and with them construct the operators $2\boldsymbol{S}^{i}_{Q} = \sum_k \boldsymbol{c}^{\dagger}_{kQ}\boldsymbol{\sigma}^{i}\boldsymbol{c}_{kQ} + \boldsymbol{d}^{\dagger}_{r}\boldsymbol{\sigma}^{i}\boldsymbol{d}_{r}$, where the $\boldsymbol{\sigma}^{i}$ are the Pauli matrices and $Q = 2\varphi$ [see Eq. (3.20)]. These operators obey the angular momentum commutation relations $[\boldsymbol{S}^{i}_{Q}, \boldsymbol{S}^{j}_{Q}] = i\varepsilon^{ijl}\boldsymbol{S}^{l}_{Q}$, where ε^{ijl} is the Levi-Civita symbol. It can be shown that the $\boldsymbol{S}^{i}_{Q}$ (for $i = x, y, z$) commute with the finite-SOC SIAM Hamiltonian. Note that, as in Ref. [96], the commutation $[\boldsymbol{S}^{i}_{Q}, H] = 0$ is satisfied because of the equality $\epsilon_{k+Q\sigma_r} = \epsilon_{k\bar{\sigma}_r}$, when $Q = 2\varphi$ [see Eq. (3.20) and Fig. 3.3(c)] showing that our Hamiltonian is pseudo-spin SU(2) symmetric. Thus, the operators $\boldsymbol{S}^{i}_{Q}$ are the generators of the symmetry operations connected to the PSH states [96], which the authors believe may be associated with the structure of the Kondo cloud formed in our system, as observed in a previous work on Topological Insulators (see Fig. 10(a) in Ref. [97]).

Chapter 4

Thermoelectric properties

To calculate the TE transport properties of a QD in a steady-state condition, we apply a small external bias voltage $\Delta V = V_L - V_R$ and a small temperature difference $\Delta T = T_L - T_R$ between the left (hot) and the right (cold) leads. In linear response theory, a current $J_{\alpha'}$ will flow through the system under the action of a temperature gradient $\vec{\nabla}T$ and/or an electric field $\vec{E} = -\vec{\nabla}V$, where $\alpha' = e$ indicates a charge current J_e, while $\alpha' = Q$ indicates a heat current J_Q. The TE properties calculations follow standard textbooks [98, 99]. The electrical and thermal conductances, $G(T)$ and $K_e(T)$, respectively, as well as the thermopower $S(T)$ (Seebeck coefficient) are given by [100]

$$G(T) = -\lim_{\Delta V \to 0} \left(J_e/\Delta V\right)_{|\Delta T=0} = e^2 \mathcal{L}_0(T), \tag{4.1}$$

$$\begin{aligned} K_e(T) &= -\lim_{\Delta T \to 0} \left(J_Q/\Delta T\right)_{|J_e=0} \\ &= \frac{1}{T}\left(\mathcal{L}_2(T) - \frac{\mathcal{L}_1^2(T)}{\mathcal{L}_0(T)}\right), \end{aligned} \tag{4.2}$$

$$S(T) = -\lim_{\Delta T \to 0} \left(\Delta V/\Delta T\right)_{|J_e=0} = \left(\frac{-1}{eT}\right)\frac{\mathcal{L}_1(T)}{\mathcal{L}_0(T)}, \tag{4.3}$$

where, to calculate the transport coefficients $\mathcal{L}_0(T)$, $\mathcal{L}_1(T)$, and $\mathcal{L}_2(T)$, we follow Ref. [101], where expressions for the particle current and thermal flux, for a QD, were derived within the framework of Keldysh non-equilibrium Green's functions. Thus, the TE transport coefficients were obtained under temperature and voltage gradients, with

the Onsager relations automatically satisfied, in the linear regime. The TE transport coefficients (for $n = 0, 1, 2$) consistent with the general TE formulas derived above are given by

$$\mathcal{L}_n(T) = \frac{2}{h} \int \left(-\frac{\partial f(\omega, T)}{\partial \omega} \right) \omega^n \tau(\omega, T) d\omega, \tag{4.4}$$

where $\tau(\omega, T)$ is the transmittance for electrons with energy $\epsilon = \hbar\omega$ and temperature T, while $f(\omega, T)$ is the Fermi-Dirac distribution function.

For ordinary metals, the Wiedemann-Franz law states that the ratio between the electronic contribution to the thermal conductance $K_e(T)$ and the product of temperature T and electrical conductance $G(T)$,

$$L = \frac{K_e(T)}{TG(T)}, \tag{4.5}$$

is independent of temperature and takes a universal value given by the Lorenz number $L_o = (\pi^2/3)(k_B/e)^2$, where k_B is the Boltzmann constant and $-e$ is the electron charge. Note that, in the calculations that follow, we present the Wiedemann-Franz law in units of L_o,

$$WF = \frac{L}{L_o}, \tag{4.6}$$

so that it is easy to spot deviations from what is expected for ordinary metals, i.e., $WF = 1$.

The slow evolution of Thermoelectricity is related to the difficulties to find TE materials that exhibit higher dimensionless TE figure of merit ZT and power factors PF_0, at the same time [8, 50]. These quantities give a measure of the efficiency of the device as a function of the temperature T and are defined by

$$ZT = S^2TG/K \qquad PF_0 = S^2G, \tag{4.7}$$

In ordinary metals, both $G(T)$ and $K(T)$ are related to the same electronic scattering processes, with only weak energy dependence, and satisfying the Wiedemann-Franz law, which is the main reason why metals show lower ZT values. However, higher ZT alone is necessary but not sufficient to define the usefulness of a TE device. In addition to this, the power factor S^2G, which is a measure of the maximum power that a TE

device can produce [50], should be higher. Both quantities act as guides to the experimental work in the area. We could have a good TE system when the power factor is maximized, and the K is minimized. However, it is not easy to maximize the heat conversion because those TE properties are closely related.

Employing Eqs. (4.5) to (4.7), we can write ZT as a function of the thermopower S and the Wiedemann-Franz law WF [expressed in units of L_o, as in Eq. (4.6)]

$$ZT = \frac{S^2}{WF}. \tag{4.8}$$

This equation shows that violations of the Wiedemann-Franz law can lead to an effective increase of ZT in regions where $WF < 1$, as long as there is no concomitant decrease in the thermopower S.

The behavior of the TE coefficients is governed by the transmittance $\tau(\omega, T)$ [see Eq. (4.4)]. For a QD in an immersed (or embedded) geometry, it can be written in terms of the QD Green's function as

$$\tau(\omega, T) = \Gamma \Im[G_d(\omega, T)], \tag{4.9}$$

where $\Gamma_\gamma = \pi V^2 \rho^c(\mu)$, with $\rho^c_{\sigma_r}(\mu)$ being the spin-orbit dependent leads' DOS at the Fermi energy, and $\Im$ indicates the imaginary part.

Chapter 5

Atomic approach method

The main objective of this chapter is to present the atomic approach [7, 102] as an alternative to study nanoscopic systems that exhibit the Kondo effect. Due to the simplicity of its implementation (practically all the method is analytical) and very low computational cost (a density of states curve can be obtained in few seconds or less), the atomic approach is a good candidate to describe strongly correlated impurity systems that exhibit Kondo effect, like the quantum dots. Although the Kondo temperature obtained by the present method shows a considerable deviation from the exact exponential behavior, the results obtained for both the localized density of states at the chemical potential and dynamical properties (like the conductance) agree very well with those obtained by the numerical renormalization group formalism [8]. This result is a consequence of the satisfaction of the Friedel sum rule by the atomic approach in the Kondo limit.

Another point that should be stressed is that the present method, due to its simplicity is not able to take into account all the Kondo physics behind the Anderson impurity as it is done by other powerful and complex methods, like the numerical renormalization group (NRG) [8]. The present method is a simple and semi-analytical technique that should be used as the first choice to calculate the dynamical properties of the Anderson impurity systems, because it can describe the emergence of the Kondo peak at low temperatures in the Kondo regime qualitatively.

5.1 Model and theory

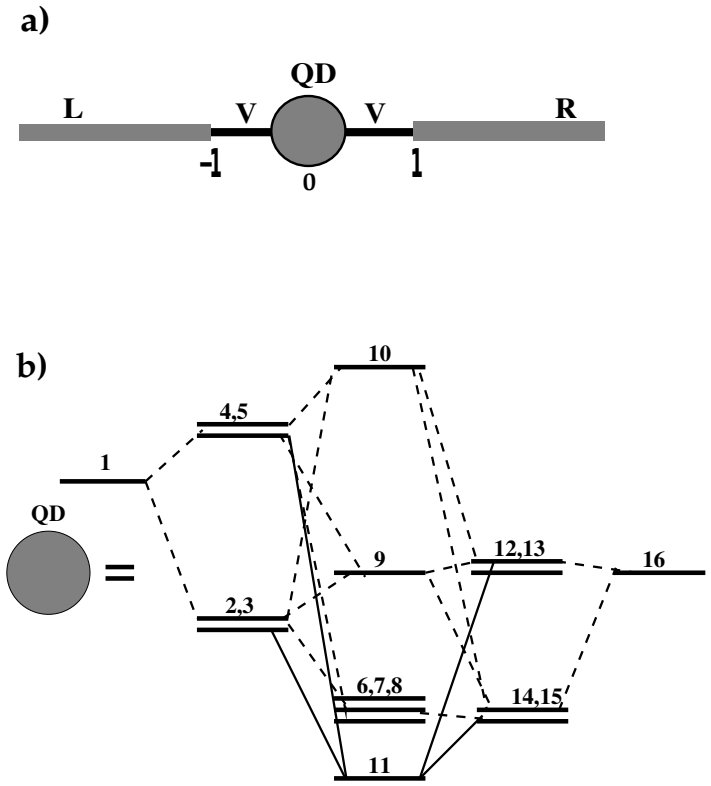

Figure 5.1: (a) Schematic picture of the SET. A quantum dot embedded into conduction leads and (b) Details of the eigenstates structure of the atomic solution generated through the atomic approach in the Kondo regime [7].

In Figure 5.1a, we present a pictorial view of a quantum dot for the immersed case. In Figure 5.1b, we represent the eigenstates of the atomic solution, which are the "seed" employed to calculate the Green's functions of the atomic approach (in this chapter, we are working on the base σ_r at all time, that is $\sigma_r \to \sigma$). Those Green's functions have the general form [7]:

$$g_{\sigma}^{f,at}(\omega) = e^{\beta\Omega} \sum_{i=1}^{16} \frac{m_i}{\omega - u_i}, \tag{5.1}$$

where Ω is the thermodynamic potential, the poles u_i in the denominator, are the energy eigenvalues associated with the energy levels, and the residues m_i in the numerator are the occupation numbers associated with the atomic transitions. In the diagram, we indicate transitions with null residues ($m_i = 0$), with dashed lines and transitions with non-null residues ($m_i \neq 0$) with solid lines, but as the temperature or the other parameters of the model change, the residues of the Green's functions change as well,

and the dotted lines can become solid lines and vice-versa. The resultant eigenstate structure of the QD corresponds to the atomic solution of the periodic Anderson model (PAM), (For more details cf. Figure 20 and the appendix of Ref. [7]).

This particular eigenstate structure corresponds to the Kondo limit at a temperature T, below the Kondo temperature T_K. The Kondo singlet ground state is given by the level 11, and the transitions represented by the complete lines produce non-null residues for the atomic Green's functions, which give rise to the Kondo peak. The transitions represented by dashed lines vanish in the Kondo region. This QD eigenstate structure is not static but instead changes with temperature, and the QD localized energy level $E_{f\sigma}$, follows the different regimes of the SIAM: empty dot, intermediate valence, Kondo, and double occupation.

The Hamiltonian of the system can be written as

$$H = \sum_{\mathbf{k},\sigma} \sum_{s=L,R} (E^s_{\mathbf{k},\sigma} - \mu) c^{s\dagger}_{\mathbf{k},\sigma} c^s_{\mathbf{k},\sigma}$$

$$+ \sum_{\sigma} [(E_{f\sigma} - \mu) X_{\sigma\sigma} + (2E_{f\sigma} + U - 2\mu) X_{dd}]$$

$$+ \sum_{s=L,R} \sum_{\mathbf{k},\sigma} V_s \left(X^{\dagger}_{0\sigma} c^s_{\mathbf{k},\sigma} + c^{s\dagger}_{\mathbf{k},\sigma} X_{0\sigma} \right), \tag{5.2}$$

where the first term represents the leads, characterized by an electronic (c-electrons) conduction band, where the spin-orbit coupling is taken into account and is included inside the $E^s_{\mathbf{k},\sigma}$ electrons to the right (R) and the left (L) of the QD (Figure 5.1a). The second term describes the QD defined by a two-level structure: one localized bare level $E_{f\sigma} = E_{QD} - \mu$ and the local Coulomb interaction of the QD, characterized by the double occupation level at $2E_{QD} + U - 2\mu$, where μ is the chemical potential [7, 102]. These localized levels are expressed in the representation of Hubbard operators, which are convenient for working with correlated local states and are defined in general by $X_{p,ab} =\mid p, a >< p, b \mid$. We would like to mention that the atomic approach "dresses" this simple two-level QD, incorporating into it the "eigenstate structure" represented in Figure 5.1b.

Finally, the third term corresponds to the tunneling between the embedded dot

and the left (L) and right (R) semi-infinite leads. The amplitude V_s is responsible for the tunneling between the QD and the lead s. For simplicity, we assume symmetric junctions (i.e., $V_s = V_L = V_R = V$) and identical leads connecting the QD to the quantum wire.

The identity relation in the reduced space of the localized states at the QD site, expressed in terms of the Hubbard operators, is

$$X_{00} + X_{\sigma\sigma} + X_{\overline{\sigma}\overline{\sigma}} + X_{dd} = I, \tag{5.3}$$

where I is the identity operator. Associated with this relation, the occupation numbers for the QD are calculated by

$$n_a = \langle X_{aa} \rangle = \left(\frac{-1}{\pi}\right) \int_{-\infty}^{\infty} d\omega Im(G^f_{o\sigma}(z)) n_F(\omega), \tag{5.4}$$

where $G^f_{o\sigma}(z)$ is the localized QD Green function and $n_F = 1/(1 + \exp(\beta\omega))$ is the Fermi-Dirac distribution, with $z = \omega + i\eta$. In the numerical calculations, we employ $\eta = 10^{-4}$. The QD occupation numbers satisfy the "completeness" relation.

$$n_0 + n_\sigma + n_{\overline{\sigma}} + n_{dd} = 1. \tag{5.5}$$

where n_o represents the empty states, $(n_\sigma, n_{\overline{\sigma}})$ are the singly occupied states, and n_d represents the double occupied states.

5.2 The atomic approach for the single impurity Anderson model (SIAM)

The exact GF for the f electrons, which is valid both for the PAM and the SIAM, can be written in the form of a Dyson equation [7]

$$\mathbf{G}^f_\sigma = \mathbf{M}_\sigma \cdot (\mathbf{I} - \mathbf{A}_\sigma)^{-1}, \tag{5.6}$$

where $\mathbf{A}_\sigma = \mathbf{W}_\sigma \cdot \mathbf{M}_\sigma$ and $\mathbf{M}_\sigma$ are the exact effective cumulants. Inverting Eq. 5.6, we obtain

$$\mathbf{M}_\sigma = \left(\mathbf{I} + \mathbf{G}^f_\sigma \cdot \mathbf{W}_\sigma\right)^{-1} \cdot \mathbf{G}^f_\sigma, \tag{5.7}$$

and for an impurity located at the origin $\mathbf{W}_\sigma$ is given by

$$\mathbf{W}_\uparrow(z) = |V|^2 \varphi_\uparrow(z)\mathbf{I}, \tag{5.8}$$

$$\mathbf{W}_\downarrow(z) = |V|^2 \varphi_\downarrow(z)\mathbf{I}', \tag{5.9}$$

where

$$\mathbf{I} = \begin{pmatrix} 1 & 1 \\ 1 & 1 \end{pmatrix} \quad , \quad \mathbf{I}' = \begin{pmatrix} 1 & -1 \\ -1 & 1 \end{pmatrix}. \tag{5.10}$$

For a tight-binding one-dimensional chain we have the unperturbed conduction band

$$\rho_\sigma(\omega) = \frac{1}{\pi\sqrt{4(t^2 + |\gamma|^2) - \omega^2}}, \tag{5.11}$$

where μ is the chemical potential and γ is the spin-orbit coupling strength.

Since the calculation of the exact effective cumulant $\mathbf{M}_\sigma$ is equivalent to obtaining the exact Green's functions [7, 102], we introduce an approximation that consists of substituting the exact effective cumulant in the Green's functions with the approximated ones, obtained from the atomic solution of the model, which is associated with the transitions described by the Hubbard operators. We employ the index $I_x = 1, 2, 3, 4$, defined in Table I, to characterize these X operators:

I_x	1	2	3	4
$\alpha = (b, a)$	$(0, \uparrow)$	$(0, \downarrow)$	$(\downarrow, d)$	$(\uparrow, d)$

(5.12)

Table I: Representation of the possible transitions present in the finite U atomic SIAM

Hamiltonian. $I_x = 1, 3$ destroys one electron with spin up, and $I_x = 2, 4$ destroys one electron with spin down.

In the atomic approach, those approximated GF's become

$$\mathbf{G}^f_{\uparrow}(i\omega) = \frac{\mathbf{M^{at}_{13}}(i\omega) - |V|^2 \varphi_{\uparrow}(i\omega) R^{13}\mathbf{I'}}{1 - |V|^2 \varphi_{\uparrow}(i\omega) S^{13}}, \tag{5.13}$$

with $R^{13} = m_{11}m_{33} - m_{13}m_{31}$ and $S^{13} = m_{11} + m_{33} + m_{13} + m_{31}$, and

$$\mathbf{G}^f_{\downarrow}(i\omega) = \frac{\mathbf{M^{at}_{24}}(i\omega) - |V|^2 \varphi_{\downarrow}(i\omega) R^{24}\mathbf{I}}{1 - |V|^2 \varphi_{\downarrow}(i\omega) S^{24}}, \tag{5.14}$$

with $R^{24} = m_{22}m_{44} - m_{24}m_{42}$ and $S^{24} = m_{22} + m_{44} + m_{24} + m_{42}$, and

$$\mathbf{M^{at}_{13}}(i\omega) = \begin{pmatrix} m^{at}_{11} & m^{at}_{13} \\ m^{at}_{31} & m^{at}_{33} \end{pmatrix}, \tag{5.15}$$

$$\mathbf{M^{at}_{24}}(i\omega) = \begin{pmatrix} m^{at}_{22} & m^{at}_{24} \\ m^{at}_{42} & m^{at}_{44} \end{pmatrix}, \tag{5.16}$$

are the atomic cumulants calculated from the atomic Green's functions (For more details cf. section III and the appendix of our Ref. [7]). In the same way, we can obtain the conduction $\mathbf{G}^{cc}_{\sigma}(\mathbf{k}, \mathbf{k'}, i\omega)$ and the cross $\mathbf{G}^{cf}_{\sigma}(\mathbf{k}, i\omega)$ Green's functions.

The exact atomic Green's function $g^{f,at}_{\sigma}(z)$ of the atomic problem satisfies a Dyson equation of the same form as Eq. 5.6, but now in terms of the atomic cumulants given by Eqs. 5.15 and 5.16

$$\mathbf{g}^{f,at}_{\sigma} = \mathbf{M^{at}_{\sigma}} \cdot \left(\mathbf{I} - \mathbf{W^{o}_{\sigma}} \mathbf{M^{at}_{\sigma}}\right)^{-1}. \tag{5.17}$$

It should be stressed that $\mathbf{g}^{f,at}_{\sigma}$ is known and it is obtained from the exact analytical diagonalization of a 16×16 matrix, which represents the atomic solution of the periodic Anderson Hamiltonian (For more details cf. the appendix of our reference [7]) . From this equation we obtain the exact atomic cumulant

$$\mathbf{M}_{\sigma}^{at} = \left(\mathbf{I} + \mathbf{g}_{\sigma}^{f,at} \cdot \mathbf{W}_{\sigma}^{o}\right)^{-1} \cdot \mathbf{g}_{\sigma}^{f,at}, \tag{5.18}$$

where

$$\mathbf{W}_{\uparrow}^{o}(z) = |\Gamma|^2 \, \varphi_{\uparrow}^{o}(z) \;\; ; \;\; \mathbf{W}_{\downarrow}^{o}(z) = |\Gamma|^2 \, \varphi_{\downarrow}^{o}(z)\mathbf{I}, \tag{5.19}$$

and

$$\varphi_{\sigma}^{o}(z) = \frac{-1}{z - \varepsilon_o - \mu}. \tag{5.20}$$

This equation corresponds to the zero-width band located at ε_0, namely the bare conduction Green's function. The atomic cumulant M_{σ}^{at}, (Eq. 5.18) is obtained by replacing Eqs. 5.19-5.20 in Eq. 5.18. The full Green's functions $\mathbf{G}_{\sigma}^{f}$ are calculated by substituting the cumulants obtained in this way in Eqs. 5.13 and 5.14. This procedure overestimates the contribution of the c electrons, because we concentrate them at a single energy level ε_o, and to moderate this effect we replace V^2 in Eq. 5.19, with the Anderson parameter $\Gamma = \pi V^2 \rho_c(\mu)$, with $\rho_c(\mu)$ being the density of states of the spin-orbit conduction band given by Eq. 5.11.

We should stress that in the low temperature regime the atomic approach imposes the fulfillment of the Friedel sum rule, but for temperatures above the Kondo temperature T_K, as happens in the present paper for $T \simeq \Gamma$, we do not apply this procedure; we only put the conduction atomic level of Eq. 5.20 at the chemical potential position, $\varepsilon_0 = \mu$.

Chapter 6

Numerical renormalization group (NRG)

Introduction

After Jun Kondo's initial work in the magnetic impurity problem [79] (see the first section of Chap. 2 for details), it was shown that perturbation theory fails at energy scales lower than the Kondo temperature. Another method that tried to solve the so-called 'Kondo problem' was Anderson's Poor man's scaling approach [103], which was also unsuccessful, although it showed a new direction to be explored (scaling and renormalization ideas). The method that successfully solves the Kondo problem is the Numerical Renormalization Group (NRG) method [86]. The NRG method was built on the basis of Anderson's scaling and renormalization ideas, and later it was generalized to other quantum systems, as well as to the Anderson impurity model [104], and impurities immersed in bosonic baths [105]. With the NRG method, one can calculate the dynamic and thermodynamic properties at zero temperature, as well as at finite temperatures, for strongly correlated Kondo-type systems.

In this chapter, we will describe the general concepts of the NRG method for the Anderson impurity model. Starting with the continuous representation of Anderson's Hamiltonian, it is followed by a discretization procedure and a mapping to a chain Hamiltonian, the so-called 'Wilson chain', which is then diagonalized iteratively. Details of the method can be found in the Refs. [66, 104, 106].

6.1 NRG strategies

Conventionally, the description of the NRG method is made on the Anderson impurity model, and here it is no exception. Let us consider Anderson's model for a single impurity. This model describes a free-fermion bath, which is coupled to a quantum magnetic impurity (a quantum dot, for example). We copy here the Hamiltonian from Eq. (3.19) (but replace σ_r by σ)

$$H = H_d + \sum_{k,\sigma} \epsilon_{k\sigma} c^\dagger_{k\sigma} c_{k\sigma} + \sum_{k,\sigma} V_k \left(c^\dagger_{k\sigma} d_\sigma + d^\dagger_\sigma c_{k\sigma} \right). \tag{6.1}$$

The first term, H_d, corresponds to the quantum magnetic impurity, while the second term describes a free fermion conduction band, and the last term describes the coupling between them. The quantum impurity term H_d is given by

$$H_d = \sum_\sigma \epsilon_d n_{d\sigma} + \sum_\sigma U \; n_{d\sigma} n_{d\bar{\sigma}}. \tag{6.2}$$

The full description of Eq. 6.1 can be found in section 3.3, where here, for simplicity's sake, we make $\gamma_{imp} = 0$, keeping only the V_k coupling. The integral form of the Hamiltonian, according to Bulla *et al.* [66], is written as

$$H = H_d + \sum_\sigma \int_{-1}^{1} g(\epsilon) n_{\epsilon,\sigma} + \sum_\sigma \int_{-1}^{1} h(\epsilon)(d^\dagger_\sigma a_{\epsilon\sigma} + a^\dagger_{\epsilon\sigma} d_\sigma). \tag{6.3}$$

In the above, $g(\epsilon)$ is the generalized dispersion and $h(\epsilon)$ is the generalized hybridization [66]. The annihilation and creation operators $a_{\epsilon\sigma}$ and $a^\dagger_{\epsilon\sigma}$, defined in energy space, obey the usual fermionic anticonmutation relation $\{a^\dagger_{\epsilon\sigma}, a_{\epsilon\sigma}\} = 1$ as long as they are normalized by the density of states of the conduction band (the explicit relation between the creation and annihilation operators in the energy space ϵ and the corresponding k-space operators can be found in Ref. [104]). The generalized dispersion and the generalized hybridization are related by

$$\frac{\partial g_\sigma^{-1}(\epsilon)}{\partial \epsilon}[h_\sigma(g_\sigma^{-1}(\epsilon))]^2 = \rho_\sigma[V_\sigma(\epsilon)]^2. \tag{6.4}$$

Equation 6.4 allows a generalization of the NRG method to a non-constant density of states [107]. This 'trick' is important when the conduction band density of states presents van-Hove singularities close to the Fermi energy.

Panel (a) in Fig. 6.1 shows a schematic representation of the Hamiltonian in Eq. (6.1), where the box H_d represents the quantum impurity, $\rho(\epsilon_k)$ is the conduction band density of states, and the red region in the figure represents the hybridization V between H_d and $\rho(\epsilon_k)$. As depicted in panel (a), the entire width of the energy spectrum interacts with the impurity. Thus, applying the NRG method to a strongly correlated system involves considering the following: (i) As discussed in Ref. [86], all energy scales, up to the band-width $D = 1$, contribute to the properties of the ground state. (ii) As discussed in Ref. [79], all the physics of the system is governed by the low cut-off energy scale $k_B T_K/D$. This is typical of Renormalization Group problems. A clear example of which is the Kondo effect, where the Kondo temperature ($k_B T_K$), being exponentially smaller than the ratio of the Coulomb repulsion and the hybridization strength, requires a high energy-resolution in the vicinity of the Fermi energy.

Because of its implementation of a logarithmic discretization (see below), the NRG method allows one to obtain a high energy-resolution in the neighborhood of the Fermi level. The NRG method consists of a series of steps, as depicted in Fig. 6.1: In panel (a) we show an appropriate continuous representation of the Hamiltonian, in panel (b) we show a discretization of the continuum into logarithmic intervals, in panel (c) we show that the impurity properties can be described quite faithfully by keeping just a single state in each logarithmic interval, and in panel (d) we finally show the (exact) mapping of the problem to a one-dimensional chain, called Wilson chain. The renormalization calculation starts here in panel (d). Next, we are going to describe each of these steps qualitatively, since a detailed description can be found in the references cited in the introduction to this chapter.

Once the Hamiltonian is properly rewritten in the continuum, the next step is the logarithmic discretization of the conduction band in intervals $[-x_n, -x_{n+1} >$, for negative energies, and $< x_{n+1}, x_n]$, for positive energies. Λ is the discretization parameter that determines the position of the $x_n = D\Lambda^{-n}$ points in the conduction band, where $n = 0, 1, 2, \ldots$. The width of each interval is given by $d_n = x_n - x_{n+1} =$

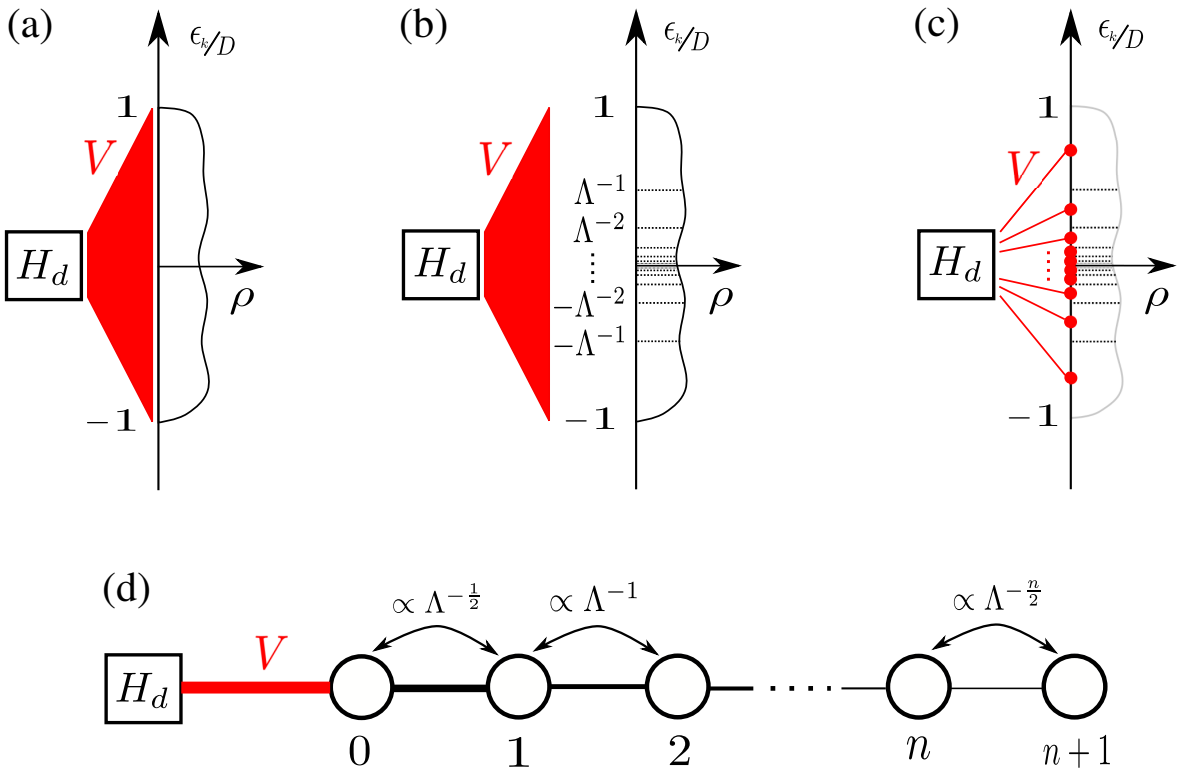

Figure 6.1: The NRG steps for the SIAM: the H_d square in (a) represents the impurity coupled to a continuous conduction band. (b) Logarithmic discretization of the conduction band. (c) Representation by a single state in each interval of the continuum. (d) Mapping of the model to a semi-infinite chain, so that the impurity is coupled just to the first site of the chain

$D(\Lambda^{-n}+\Lambda^{-(n+1)}) = \frac{D(\Lambda-1)}{\Lambda^{n+1}}$. The following step is to define a complete set of orthogonal functions within each interval

$$\psi^{\pm}_{np}(\epsilon) = \begin{cases} \frac{1}{\sqrt{d_n}} e^{\pm i\omega_n p\epsilon} & x_{n+1} < \pm\epsilon < x_n \\ 0 & else \end{cases} , \tag{6.5}$$

where the signs $+$ and $-$ mean that the orthogonal functions are defined for positive and negative energies, respectively, the integers $p \in \langle -\infty, \infty \rangle$, and the fundamental frequency of each interval is $\omega_n = \frac{2\pi}{d_n} = \frac{2\pi\Lambda^{n+1}}{D(\Lambda-1)}$.

After that, the conduction band annihilation operators $a_{\epsilon\sigma}$ are expressed in the basis functions defined in Eq. (6.5), for each interval

$$a_{\epsilon\sigma} = \sum_{np} [a_{np\sigma}\psi^{+}_{np}(\epsilon) + b_{np\sigma}\psi^{-}_{np}(\epsilon)]. \tag{6.6}$$

It can be shown that the impurity couples *directly* only to the $p = 0$ state in each interval, i.e., $\psi^{\pm}_{np=0}(\epsilon)$. Thus, here, the most severe approximation in NRG is done, viz., all the $p \neq 0$ states are discarded, since they couple to the impurity only indirectly (through the $p = 0$ states). Thus, each interval now contains a single state, and this is depicted in panel (c) of Fig. 6.1.

Thus, the Hamiltonian 6.1 has been transformed from the continuous representation to the discrete representation, from which the mapping of the system to the Wilson chain can be performed easily. It is well known that one can always tridiagonalize any sparse matrix using, for example, the Lanczos algorithm [108]. On the other hand, a tridiagonal matrix represents a Hamiltonian for a tight-binding chain with only nearest-neighbor hoppings. The important point to realize here is that, in our case, the first element of the tridiagonal (Lanczos) basis is given by the hybridization term in the discretized Hamiltonian (i.e., the orbital that couples to the impurity). Then, the Lanczos algorithm will create the rest of the basis, together with all the hoppings and orbital energies for each site of the Wilson chain. This is depicted in Fig. 6.1(d) and the tight-binding expression of the Hamiltonian for the Wilson chain is as follows

$$H = H_d + \sqrt{\frac{\xi_0}{\pi}} \sum_{\sigma} (d^{\dagger}_{\sigma} c_{0\sigma} + h.c) + \sum_{\sigma,n=0}^{\infty} [\epsilon_n c^{\dagger}_{n\sigma} c_{n\sigma} + t_n (c^{\dagger}_{n\sigma} c_{n+1\sigma} + h.c)], \tag{6.7}$$

where

$$\xi_0 = \int_{-1}^{1} d\varepsilon \Delta(\varepsilon). \tag{6.8}$$

Thus, the second term of Eq. 6.7 describes the coupling of the orbital in the first site of the Wilson chain (denoted $c_{0\sigma}$) to the impurity, and the third term is the Wilson chain itself, with $n = 0, 1, 2, 3 \ldots$ being the index of the Wilson chain sites. The hoppings of the Wilson chain decrease exponentially as $\Lambda^{-n/2}$.

This is where truly the renormalization group process begins, through an iterative

diagonalization process of the Hamiltonian. Within the ideas of the renormalization group, the Wilson chain Hamiltonian is interpreted as a series of Hamiltonians, where the next Hamiltonian in the series is obtained from the previous by adding an extra site to the Wilson chain. Thus, we have, for example, $H_1, H_2, \ldots H_N$ are Wilson chain's Hamiltonians for 1 site, 2 sites, ..., and N sites. We recover the initial Hamiltonian in the limit of $N \to \infty$

$$H = \lim_{N\to\infty} \Lambda^{-(N-1)/2} H_N, \tag{6.9}$$

where the full expression for H_N is given by

$$H_N = \Lambda^{(N-1)/2} \left(H_d + \sqrt{\frac{\xi_0}{\pi}} \sum_\sigma (d^\dagger_\sigma c_{0\sigma} + h.c) + \sum_{\sigma,n=0}^{N-1} [\epsilon_n c^\dagger_{n\sigma} c_{n\sigma} + t_n (c^\dagger_{n\sigma} c_{n+1\sigma} + h.c)] \right), \tag{6.10}$$

and the recursive relation that relates H_{N+1} to H_N is given by

$$H_{N+1} = \sqrt{\Lambda} H_N + \left(\sum_\sigma [\epsilon_{N+1} c^\dagger_{N+1\sigma} c_{N+1\sigma} + t_N (c^\dagger_{N\sigma} c_{N+1\sigma} + h.c) \right). \tag{6.11}$$

In each of these iteration steps an $N+1$ new site is added, and the Hamiltonian is diagonalized in this new enlarged Hilbert space.

6.2 "NRG Ljubljana" open-source numerical renormalization group code

The NRG-Ljubljana is a sophisticated open-source program designed to study quantum-impurity problems using the NRG method. It was developed by Prof. Rok Žitko from the Jožef Stefan Institute in Ljubljana, Slovenia. It is a highly cost-effective code in terms of computational cost and flexibility, which can be integrated with other

programming languages without losing computational efficiency. The NRG iteration calculations are performed in C++, the diagonalization is done through specialized libraries, and the processing of the results can be done in any other high-level language [109], or in any language one prefers. By default, the package has a library of Perl commands and functions that facilitate the handling of files, whether these files are text or numerical. Depending on the complexity of the problem to be studied, it allows the parallelization of the program. It allows us to study a great variety of problems besides the Kondo problem and the SIAM, which are the best known ones. For example, we can also study the periodic SIAM, the Hubbard model, Density Matrix NRG, superconductivity, and others. It also implements different 'flavors' of conduction band discretizations [110–112].

Chapter 7

Numerical Results

7.1 NRG result: Kondo Temperature under spin-orbit coupling

7.1.1 Renormalized Haldane expression

Through the application of Anderson's poor man's scaling approach [103] to the SIAM, different expressions for the Kondo temperature T_K can be found for a variety of parameter regimes [67]. All of them, collectively known as Haldane expression [95, 113], are proportional to an exponential $\exp\left({}^{\pi\epsilon_0(\epsilon_0+U)}/_{2\Delta U}\right)$ multiplied by a function of Δ, D, ϵ_0 and U, whose form depends on these parameters relative values. In the wide-band limit, i.e., $D \gg U, \Delta, |\epsilon_0|$, Haldane obtained (see Eq. [37] in Ref. [95])

$$T_K = 0.364 \left({}^{2\Delta U}/_{\pi}\right)^{\frac{1}{2}} \exp\left[\frac{\epsilon_0\left(\epsilon_0+U\right)}{{}^{2\Delta U}/_{\pi}}\right], \tag{7.1}$$

where $\Delta = \pi V^2 \rho\left(\epsilon_F\right)$ and $\rho\left(\epsilon_F\right)$ is the band DOS at the Fermi energy ϵ_F. As our Hamiltonian [Eq. (3.19)] is formally equivalent to the zero-SOC SIAM Hamiltonian used to obtain Eq. (7.1), the Haldane expression should be valid for our finite-SOC SIAM as well, but with band parameters renormalized by SOC (an SOC renormalized parameter will be denoted with a $\tilde{}$ on top of it). Indeed, as illustrated in Figure 3.5, which compares the DOS for $\gamma = 0.0$ (dotted black line) with that for $|\gamma| = 0.5$ (solid/dashed (red/blue) for $\sigma = \uparrow / \downarrow$), the bulk SOC γ increases the bandwidth and

thus decreases the DOS $\tilde{\rho}(\epsilon_F)$, at $\epsilon_F = 0$. Thanks to the analytical expression for $\epsilon_{k\sigma_r}$ [Eq. (3.20)], obtained through the spin rotation, we can derive a simple analytical expression for the renormalized semi-bandwidth

$$\tilde{D} = 2\sqrt{t^2 + |\gamma|^2}, \tag{7.2}$$

as well as for the band DOS at the Fermi energy $\tilde{\rho}(0) = 1/\left(2\pi\sqrt{t^2+|\gamma|^2}\right)$. Therefore, the renormalized hybridization function at half-filling $\tilde{\Delta} = \tilde{\Delta}(0)$ can be written as

$$\tilde{\Delta} = \pi\Lambda^2\tilde{\rho}(0) = \frac{V^2 + |\gamma_{imp}|^2}{2\sqrt{t^2 + |\gamma|^2}}. \tag{7.3}$$

Finally, replacing $\tilde{\Delta}$ for Δ in Eq. (7.1), the renormalized finite-SOC SIAM Kondo temperature $\tilde{T_K}$, in the wide-band limit, is given by

$$\tilde{T_K} = 0.364\left(2\tilde{\Delta}U/\pi\right)^{\frac{1}{2}} \exp\left[\frac{\epsilon_0(\epsilon_0+U)}{2\tilde{\Delta}U/\pi}\right]. \tag{7.4}$$

In particular, if one takes the $U \to \infty$ limit, one obtains [67]

$$\tilde{T_K} \propto \sqrt{\tilde{\Delta}\tilde{D}}\exp\left(\pi\epsilon_0/2\tilde{\Delta}\right), \tag{7.5}$$

where it should be noticed that, differently from the wide-band limit [Eq. (7.4)], the multiplicative constant in Eq. (7.5) is unknown. Through the renormalized infinite-U Haldane expression in Eq. (7.5), one can easily analyze the SOC impact over the Kondo temperature $\tilde{T_K}$ for a fixed value of ϵ_0. First, $\tilde{T_K}$'s prefactor depends on the local SOC term (γ_{imp}), but not on the bulk SOC (γ). Second (keeping in mind that, in the Kondo regime, $\epsilon_0 < \mu$, since $\epsilon_F = \mu$), Eq. (7.3), for the renormalized hybridization $\tilde{\Delta}$, implies that the local SOC γ_{imp}, by increasing $\tilde{\Delta}$, exponentially increases $\tilde{T_K}$, while the bulk SOC term γ exponentially decreases it, by decreasing $\tilde{\Delta}$.

Next, using NRG, we will numerically validate the analytical results obtained for the wide-band regime. In addition, we will compare our NRG results with the QMC results in Ref. [62], for the intermediate regime, $U = D > \Delta$, with the Fermi energy close to the bottom of the band.

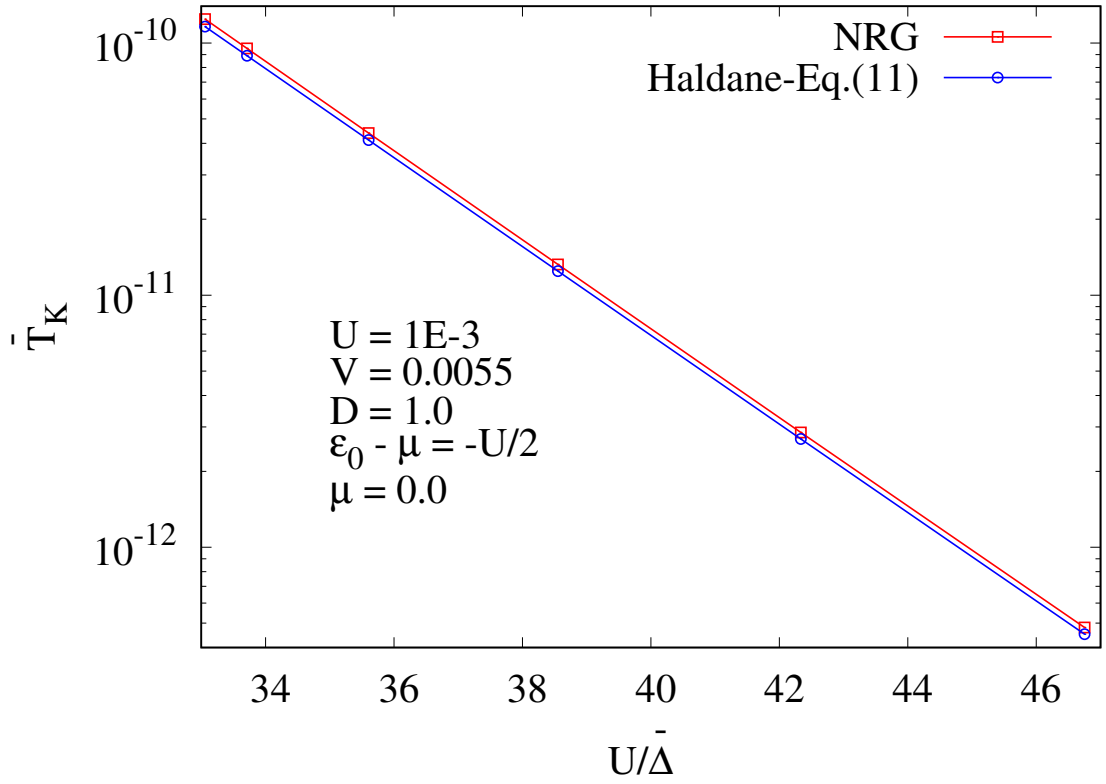

Figure 7.1: Log-linear plot of $\tilde{T}_K$ *vs* $U/\tilde{\Delta}$, deep into the Kondo regime. Comparison of NRG results [(red) squares curve] with the analytical results obtained from Eq. (7.4) [(blue) circles curve], for $U = 1.0 \times 10^{-3}$, $V = 5.5 \times 10^{-3}$, $0.0 \leq |\gamma| \leq 0.5$, $\gamma_{imp} = 0.0$, $\mu = 0.0$, and $\epsilon_0 - \mu = -U/2$. The very good agreement indicates that the renormalized Haldane expression [Eq. (7.4)] describes the dependence of the Kondo temperature with SOC to high accuracy.

7.1.2 Discussion of the NRG and analytical results for finite-SOC

In Figure 7.1, we show Kondo temperature results for finite-SOC, $\tilde{T}_K$ (in $\log_{10}$ scale), as a function of $U/\tilde{\Delta}$, for $U = 1.0 \times 10^{-3}$, $V = 5.5 \times 10^{-3}$, $0.0 \leq |\gamma| \leq 0.5$, $\gamma_{imp} = 0.0$, $\mu = 0.0$, at the particle-hole symmetric point $\epsilon_0 - \mu = -U/2$. The (red) squares curve was obtained using NRG, while the (blue) circles curve was obtained analytically through Eq. (7.4). We used this set of parameters for two reasons: first, the wide-band limit, i.e., $D \gg U, \tilde{\Delta}, |\epsilon_0|$, allows for a very precise determination of the prefactor to the exponential [see Eq. (7.4)]. Thus, in this regime, the Haldane expression is supposed to be the most accurate. This can be confirmed by its very good agreement with NRG, as shown in the figure. Second, for $U \gg \tilde{\Delta}$, and in the particle-hole symmetric point

$\epsilon_0 - \mu = {}^{-U}/_2$ and $\mu = 0$, one is deep into the Kondo regime, therefore, NRG is probing the properties of the SIAM very close to its strong coupling fixed point. The very good agreement shown by the results in Figure 7.1 imply that the SOC-induced reduction of the Kondo temperature is directly tied to the suppression of the hybridization $\tilde{\Delta}$ at the Fermi energy, which is caused by the widening of the band [see Figure 3.5], and this effect is *very accurately* described by the Haldane expression, Eq. (7.4), giving strong support to the analytical results presented in the previous section.

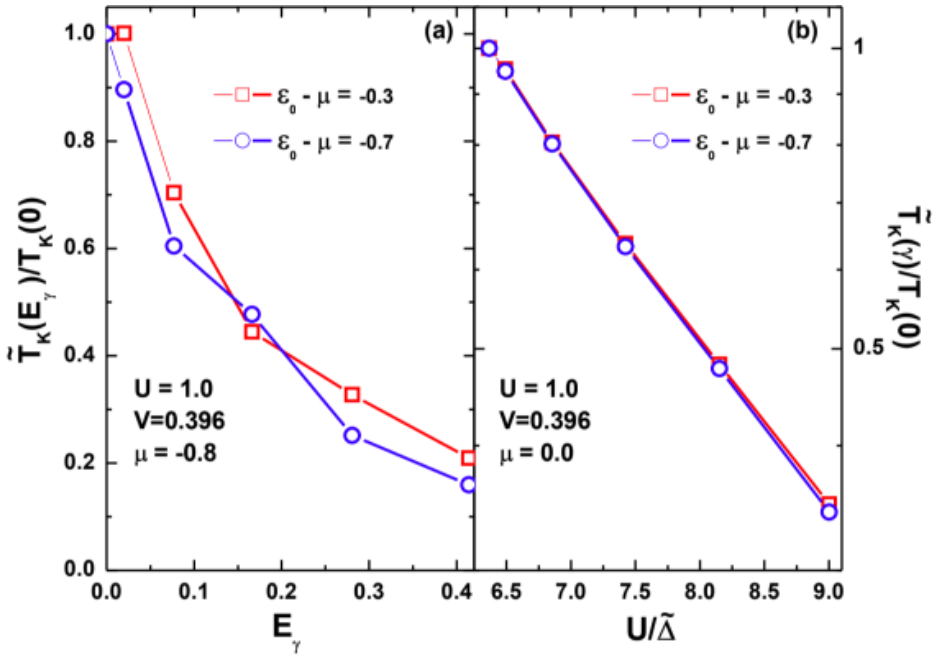

Figure 7.2: (a) NRG results for ${}^{\tilde{T}_K(E_\gamma)}/_{T_K(0)}$ *vs* E_γ (SOC energy, see main text) in the intermediate regime, for $U = 1.0$, $V = 0.396$, $0.0 \leq |\gamma| \leq 0.5$, $\gamma_{imp} = 0.0$, $\mu = -0.8$ (thus, the Fermi energy is 0.2 above the bottom of the band), and two different values of $\epsilon_0 - \mu$: -0.3 [(red) squares curve] and -0.7 [(blue) circles curve]. (b) Same parameters as in (a), except for the chemical potential, now at half-filling ($\mu = 0.0$). In addition, the horizontal axis is now ${}^{U}/_{\tilde{\Delta}}$, instead of E_γ, and the vertical axis is in $\log_{10}$ scale, showing that the Kondo temperature has an almost exponential behavior dependence on ${}^{U}/_{\tilde{\Delta}}$, similar to the results for the wide-band limit, Figure 7.1.

The situation is more involved for the second regime we analyzed, which we call intermediate regime, i.e., $U = D > \Delta$, where, in addition, we have moved the Fermi energy close to the bottom of the band. Recent results [62], for a model very similar to ours, obtained using QMC, have reported a polynomial dependence of the Kondo temperature with SOC for this intermediate regime (see Figure 3(a) in Ref. [62]). Their conclusion is similar to the one we obtained for the wide-band regime, namely, that the reduction of the hybridization at the Fermi energy, caused by SOC, is responsible for the

decrease in the Kondo temperature. In Figure 7.2(a), to compare our NRG results with the QMC ones in Ref. [62], it is shown ${}^{\tilde{T}_K(E_\gamma)}/_{T_K(0)}$ *vs* E_γ [where $E_\gamma = 2[\sqrt{t^2+|\gamma|^2}-t]$ is the so-called SOC energy, indicated in Figure 3.3(b)], for $U = 1.0$, $V = 0.396$, $0.0 \leq |\gamma| \leq 0.5$, $\gamma_{imp} = 0.0$, $\mu = -0.8$, and two different values of $\epsilon_0 - \mu = -0.3$ [(red) squares curve] and -0.7 [(blue) circles curve]. For this value of chemical potential, the Fermi energy is just 0.2 above the bottom of the band. The contrast to the results shown in Figure 7.1 is striking. Note that we have plotted (not shown) the two curves in panel (a) in $\log_{10}$ scale for the vertical axis (*vs* ${}^{U}/_{\tilde{\Delta}}$) and the behavior is clearly not Haldane-like. In Figure 7.2(b), we show NRG results for ${}^{\tilde{T}_K(\gamma)}/_{T_K(0)}$ *vs* ${}^{U}/_{\tilde{\Delta}}$ for the same parameters as in Figure 7.2(a), but for $\mu = 0.0$ (i.e., at half-filling), using a $\log_{10}$ scale. It is very clear that, *for the particle-hole symmetric point*, contrary to what happens when the Fermi energy is close to the bottom of the band [Figure 7.2(a)], ${}^{\tilde{T}_K(\gamma)}/_{T_K(0)}$, plotted against ${}^{U}/_{\tilde{\Delta}}$, shows a very-close-to exponential behavior. We do not plot results for the Haldane expression [Eq. (7.4)] because, as already mentioned above, that expression compares well with the NRG results just for the wide-band limit [67]. Nonetheless, the contrast between the results at half-filling [$\mu = 0.0$, panel (b)] and those for the Fermi energy close to the bottom of the band [$\mu = -0.8$, panel (a)], indicates that the polynomial behavior reported in Ref. [62] is caused by the proximity of the Fermi energy, and thus the Kondo peak, to the singularity at the bottom of the band. Indeed, as γ changes, the singularity moves [see Figure 3.5], altering its effect over the impurity's local density of states (LDOS), thus over its Kondo peak, and, by extension, over its Kondo temperature. A similar effect was observed for a related 2D model [56]. Indeed, as shown in detail in Ref. [56] [see its Figure (2)], for $U = D$ and with the Fermi energy sitting close to the bottom of the band, as it is the case for the intermediate regime analyzed here and in Ref. [62], the broad $\epsilon_0 - \mu$ peak in the impurity's LDOS is strongly affected by the singularity at the bottom of the band, and this has an effect on the width of the Kondo peak, thus in the associated Kondo temperature, resulting in the behavior seen in Fig 7.2(a). None of that is seen in Figure 7.1 and very little of it in Figure 7.2(b), because both the Kondo and the $\epsilon_0 - \mu$ peaks are far from the singularity and are not affected by its movement (more so in the case of the results in Figure 7.1, where, in addition, $U \ll D$). It is not noticeable in Figure 7.2(b), but the first two points ($|\gamma| = 0$ and 0.1), for both values of ϵ_0, slightly deviate from the exponential behavior followed by the rest of the points (at higher $|\gamma|$ values). This is consistent with our interpretation of the non-exponential behavior present for $\mu = -0.8$ being caused by the proximity of the bottom of the band

singularity to the Kondo peak, as the singularity moves away from it as SOC increases. Thus, in summary, the QMC results in Ref. [62], reporting a polynomial behavior of the Kondo temperature with SOC, in qualitative agreement with our results obtained through NRG [see Figure 7.2(a)], do not contradict our main conclusion regarding the suitability of using Haldane's expression [Eq. (7.4)] to understand the SOC effect on the Kondo regime. The reason is clear: the influence of any structures in the hybridization function (like the singularity at its bottom), which only manifests itself in the very specific regime analyzed in Figure 7.2(a), where the Fermi energy is close to the bottom of the band and $U = D$, is irrelevant in the wide-band (or flat-band) regime, $\mu = 0.0$ and $D \gg U, \Delta, |\epsilon_0|$, for which Eq. (7.4) was derived. Finally, we agree with Chen and Han [62] in their assessment that the poor man's scaling results [61], pointing to an exponential increase of T_K with SOC in a 1D system similar to ours, is a high temperature effect, which does not describe the properties of the Kondo ground state under the influence of SOC, at least in regards to the Kondo temperature. The NRG approach was performed using Wilson's discretization parameter set to $\Lambda = 2.0$, 2000 many-body states were kept after each NRG iteration (except for the calculations near the bottom of the band, where it was necessary to keep 20000), and we made use of the z-trick averaging in the discretization procedure. In addition, the Kondo temperature was obtained through Wilson's criterion [67]. We have used the NRG Ljubljana open-source code [109] for all NRG calculations.

7.2 Atomic approach: Thermoelectric transport properties of quantum dots

7.2.1 Density of states

In this section, we present preliminary results for the thermoelectric properties taking into account the SOC of the conduction band over the Kondo resonance. The results obtained here lead us to solve the problem employing the NRG approach.

In the calculations, we employed the energy unit $\Gamma_o = 0.001t$, where t is the tight-binding hopping parameter, and $D = 2t$ is the half-width of the conduction band in the absence of SO coupling; the chemical potential is always located at $\mu = 0$. We considered the following values of the correlation: $U = 20.0\Gamma_o$, $U = 50.0\Gamma_o$ and

$U = 80.0\Gamma_o$ corresponding to the symmetric limit of the Anderson model, where $E_{QD} = -U/2$. The hybridization is calculated from the Anderson parameter $\Gamma = \pi V^2 \rho_c(\mu = 0)$. We show results corresponding to the universality of the electrical and thermal conductance as well as the thermopower [8], in the presence of the conduction band spin-orbit coupling, which varies from $\gamma = 0.0t$ to $\gamma = 4.0t$.

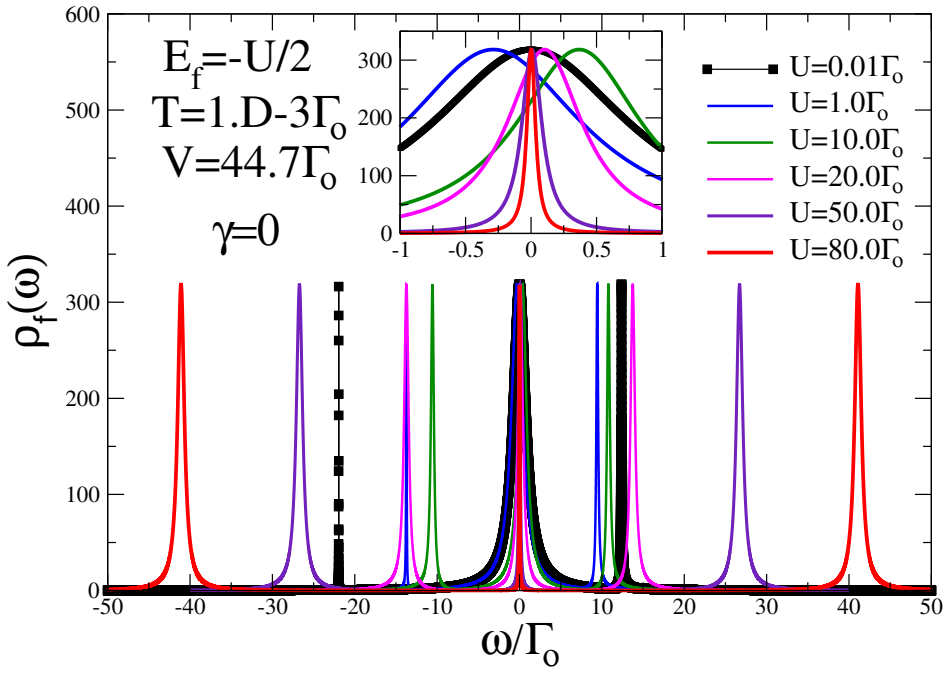

Figure 7.3: The localized density of states for different values of the electronic correlation U. Formation of the Kondo peak, starting from the $U \simeq 0$ limit to the Kondo limit, $U = 80.0\Gamma_o$.

In Figure 7.3 we show the localized density of states $\rho_f(\omega)$, corresponding to the symmetric limit of the SIAM, for different values of the electronic correlation U and spin-orbit coupling $\gamma = 0$. The figure shows the effect of the formation of the Kondo peak as the correlation U is varied from the $U \simeq 0$ limit to the Kondo limit, $U = 80.0\Gamma_o$. For $U = 0.01\Gamma_o$, as indicated in the black curve, we have a broad peak centered at around $E_f = -0.005\Gamma_o$ and two asymmetric satellites peaks; the particle-hole symmetry does not exist. However, as we increase the correlation to $U = 10.0\Gamma_o$ (dark green curve), the particle-hole symmetry is established, but the Kondo peak is only completely formed for $U = 50.0\Gamma_o$ (indigo curve), as indicated in the inset of the figure.

In the inset, the process of the formation of the Kondo peak, as the electronic correlation increases, is shown more clearly: For $U = 0.01\Gamma_o$, there is an uncorrelated peak centered at around $\mu = 0$, as the U increases to $U = 1.0\Gamma_o$, the broad peak

is displaced to the left, and after to the right at $U = 10.0\Gamma_o$, finally the peak goes to the chemical potential at $\mu = 0$ for $U = 50.0\Gamma_o$, where now, the Kondo peak is completely formed. During this process the width of the peak diminishes, indicating that the Kondo temperature is varying from $T_K = 0.34\Gamma_o$ ($U = 20.0\Gamma_o$); $T_K = 0.092\Gamma_o$ ($U = 50.0\Gamma_o$) and $T_K = 0.039\Gamma_o$ ($U = 80.0\Gamma_o$).

t is important to emphasize that the atomic method calculations that we have done here obey Friedel's sum rule. Therefore, the results that we obtain here show us the trend of the exact results that we will look for with the NRG method.

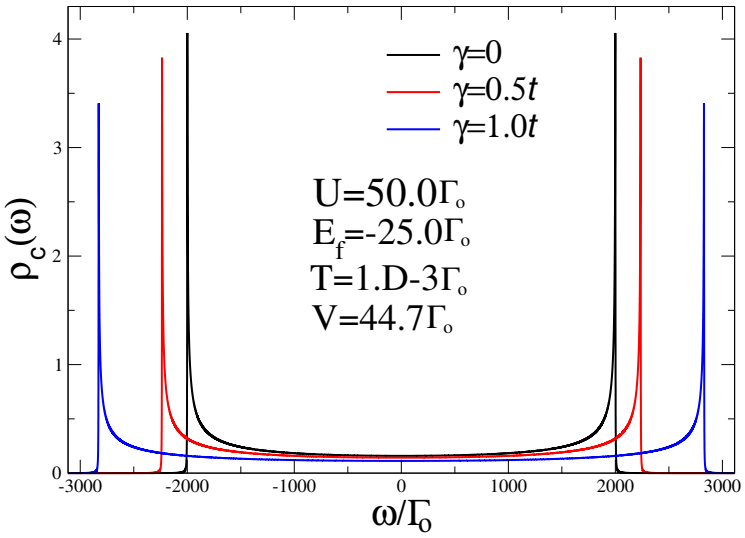

Figure 7.4: Conduction density of states for different values of the spin-orbit coupling.

In Figure 7.4, we show the conduction density of states $\rho_c(\omega)$, corresponding to the symmetric limit of the SIAM. We consider the electronic correlation $U = 50\Gamma_o$, and different values of spin-orbit coupling γ, whose main effect is to enlarge the density of states, decreasing its value at the chemical potential μ.

In Figure 7.5 we plot the localized density of states $\rho_f(\omega)$, for different values of the spin-orbit coupling γ and the electronic correlation $U = 50.0\Gamma_o$. The main result of the SO interaction is to increases the height of the Kondo peak, which leads to a decreases of the Kondo temperature, which is given by: $T_K = 0.5288\Gamma_o(\gamma = 0.0)$, $T_K = 0.3149\Gamma_o(\gamma = 1.0t)$, $T_K = 0.1385\Gamma_o(\gamma = 2.0t)$, $T_K = 0.06095\Gamma_o(\gamma = 3.0t)$, and $T_K = 0.03089\Gamma_o(\gamma = 4.0t)$. So, we see that the main effect of SOC is to improve the

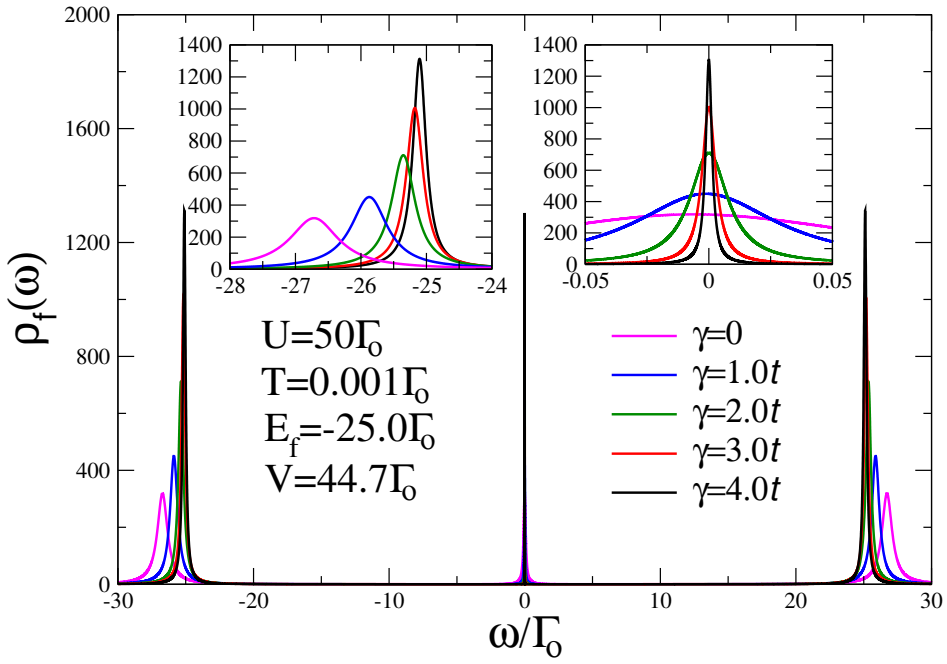

Figure 7.5: The localized density of states $\rho_f(\omega)$, for different values of the spin-orbit coupling γ.

Kondo regime, because the Kondo resonance peak becomes finer with SOC, this is like as to tune the system into the Kondo regime.

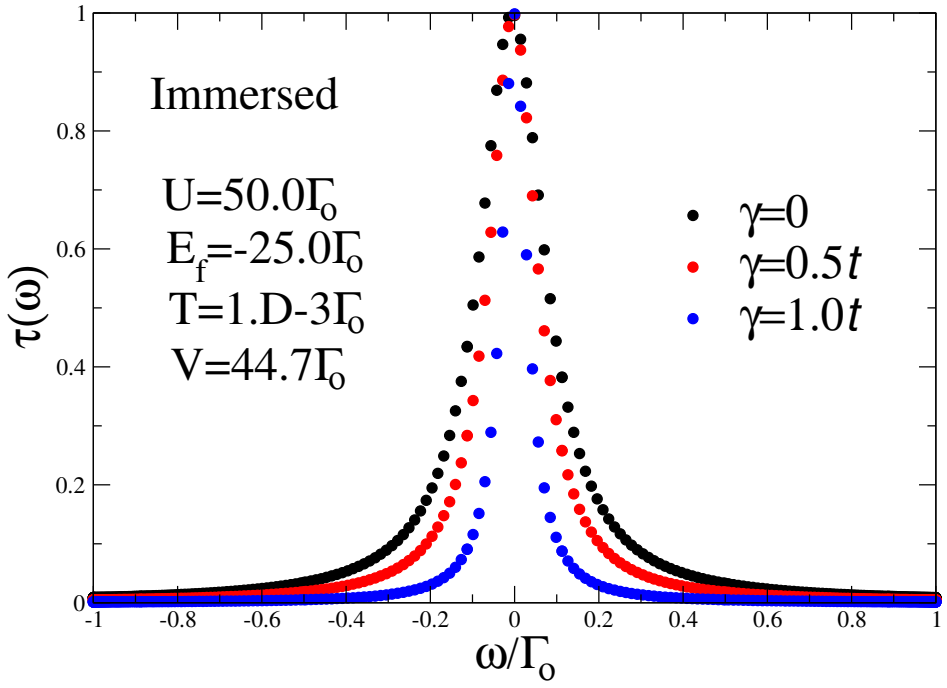

Figure 7.6: The transmittance $\tau(\omega)$, for different values of the spin-orbit coupling, γ in the case of the immersed quantum dot.

In Figure 7.6, we plot the transmittance $\tau(\omega)$, for the case of the immersed quantum dot, considering different values of the spin-orbit coupling γ. To get reliable results to the thermoelectric properties, we must guarantee that the transmittance, for different spin-orbit strengths, goes to the right unit value at low temperatures.

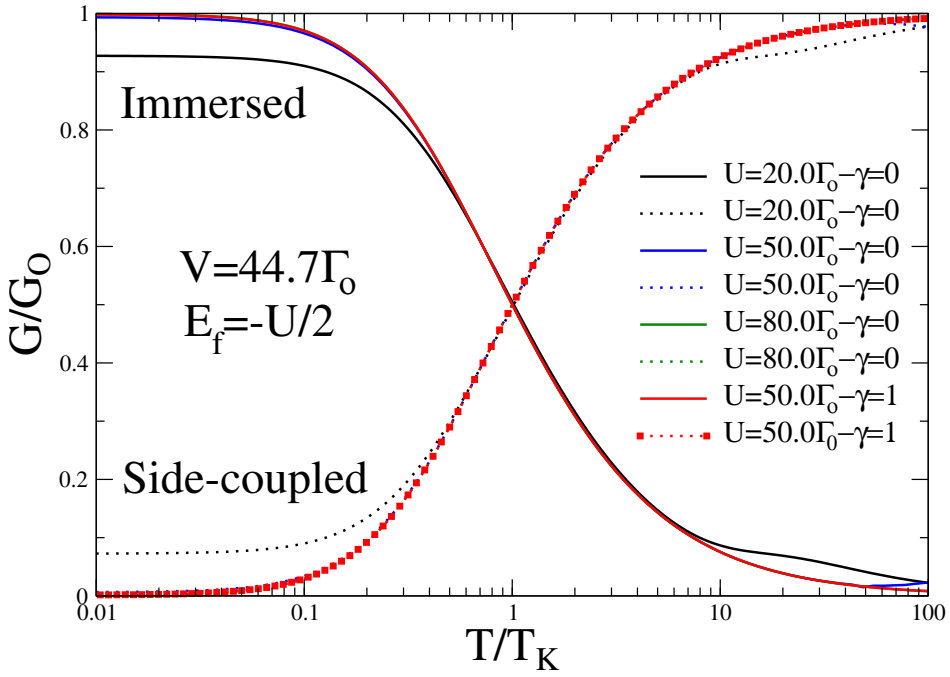

Figure 7.7: The universality of the conductance for the cases of the dot immersed and side coupled to the leads.

In Figure 7.7, we plot the universality of the electrical conductance, in the particle-hole symmetric case, for the dot immersed and side coupled to the leads. In the Kondo regime, the conductance presents a universal character; it is invariant under the variation of the electronic correlation and the spin-orbit coupling. We consider the spin-orbit coupling $\gamma = 0$ and different values of the electronic correlation U. Figure 7.3 shows that, for $U = 20.0\Gamma_o$, the Kondo peak is not yet formed, and as a consequence the electrical conductance here is located apart from the other universal curves. On the other hand, for $U = 50.0\Gamma_o$, $U = 80.0\Gamma_o$ and for $(U = 50.0\Gamma_o - \gamma = 1.0t)$, the system is in the Kondo regime, the Kondo peak is present in the density of localized states, and the electrical conductance exhibits universal behavior.

The important point that should be stressed here is that the thermoelectric properties do not depend on the absolute value of the Kondo temperature, but only depends on the T/T_K relation [8]. As indicated in the figure, although the atomic approach does not produce the correct absolute Kondo temperature, as given by the Haldane's rela-

tion, the method produces a correct ratio T/T_K and its results satisfy the universality requirements.

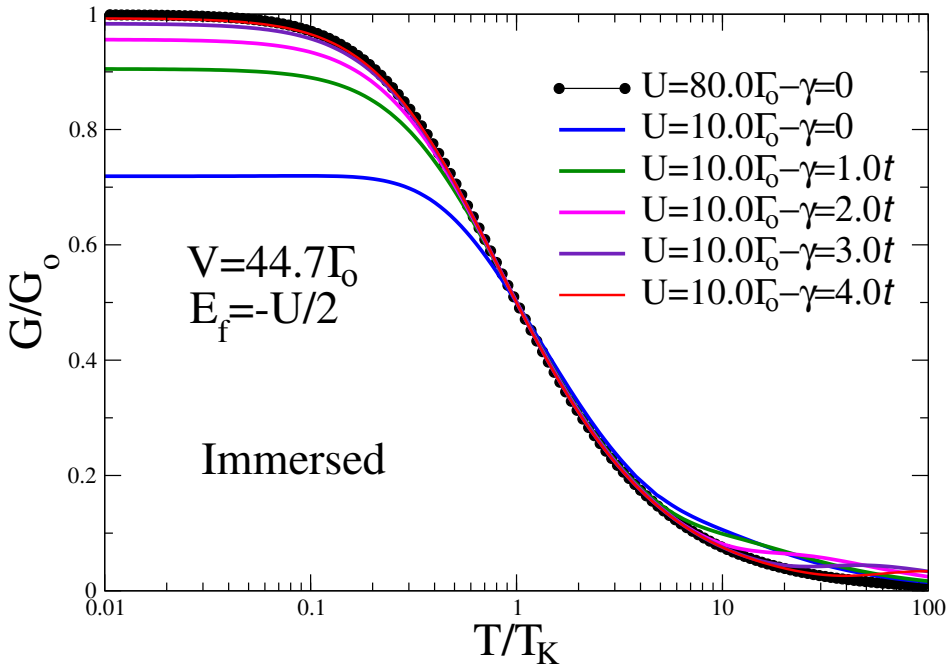

Figure 7.8: Electrical conductance tuned to the Kondo limit by the increase of the spin-orbit coupling, for the cases of the dot side-coupled and immerse.

In Figure 7.8 we vary the spin-orbit coupling in the interval $\gamma = [1-4]t$ to tune an electrical conductance far from the Kondo regime the electronic correlation, with $(U = 10.0\Gamma_o - \gamma = 0)$, to the extreme Kondo limit with $(U = 80.0\Gamma_o - \gamma = 0)$. Those huge SOC do not appear in real compounds, and we employed them here only to stress the situation and reveal the potentiality of the effect. However, we believe that it is possible to realize the simulation of Figure 7.8, with the SOC in the interval $\gamma = [0-0.5]t$ in real quantum dots or optical lattices systems.

In Figure 7.9 we plot the universality of the thermal conductance, in the particle-hole symmetric case, for the case of the dot immersed and side coupled to the leads. As happens with the electrical conductance, discussed in Figure 7.7, the thermal conductance, in the Kondo regime, is also invariant under the variation of the electronic correlation [8], and the SOC. Here, we consider the SOC $\gamma = 0$ and different values of the electronic correlation U. For $U = 20.0t$, the Kondo peak is not formed, and this is reflected in the absence of universal behavior. On the other hand, for $U = 50.0\Gamma_o$, $U = 80.0\Gamma_o$ and for $(U = 50.0\Gamma_o - \gamma = 1.0t)$, the system is lead to the Kondo limit by increasing the SOC, the Kondo peak is present in the density of localized states, and

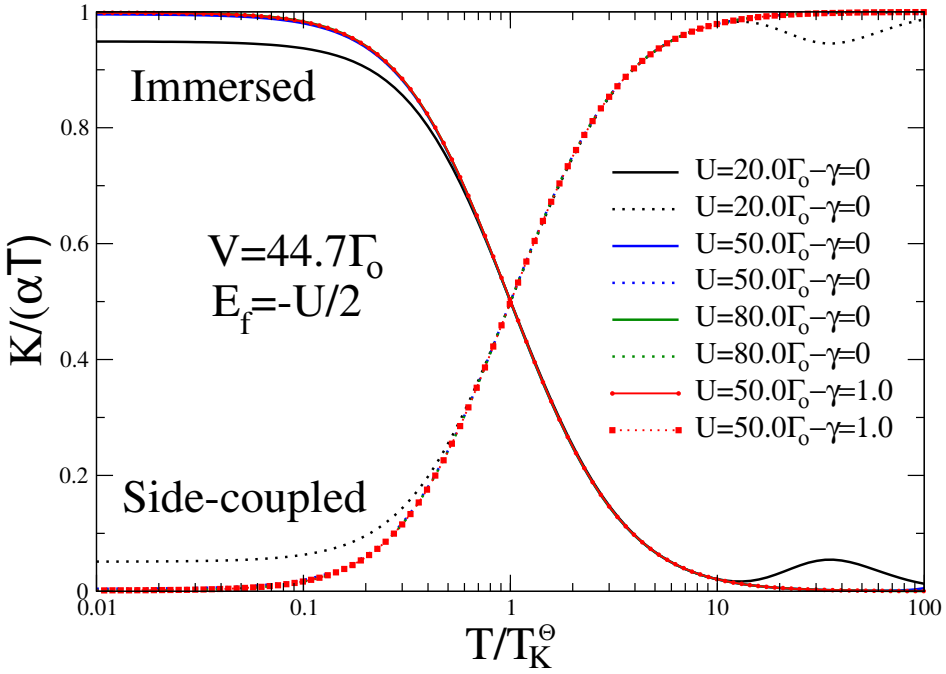

Figure 7.9: The universality of the thermal conductance for the cases of the dot side coupled to the leads. The thermal conductance is invariant under the variation of the electronic correlation in the Kondo regime.

the thermal conductance exhibits universal behavior.

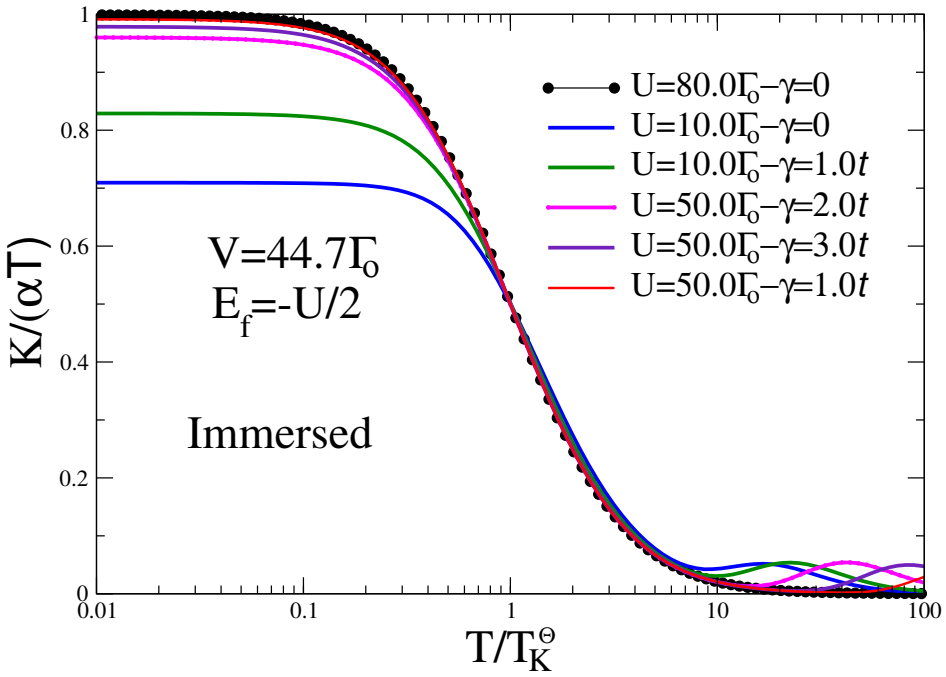

Figure 7.10: The thermal conductance tuned to the Kondo limit by the increase of the spin-orbit coupling, for the cases of the dot side-coupled and immerse.

In Figure 7.10 we vary the SOC in the interval $\gamma = [1-4]t$ to tune the thermal

conductance far from the Kondo regime, with the electronic correlation ($U = 10.0\Gamma_o - \gamma = 0$), to the extreme Kondo limit with ($U = 80.0\Gamma_o - \gamma = 0$). The electrical and thermal conductances are closely related between each other, and as shown in Figure 7.7, this could indicate that those conduction processes can be considered as different aspects of the same physical phenomena.

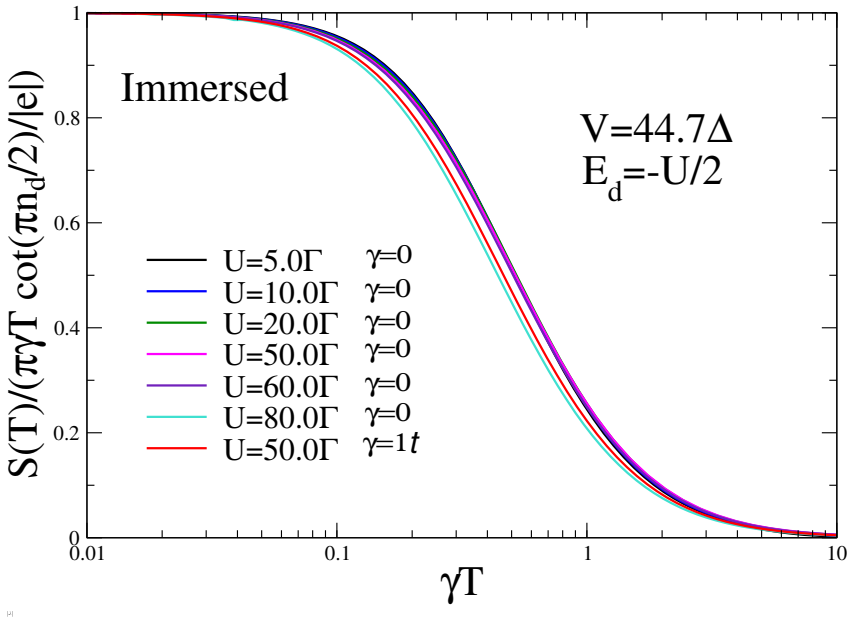

Figure 7.11: The universality of the thermopower for the case of the dot immersed to the leads.

In Figure 7.11, we plot the thermopower for the case of the dot immersed in the leads. The thermal conductance exhibits universality, being invariant under the variation of the electronic correlation in the Kondo regime [8].

As in the case of the electrical and thermal conductances discussed in Figs. 7.7 and 7.9, we consider the spin-orbit coupling $\gamma = 0$ and different values of the electronic correlation U. But here, we start with a low electronic correlation $U = 5.0\Gamma_o$ and increase it until $U = 60.0\Gamma_o$. For all of these U values, the thermopower exhibits universal behavior, which contrasts with the earlier results of the electrical and thermal conductances, where the universality is manifested only for the QD into the Kondo regime. However, when we increase the electronic correlation to $U = 80.0\Gamma_o$, the thermopower separates from the bunch of the universal, at around the Kondo limit. We also consider the SO interaction $\gamma = 1.0t$ over the $U = 50.0\Gamma_o$ curve, and it goes

close to the Kondo limit curve.

7.3 NRG results: Thermoelectric transport properties of quantum dots

All the results in this section onwards are results of the article sent to PRB, where the preprint version is available at [114].

7.3.1 Spin-orbit effects over the density of states

In Kondo physics, the hybridization function at the Fermi energy is an important quantity. When SOC is included in the conduction band, we obtain that the hybridization function at the Fermi energy is given by

$$\Gamma_\gamma = \pi\Lambda^2\rho_c\left(0\right) = \frac{V^2}{2\sqrt{t^2+|\gamma|^2}}. \tag{7.6}$$

In all the calculations that follow, we employed $\Gamma_0 = 0.007$ [115], in units of D_0, which is the half-width of the conduction band in the absence of SOC [116] (i.e., for $\gamma = 0$), and the chemical potential is always located at $\mu = 0$. In addition, we will vary SOC in the interval $0.0 \leq |\gamma| \leq 0.5$, which will make Γ_γ vary in accordance with Eq. (7.6). Finally, for the calculation of the thermoelectric (TE) properties, following standard procedure, we take the electron charge as $e = 1$ and Planck's constant as $h = 1$. Thus, the results in Figure 7.18(b) (for K_e), and Figs. 7.20 and 7.25(b) (for S), are presented in arbitrary units, while all other figures, studying the universality of the TE properties, are presented in dimensionless units.

In Figure 7.12, we show the QD's LDOS $\rho_d(\omega)$ at the particle-hole symmetric (PHS) point ($\epsilon_d = -U/2$) of the SIAM for several different values of the Coulomb repulsion $\Gamma_0 \leq U \leq 20.0\Gamma_0$, for vanishing SOC, $|\gamma| = 0.0$. For this range of variation of U/Γ_0, it is well know that the system passes from weak correlated system (for the smaller values of U/Γ_0) to the strongly correlated system (Kondo state, for the larger values of U/Γ_0). The passage from the former to the latter is a crossover, thus it does not occur for an specific value of U/Γ_0. Nonetheless, the results show the gradual formation of the Kondo peak as

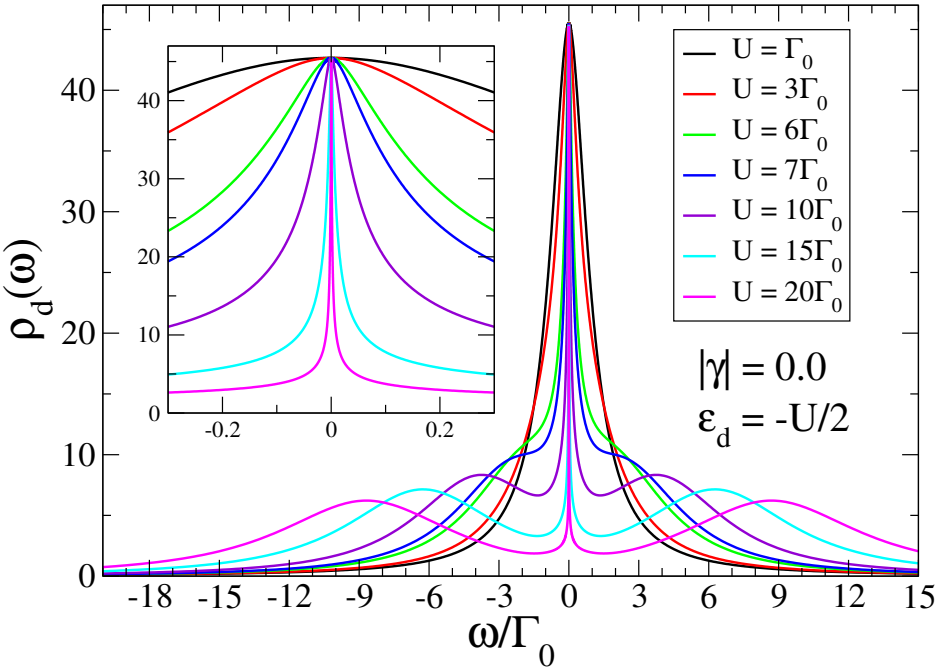

Figure 7.12: QD's LDOS $\rho_d(\omega)$ for different values of the electronic correlation U and $|\gamma| = 0.0$, showing the formation of the Kondo peak, starting from $U = \Gamma_0$, when the system is weakly correlated, to $U = 20.0\Gamma_0$, when the system is deep inside the Kondo regime when the system is strongly correlated. Inset: Details of the formation of the Kondo peak. Note that all curves are at the PHS point $\epsilon_d = {}^{-U}/_{2}$. Comparing with the result shown in Figure 7.3 with the atomic method, this is the exact version.

the correlation U is varied from $U = \Gamma_0$ to $U = 20.0\Gamma_0$, where the system is already deep into the Kondo regime [very low Kondo temperature $T_{K\gamma}$—see Eq. (7.4)]. For $U = \Gamma_0$, we have a broad peak centered around the chemical potential, located in $\omega = 0$ (black curve); in addition, the two symmetric Hubbard satellite peaks characteristic of the PHS point cannot be discerned. However, as we increase the correlation to $U = 10.0\Gamma_0$ (purple curve), the Hubbard satellites are already well established, but the Kondo peak is only completely formed above $U = 15.0\Gamma_0$ (cyan curve). In the inset, the formation of the Kondo peak, as the electronic correlation increases, is shown more clearly. Along this process, the peak diminishes its width, indicating the establishment of the Kondo regime characterized by a Kondo temperature $T_{K\gamma}$, which is proportional to the width of the Kondo peak, thus, the narrower the peak, the lower is the Kondo temperature and the deeper is the system into the Kondo regime.

In Figure 7.13, we show the DOS of the conducting leads $\rho_c(\omega)$, corresponding to different values of SOC, $0.0 \leq |\gamma| \leq 0.5$. The main effect of the SOC is to produce a

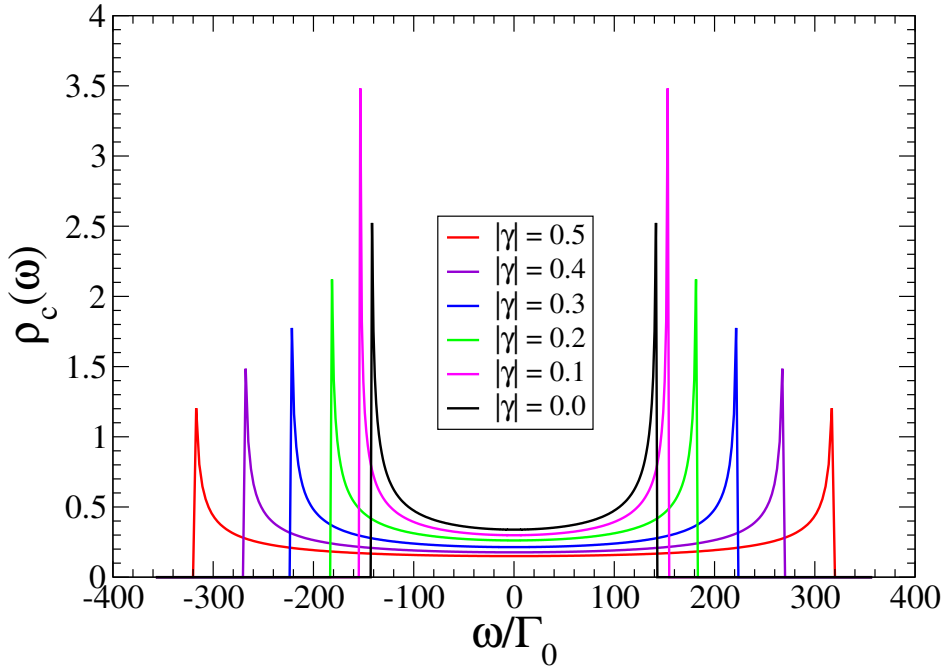

Figure 7.13: Density of states of the 1D conducting leads $\rho_c(\omega)$ for different values of SOC, $0.0 \leq |\gamma| \leq 0.5$. Notice the sizable broadening of the band, as well as the decrease of the DOS at the Fermi energy. This figure as well as the previous one, was also shown by the atomic method Figure 7.4.

broadening of the band, and, as a consequence, a decrease of the DOS at the chemical potential $\mu = 0$, which, see Eq. (7.3), results in the decrease of the value of the SOC-renormalized hybridization function at the Fermi energy.

In Figure 7.14, we plot the QD's LDOS $\rho_d(\omega)$, for different values of $|\gamma|$, for a PHS situation. We do all the calculations for $U = 6.0\Gamma_0$, thus, at $|\gamma| = 0.0$, not deep into the Kondo regime (see green curve in Figure 7.12). However, by the evolution of $\rho_d(\omega)$, due to the increase of SOC from $|\gamma| = 0$ to $|\gamma| = 0.5$, it can be clearly seen that the increase of SOC drives the system deep into the Kondo regime. Indeed, the height of the Kondo peak increases while its width decreases, indicating a lowering of the Kondo temperature. This striking effect is directly related to the decreasing value of the SOC-renormalized hybridization function at the Fermi level, since, according to Friedel's sum rule, this should cause an increase of $\rho_d(\mu = 0)$ and, according to Eq. (7.4), a decrease of the Kondo temperature, with an accompanying reduction of the Kondo-peak half-width. It is also possible to discern a slight increase in the separation between the satellite Hubbard peaks, pointing to an increase of the effective Hubbard on-site repulsion, which accounts for an increase in the electronic correlations. It should also

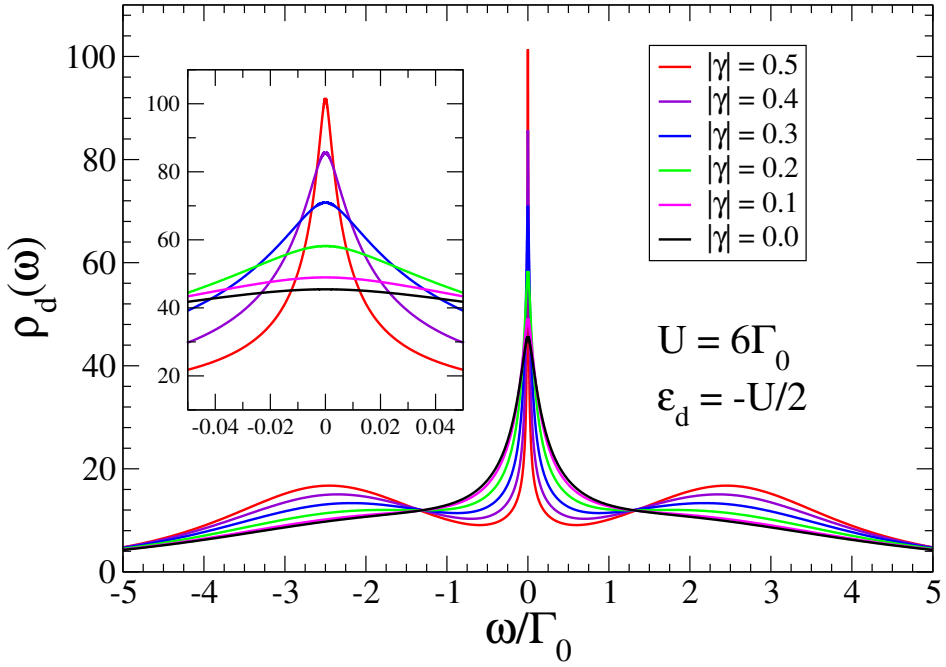

Figure 7.14: QD's LDOS $\rho_d(\omega)$, for different SOC values, $0.0 \leq |\gamma| \leq 0.5$, at the PHS point, for $U = 6.0\Gamma_0$. Note that the black curve ($|\gamma| = 0.0$) corresponds to the green curve in Figure 7.12, thus inside the moderately correlated regime, clearly showing that SOC drives the system deep into a strongly correlated (deep into the Kondo state). Notice the very well formed Kondo peak for $|\gamma| = 0.5$ (red curve). Inset: zoom close to $\omega = 0$, showing details of the evolution of the Kondo peak.

be noted that the results in Figure 7.14 agree with Refs. [62, 63].

7.3.2 Thermoelectric properties maps

In this section, we plot the TE properties for different values of ϵ_d, from the Kondo to the empty-orbital regime, as a function of T/Γ_0, for different values of SOC, $|\gamma| = 0.0$, 0.25, and 0.5. For all the results in this section, we consider the electronic correlation $U = 7.0\Gamma_0$, and, to characterize the different regimes of the system (at low temperature), we follow the definitions in Ref. [8], viz., (i) n_d values in the interval $|n_d - 1|_{T\approx 0} \leq 0.25$ (red curves) correspond to the Kondo regime, (ii) $|n_d - 0.5|_{T\approx 0} \leq 0.25$ (blue curves) correspond to the mixed-valence regime, (iii) $|n_d|_{T\approx 0} \leq 0.25$ (green curves) correspond to the empty-orbital regime. The borders between different regimes occur as crossovers. Although these regime definitions are more appropriate to the low temperature region, we extend them to the higher temperature regions as well.

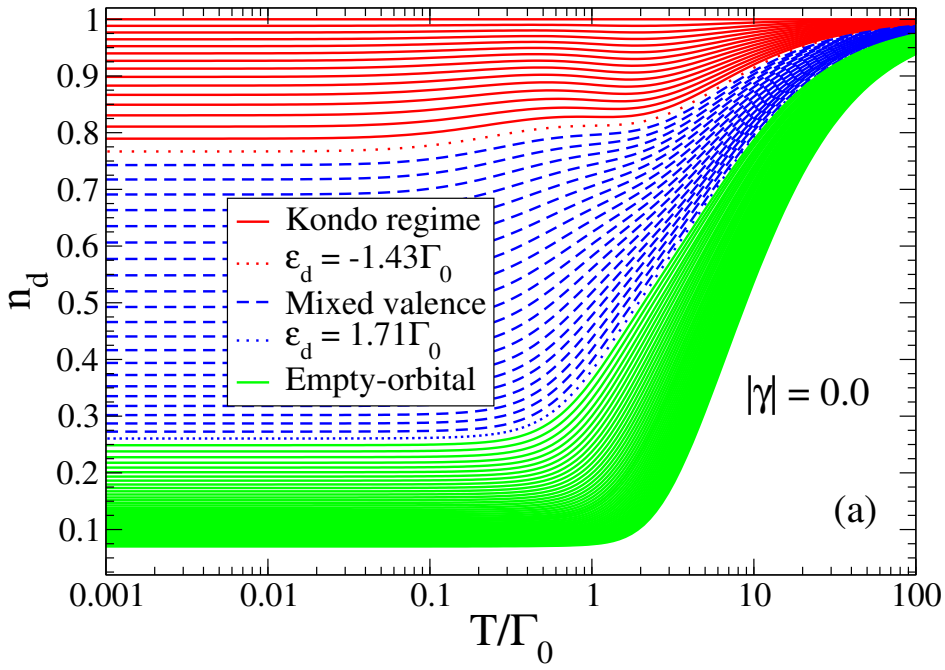

Figure 7.15: QD occupation-number map, for $|\gamma| = 0.0$, indicate the temperature variation of n_d for varying ϵ_d in the interval $-U/2 \leq \epsilon_d \leq 8.71\Gamma_0$. The definition of the different regimes follows Ref. [8], i.e., Kondo (red), $|n_d - 1|_{T\approx 0} \leq 0.25$, intermediate-valence (blue), $|n_d - 0.5|_{T\approx 0} \leq 0.25$, empty-orbital (green), $|n_d|_{T\approx 0} \leq 0.25$. The dotted curves, with corresponding ϵ_d values indicated in the legends, demarcate the crossover from one regime to the next. All results for $U = 7.0\Gamma_0$

In Figs. 7.15, 7.16, and 7.17 we plot the QD occupation number n_d as a function of temperature for different values of ϵ_d ($-U/2 \leq \epsilon_d \leq 8.71\Gamma_0$). These figures correspond to different SOC values $|\gamma| = 0.00, 0.025$ and 0.50, respectively. The ϵ_d values shown in the legend represent the values at which, according to the definitions above, there is a crossover between different regimes, indicated by dotted curves. By comparing different panels, it is clear that SOC affects the overall spread of each region. Indeed, as $|\gamma|$ increases from 0.0 to 0.5, the empty-orbital and Kondo regions expand, at the expense of the mixed-valence region. This makes sense, as the decrease of the hybridization between the QD and the conduction band, caused by SOC, should enhance spin fluctuations (enhancing Kondo and empty-orbital) at the expense of charge fluctuations (weakening intermediate valence). As we shall see next, this will be reflected in the results for the TE properties.

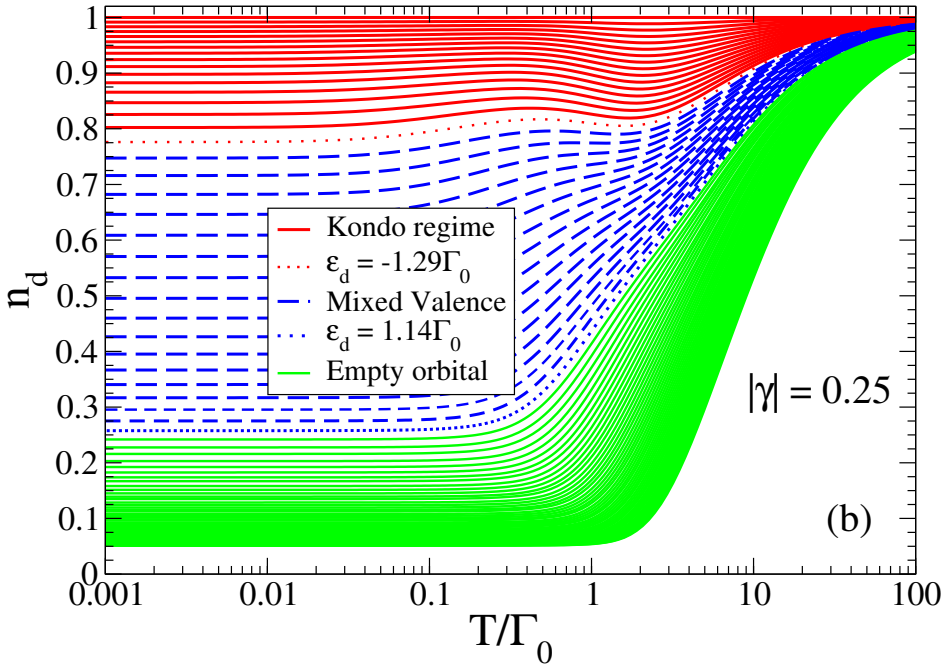

Figure 7.16: Same as in Figure 7.15, but now for $|\gamma| = 0.25$.

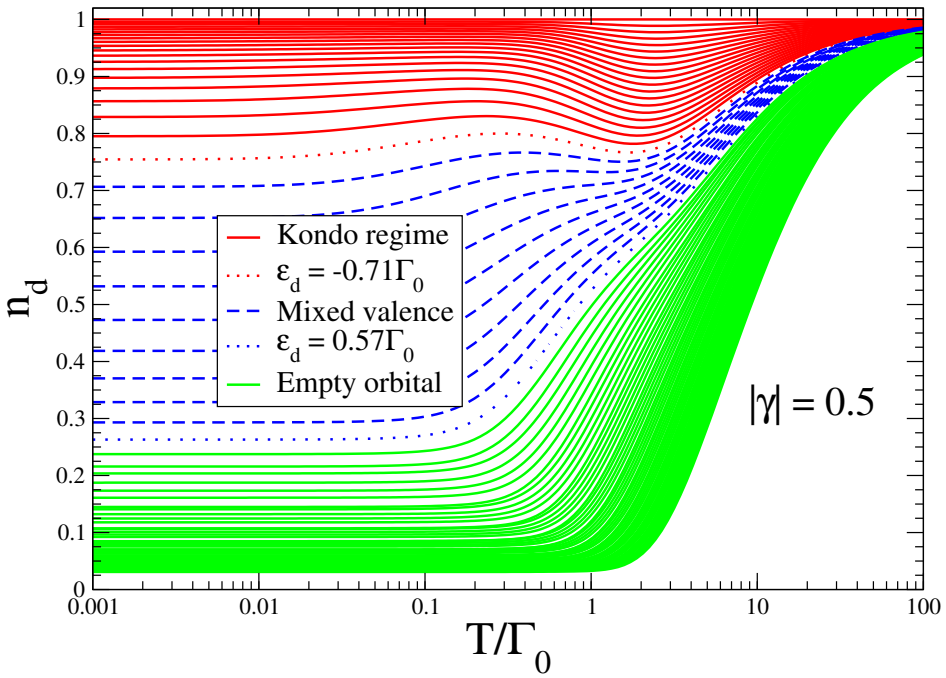

Figure 7.17: Same as in Figs. 7.15 and 7.16, but now for $|\gamma| = 0.5$.

Electrical and thermal conductances

In Figure 7.18, we have similar plots to the ones in Figs. 7.15, 7.16, and 7.17, but this time for the electrical conductance $^{G(T)}/_{G_0}$, in panels (a), (b), and (c), and for the

thermal conductance $K_e(T)$, in panels (d), (e), and (f). $G_0 = {}^{2e^2}/_h$ is the quantum of conductance (taking spin into account). The arrows indicate the direction of increasing values of ϵ_d, where the values of ϵ_d for each curve are the same as in Figs. 7.15, 7.16, and 7.17. Following Ref. [10], the Kondo temperature, $T_{K\gamma}$, can be calculated, from each curve in the three panels (a), (b), and (c), by computing the temperature value where the electrical conductance attains $G(T_{K\gamma}) = {}^{G_0}/_2 = {}^{e^2}/_h$. By using that criterion to define $T_{K\gamma}$, it is easy to see that the average $T_{K\gamma}$ of the red curves (Kondo regime, as defined by Costi *et al.* [8]) in panel (c) is more than an order of magnitude lower than the average $T_{K\gamma}$ in panel (a). Taking in account the universally accepted concept that, the lower is $T_{K\gamma}$, the deeper we are into the Kondo regime, leads us to assert that an increase in SOC drives the SIAM deeper into the Kondo regime, as already observed through the LDOS results in Figure 7.14.

In the right column of Figure 7.18, we have similar plots to the ones in the left column, but this time for the thermal conductance K_e, as a function of temperature (in units of Γ_0). The arrows have the same meaning as in the electrical conductance column. Comparing the three panels (d), (e) and (f), we observe again the SOC's tendency to reduce the intermediate valence region and to increase the Kondo and the empty-orbital regions. The three panels (d), (e), and (f), for $|\gamma| = 0.0$, 0.25, and 0.5, respectively, exhibit a crossing point, slightly below $T = \Gamma_0$ (and weakly dependent on γ). This crossing point appears as the convergence of all the red and blue curves to a very narrow window interval at $T \approx \Gamma_0$ [8]. It is interesting to note that the width of this window becomes increasingly narrower as γ increases, basically collapsing to a single point for $|\gamma| = 0.5$. These crossing points are characteristic signatures of strongly correlated systems, like it was observed for the specific heat in the Hubbard model in Ref. [117].

In Figure 7.19, we can see ${}^{G(\epsilon_d)}/_{G_0}$, as a function of ϵ_d (scaled by Γ_0), for different values of temperature ($5.7 \times 10^{-5} \leq T/\Gamma_0 \leq 1.14$). Panels (a) and (b) are for $|\gamma| =$ 0.25 and 0.5, respectively. It is easy to see that, in both panels, as the temperature increases above a certain value (the Kondo temperature for $\epsilon_d = {}^{-U}/_2$), there is an overall suppression of the conductance, which is more pronounced at the PHS point ($\epsilon_d = {}^{-U}/_2$). The regime located between the two peaks, symmetrically positioned around the PHS point, constitutes the so-called Coulomb blockade regime, where the QD (or impurity) is approximately single-occupied, and Coulomb repulsion suppresses the conductance. Since we are above T_K (its value *at* the PHS point), there is no

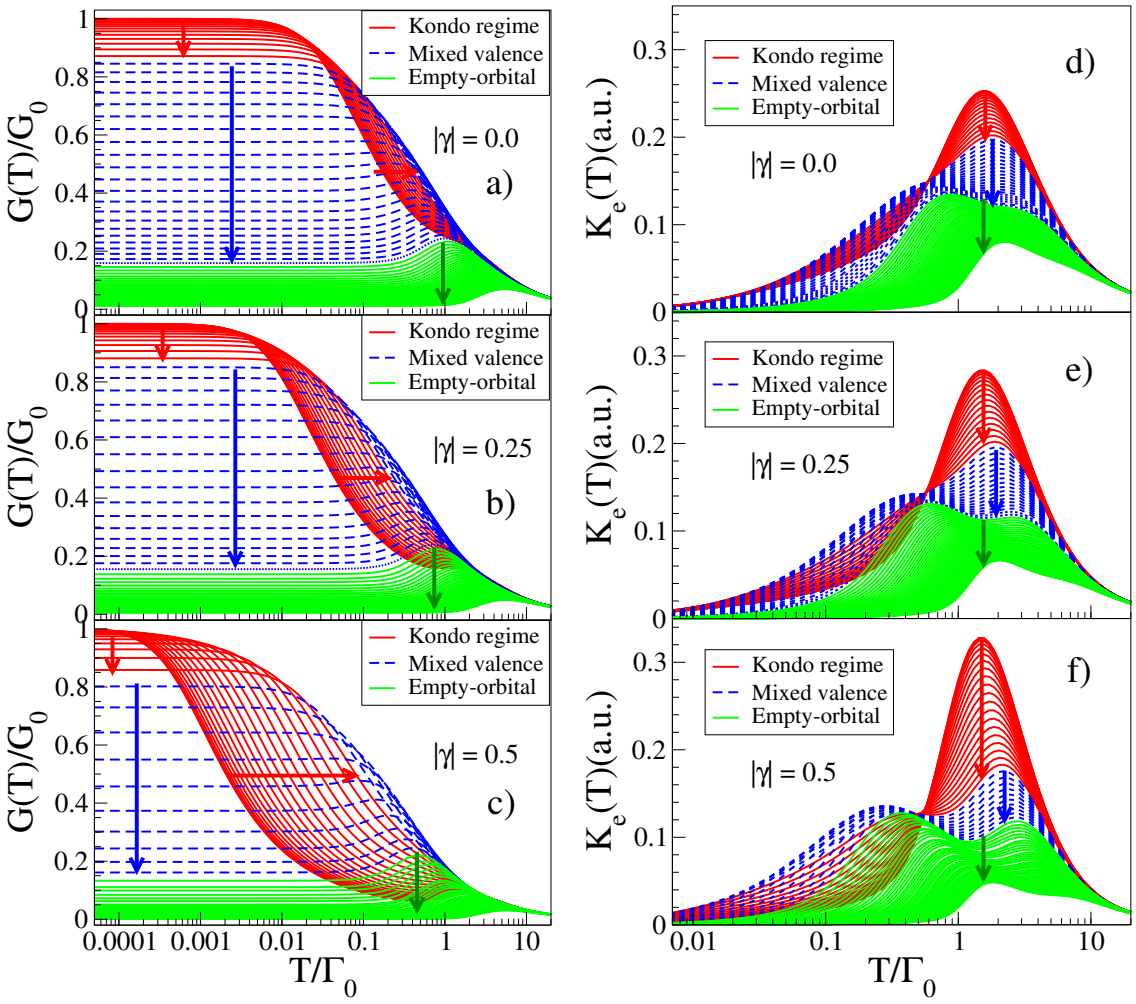

Figure 7.18: Same parameters as in Figure 7.15, 7.16, and 7.17, but now showing the electrical conductance $G(T)$ (in units of the quantum of conductance G_0) in the left column, and the thermal conductance $K_e(T)$ (in arbitrary units) in the right column; both conductances are plotted as a function of temperature. The arrows indicate the direction of increasing values of ϵ_d, where the values of ϵ_d for each curve are the same as in Figs. 7.15, 7.16, and 7.17. The temperature is in units of Γ_0 and $U = 7.0\Gamma_0$.

Kondo peak anymore at the Fermi energy and perfect conductance (around the PHS point) is lost. As already observed above through other properties, these results show that the Kondo temperature decreases with γ, since the conductance suppression in the right panel (higher $\gamma = 0.5$) starts at a lower temperature, $T \approx 0.00057\Gamma_0$, than in the left panel (lower $\gamma = 0.25$), $T \approx 0.0057\Gamma_0$.

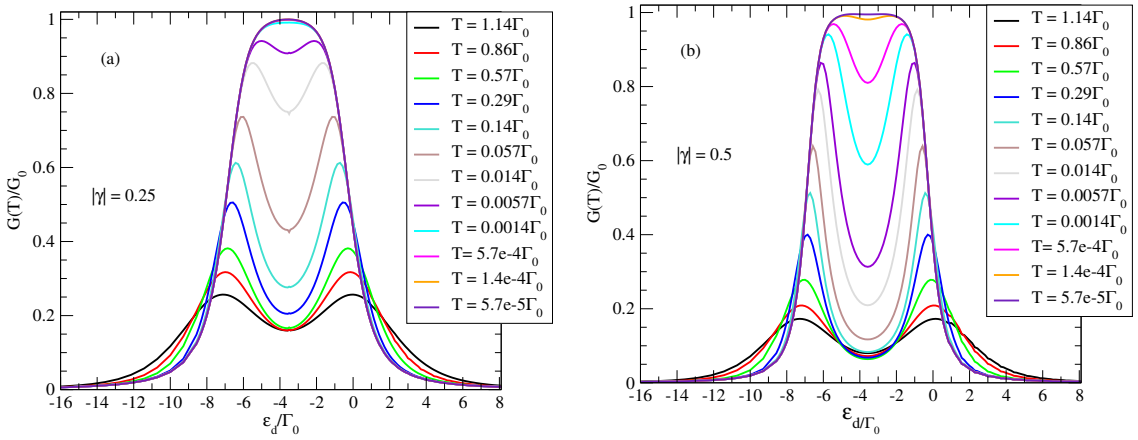

Figure 7.19: Electrical conductance $^{G(\epsilon_d)}/_{G_0}$ as a function of ϵ_d/Γ_0 for different temperatures (as indicated in the legend). Panel (a) is for $|\gamma| = 0.25$, and panel (b) for $|\gamma| = 0.5$. Both panels are for the same temperatures.

Thermopower $S(T)$

In panels (a), (b), and (c) in Figure 7.20, we show plots similar to the ones in Figs. 7.15 to 7.18, but this time for the thermopower $S(T)$, as a function of temperature. There are three peaks in the Kondo regime (red curves), viz., two minima satellite peaks located at left and right of a maximum central peak located at $T \approx \Gamma_0$, which is inside the interval $[T_1 : T_2]$. Temperatures T_1 and T_2 represent energy scales associated to the Kondo regime that characterize the changes in who are the $S(T)$ heat carriers, from electrons to holes to electrons, from left to right. In the PHS point, i.e., $\epsilon_d = {}^{-U}/_2$, $S(T) = 0$. However, away from the PHS point, $S(T)$ acquires a temperature dependence. Comparing the three panels, for $|\gamma| = 0.0$, 0.25 and 0.5, when the system is not in the PHS point, there is a strong increase in the height of the maximum Kondo-related peak (red curves) and in the depth of the minimum empty-orbital-related peak (green curves), as $|\gamma|$ increases from 0.0 to 0.5, which is the most striking characteristic of the thermopower shown here. That will contribute to the sizable ZT increase seen in Figure 7.26(b) and (c), at finite γ, when compared to zero-SOC [Figure 7.26(a)].

7.3.3 Universal behavior

In this section, we present a study of the universal behavior of the electrical and thermal conductances, as well as of the thermopower, as a function of temperature, for different values of ϵ_d, for $|\gamma| = 0$, and how this universal behavior changes for varying SOC.

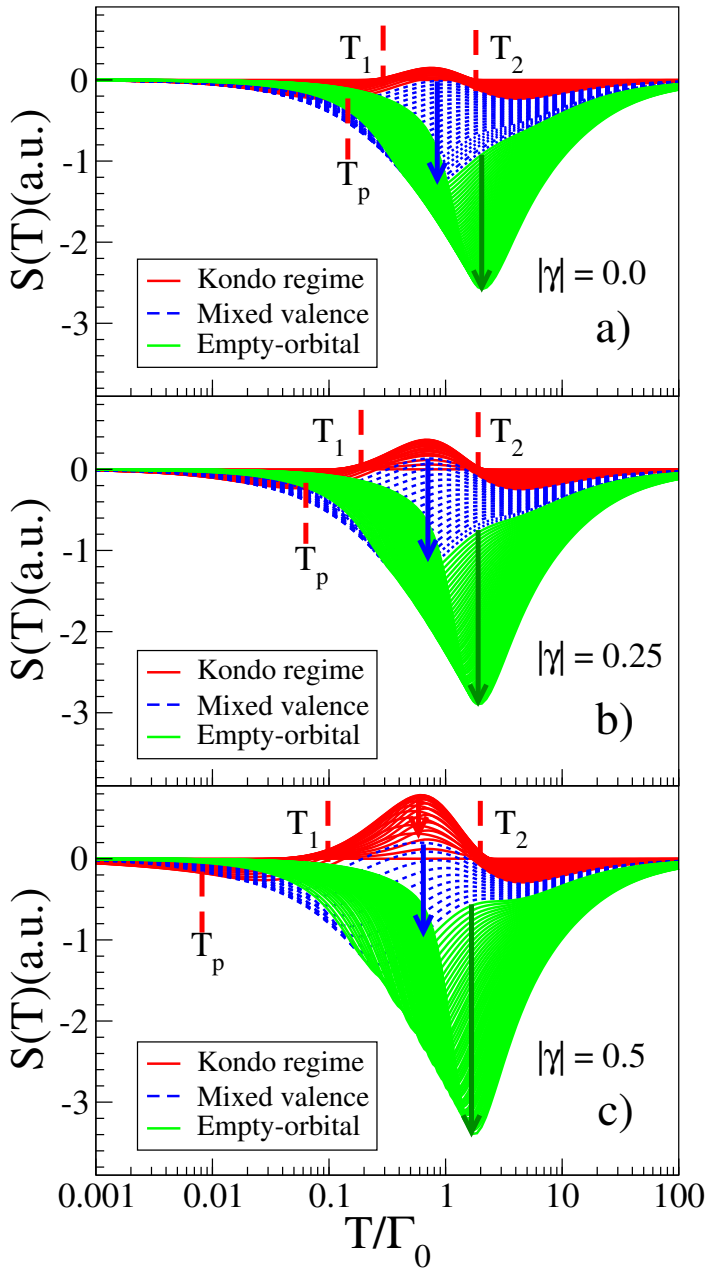

Figure 7.20: Same parameters as in Figs. 7.15 to 7.18, but now showing the thermopower $S(T)$ as a function of temperature. Notice the sizable change in the interval of variation of S(T) (increase in the maximum and minimum values) as a function of γ. This will be relevant to the TE figure of merit results in Figure 7.26. Again, the arrows indicate the direction of increasing values of ϵ_d.

In Figure 7.21(a), we plot the electrical conductance $^{G(T)}/_{G(0)}$ as a function of the scaled temperature $^{T}/_{T_{K\gamma}}$, for several ϵ_d values, for $|\gamma| = 0.0$, where $G(0)$ is given by Eq. (10) in Ref. [8]. As expected, the curves for the first four values of ϵ_d, which fall inside the Kondo regime, collapse into a single curve. On the other hand, the

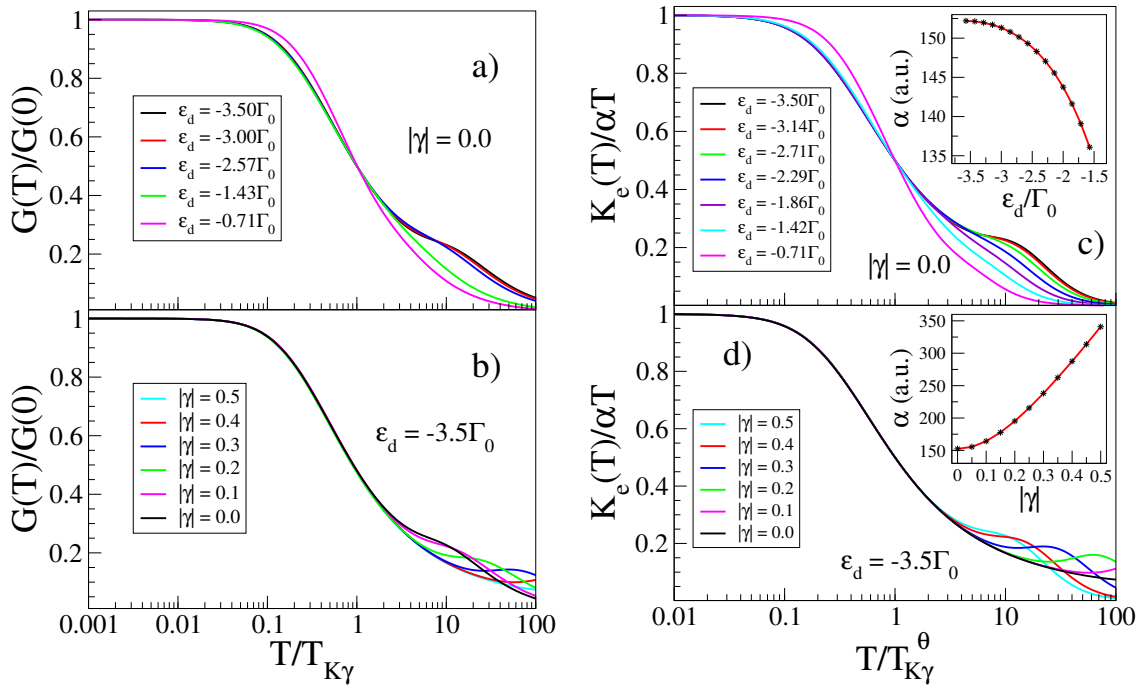

Figure 7.21: (a) Universal behavior of the electrical conductance $^{G(T)}/_{G(0)}$ for different values of ϵ_d and $|\gamma| = 0.0$ as a function of the scaled temperature $^{T}/_{T_{k\gamma}}$. The universality occurs inside the Kondo regime, since the magenta curve, which does not collapse, falls already inside the intermediate valence regime. (b) Universal behavior of $^{G(T)}/_{G(0)}$, as a function of the scaled temperature $^{T}/_{T_{K\gamma}}$, where all curves for different SOC ($0.0 \leq |\gamma| \leq 0.5$) collapse into a single curve $f(T/T_{K\gamma})$ for temperatures up to $T \gtrsim T_{K\gamma}$. In panel (c), like in panel (a), we show the universal behavior of the thermal conductance $^{K_e(T)}/_{\alpha T}$ as a function of the scaled temperature $^{T}/_{T^{\theta}_{K\gamma}}$, for several values of ϵ_d (inside the Kondo regime), for $|\gamma| = 0.0$. The single curve inside the intermediate valence regime ($\epsilon_d = -0.71\Gamma_0$, magenta curve) does not collapse into the Kondo regime universality function. (d) Universal behavior of $^{K_e(T)}/_{\alpha T}$, as a function of the scaled temperature $^{T}/_{T^{\theta}_{K\gamma}}$, where all curves for different SOC ($0.0 \leq |\gamma| \leq 0.5$) collapse into a single curve $g(T/T^{\theta}_{K\gamma})$. In both insets we show the values of α that produce the collapse.

cyan curve, for $\epsilon_d = -0.71\Gamma_0$, which is inside the intermediate valence regime [see Figure 7.15(a)], does not collapse into the other curves. The situation is similar if we stay at the PHS point and vary γ. In Figure 7.21(b) we plot $^{G(T)}/_{G(0)}$ in the PHS point, $\epsilon_d = {}^{-U}/_{2}$, as a function of the scaled temperature $^{T}/_{T_{K\gamma}}$, for different values of SOC, $0.0 \leq |\gamma| \leq 0.5$. In the Kondo regime, the electrical conductance presents a universal character: $^{G(T)}/_{G(0)} = f(^{T}/_{T_{K\gamma}})$, with a functional form that is independent of SOC. Note that the larger is $|\gamma|$, the further above $T_{K\gamma}$ remains the invariance of $f(^{T}/_{T_{K\gamma}})$ with γ.

We just saw that a quite interesting characteristic of electronic transport through

QDs is the universal behavior in the Kondo regime when the temperature is scaled by a characteristic temperature, such as $T_{K\gamma}$ for $G(T)$, as just shown above, or by $T^{\theta}_{K\gamma}$ for $K_e(T)$. The temperature $T^{\theta}_{K\gamma}$ is the equivalent of $T_{K\gamma}$ for $K_e(T)$ and can be computed using the Wiedemann-Franz law, Eq. (4.5), ${}^{K_e}/_{T} \approx L_o \times WF \times G(T)$, being defined by the relation [8]

$$\frac{K_e(T = T^{\theta}_{K\gamma})}{T^{\theta}_{K\gamma}} = \frac{\alpha}{2}, \tag{7.7}$$

where α is obtained through

$$\alpha = \lim_{T\to 0} \frac{K_e(T)}{T}. \tag{7.8}$$

In Figure 7.21(c), we plot the thermal conductance ${}^{K_e(T)}/_{\alpha T}$ as a function of the scaled temperature ${}^{T}/_{T^{\theta}_{K\gamma}}$, for several ${}^{-U}/_{2} \leq \epsilon_d \leq -0.71\Gamma_0$ and $|\gamma| = 0.0$. In the inset to panel (a), we plot the rescaling parameter α as a function of ϵ_d, in Γ_0 units. It is clear from the results that the rescaling by $T^{\theta}_{K\gamma}$ and α collapses all the $K_e(T)$ curves, for different ϵ_d, for $T \lesssim T^{\theta}_{K\gamma}$, onto a single universal curve. The exception, as in the case of the electric conductance, was for $\epsilon_d = -0.71$ (magenta curve), which is inside the intermediate valence regime. In Figure 7.21(d) we plot ${}^{K_e(T)}/_{\alpha T}$ at the PHS point, for different values of $|\gamma|$. In the Kondo regime, the thermal conductance thus presents a universal character: ${}^{K_e(T)}/_{\alpha T} = g({}^{T}/_{T^{\theta}_{K\gamma}})$, showing its invariance with SOC. In addition, in the PHS point, the thermal conductance obeys, by construction [see Eqs. (7.7) and (7.8)], ${}^{K_e(T)}/_{\alpha T} = 1.0$, at low temperatures. In the inset to panel (d), we plot the rescaling parameter α as a function of $|\gamma|$.

As pointed out by Costi *et al.* [8], in the Fermi liquid regime [118], ${}^{S(T)}/_{T}$, for a range of different values of ϵ_d in the Kondo regime, scales as

$$\frac{S(T)}{T} = -\frac{\pi\zeta}{e}\cot(\frac{\pi n_d}{2}), \tag{7.9}$$

where $-e$ is the electron charge, and the factor ζ can be obtained from the numerical value of $\lim_{T\to 0}|S(T)/T|$ and the occupation number n_d.

As done for the electric and thermal conductances Figs. 7.21, we will employ this procedure to rescale the temperature dependence of $S(T)$ to check the universality for varying ϵ_d (at $|\gamma| = 0.0$) and for varying γ at fixed ϵ_d. In Figure 7.22, we plot the thermopower $S(T)$, in units of ${}^{\pi\zeta T\cot(\pi n_d/2)}/_{e}$, as a function of the scaled temperature ζT,

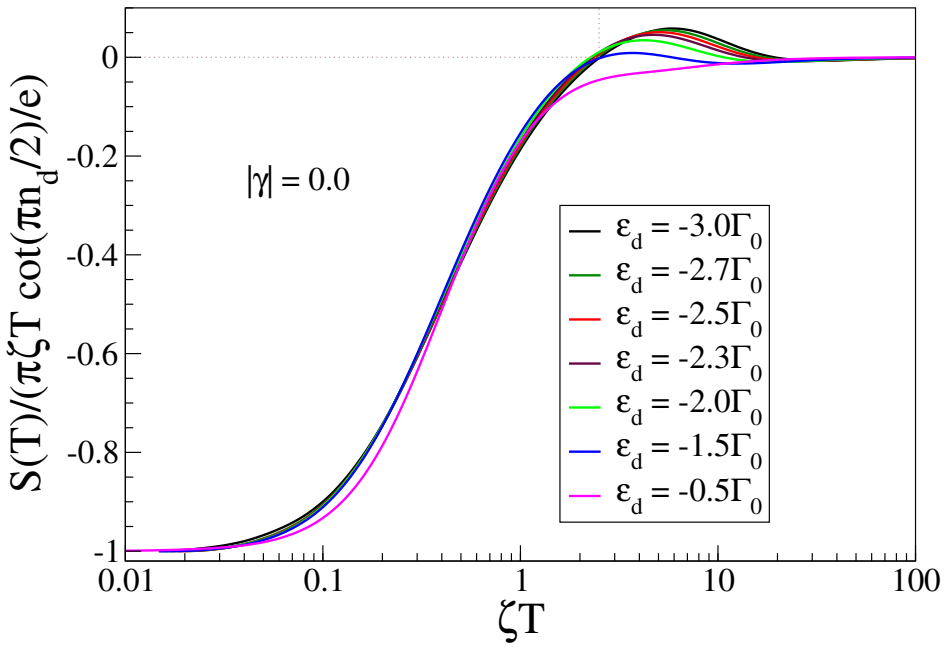

Figure 7.22: Temperature dependence of the thermopower $S(T)$, plotted in units of $\pi\zeta T\cot(\pi n_d/2)/e$ for $-3.0\Gamma_0 \leq \epsilon_d \leq -0.5\Gamma_0$ and $|\gamma| = 0.0$. Universality is achieved for $T \lesssim \zeta T$. As it happened for the electric and thermal conductances, the curve for the first value inside the intermediate valence regime ($\epsilon_d = -0.5$, magenta curve) does not collapse into the universal curve.

for several ϵ_d and $|\gamma| = 0.0$. In agreement with what we obtained for the electric and thermal conductances, $S(T)$ attains universality if we stay inside the Kondo regime, i.e., $-3.0\Gamma_0 \leq \epsilon_d \leq -1.5\Gamma_0$. For $\epsilon_d = -0.5$ (magenta curve) the universality is lost. In addition, since the sign of $S(T)$ is determined by the charge of the heat carriers ($S(T) > 0 \leftrightarrow$ holes, and $S(T) < 0 \leftrightarrow$ electrons), for temperatures below $\zeta T \simeq 2.0$ (see black dotted lines in Figure 7.22), the carriers are electrons, and, in a region above $\zeta T \simeq 2.0$ the carriers are holes. In the limit of high temperatures, $S(T) \to 0$.

Something curious, however, occurs when we analyze the universality at fixed ϵ_d and $0.0 \leq |\gamma| \leq 0.5$. As shown in Figure 7.23, where panels (a) to (i) show the scaling of $S(T)$ for different values of ϵ_d in the interval $-3.2\Gamma_0 \leq \epsilon_d \leq \Gamma_0$ (spanning the Kondo and intermediate valence regimes), the universality is achieved only deep into the intermediate valence regime (panels (c) and (d), for $\epsilon_d = 0.0\Gamma_0$ and $-0.5\Gamma_0$, respectively). This is in contrast to what was observed for the electric and thermal conductances Figure 7.21, where the universality was observed inside the Kondo regime.

In Figure 7.24, we re-plot Figure 7.23(d) ($S(T)$ for $\epsilon_d = -0.5\Gamma_0$) to study the variation of $T_{K\gamma}$ with γ (top inset), the dependence of the Fermi liquid parameter

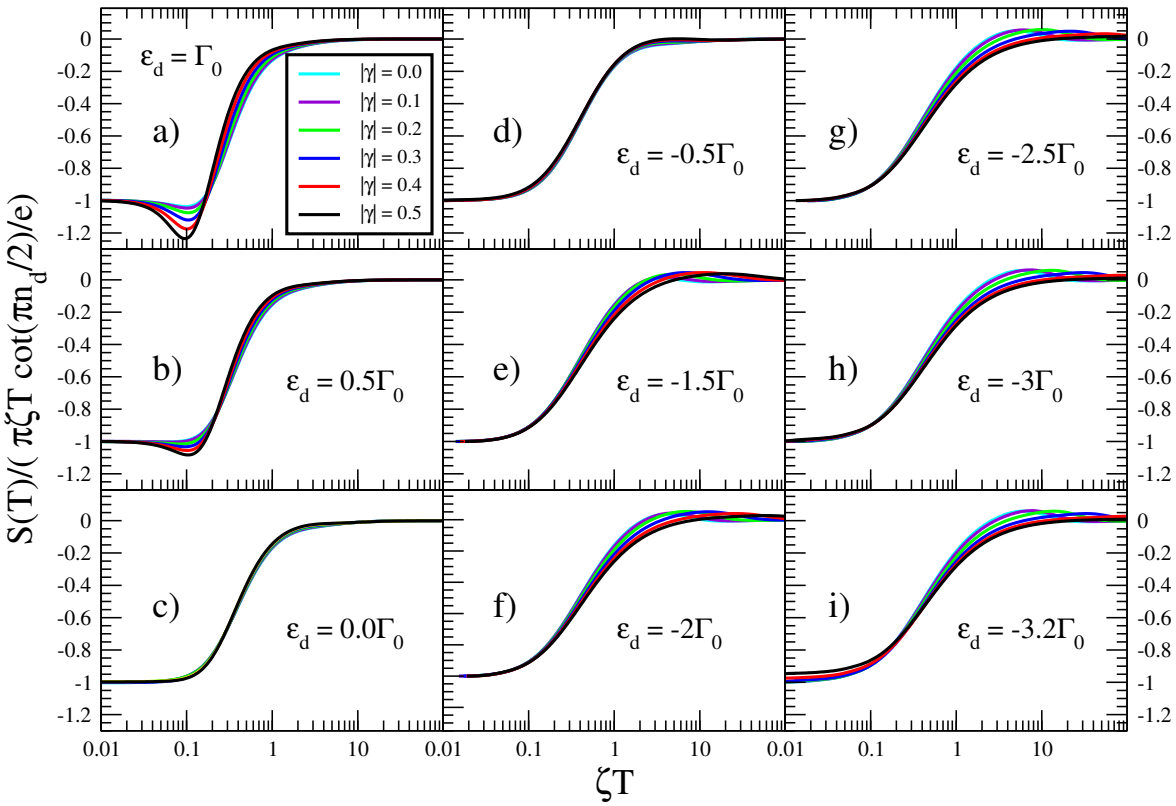

Figure 7.23: (a) to (i): Comparison of thermopower universality in the Kondo and intermediate valence regimes. Each panel contains the scaled thermopower (for $0.0 \leq |\gamma| \leq 0.5$) for different values of ϵ_d. Notice how the universality is more complete in the intermediate valence regime. Indeed, panels (c) and (d), for $\epsilon_d = 0.0\Gamma_0$ and $-0.5\Gamma_0$, present the more complete collapse of the thermopower results for different values of γ. These two values of ϵ_d are deep into the intermediate valence regime, for all values of γ [see Figure 7.17].

ζ with γ (bottom-left inset), and the dependence of the QD occupancy n_d with γ (bottom-right inset). As expected, since the increase in γ moves the system in the Kondo regime direction, we see that there is a non-monotonic increase in n_d as γ increases (bottom-right inset), while, as expected too, T_K decreases with γ (top inset). In addition, there is a corresponding increase in ζ with γ (bottom-left inset).

Thus, we have analyzed two types of universalities for the quantities $G(T)$, $K_e(T)$, and $S(T)$: (i) zero-SOC and varying ϵ_d, for which we found that there is universality for $G(T)$, $K_e(T)$, and $S(T)$ in the Kondo regime [see Figs. 7.21(a), 7.21(c), and 7.22]; (ii) fixed ϵ_d and varying γ, for which both $G(T)$ and $K_e(T)$ show universality in the Kondo regime [see Figs. 7.21(b) and 7.21(d)], while, unexpectedly, $S(T)$ shows universality in the intermediate valence regime (Figure 7.23). Additional theoretical and/or

experimental research is needed to clarify the reason for this unexpected behavior.

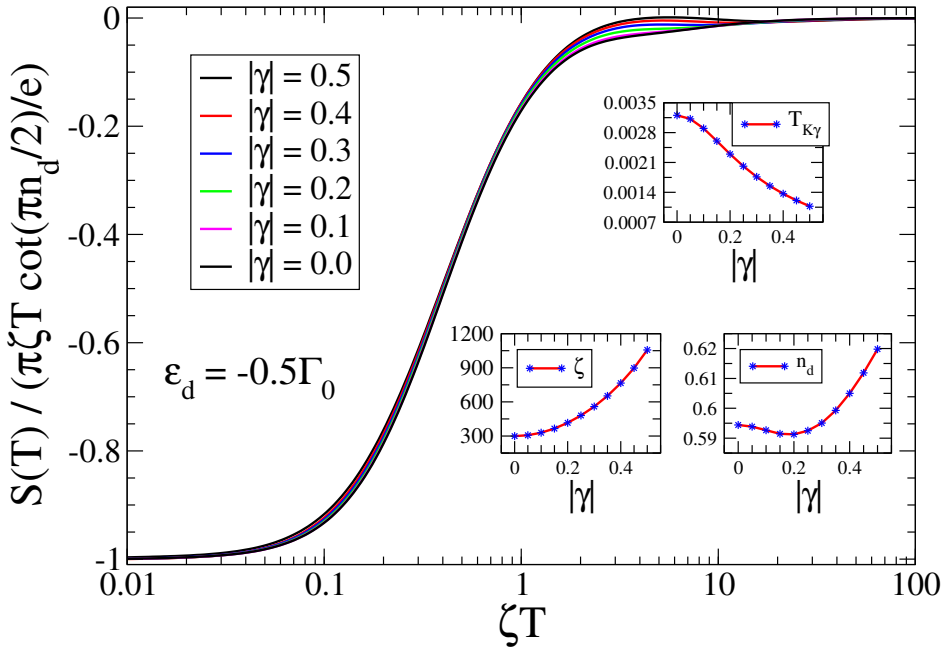

Figure 7.24: Same as in Figure 7.22, but for $0.0 \leq |\gamma| \leq 0.5$ and $\epsilon_d = -0.5\Gamma_0$. Top inset: $T_{K\gamma}$ as a function of γ; bottom-left inset: ζ as a function of γ; bottom-right inset: QD occupation n_d as a function of γ.

In panels (a) and (b) in Figure 7.25, we show the Wiedemann-Franz law, in units of the Lorenz number L_o, and the thermopower S, respectively, as a function of ϵ_d (in units of Γ_0), at various temperature values (also in units of Γ_0), for $|\gamma| = 0$ and $U = 7.0\Gamma_0$. At the lowest temperature ($T = 0.011\Gamma_0$, cyan curve), the Wiedemann-Franz law is satisfied, aside from a small region around the PHS point ($\epsilon_d = -3.5\Gamma_0$), where $WF \lesssim 1$. As the temperature increases, the width of this region increases, as well as the departure of WF from 1. In addition, two broad peaks appear farther away from the PHS point (on the left and right of it), whose violation of the Wiedemann-Franz law (now, $WF > 1$) becomes more severe, as the temperature increases. In addition, the maxima of the left and right peaks gradually move away from the PHS point with increasing temperature.

A somewhat similar picture describes the results for $S(\epsilon_d)$ in Figure 7.25(b), with the difference that now $S(\epsilon_d)$ is odd in relation to the PHS point. In addition, left and right broad peaks emerge away from the PHS point, similarly located and with similar temperature dependence as the ones shown for WF in Figure 7.25(a). As a consequence, given that $ZT = {}^{S^2}/_{WF}$, and since $S \gtrsim WF$ at and around those broad peaks, this determines the relatively high values attained by ZT in the peaks region,

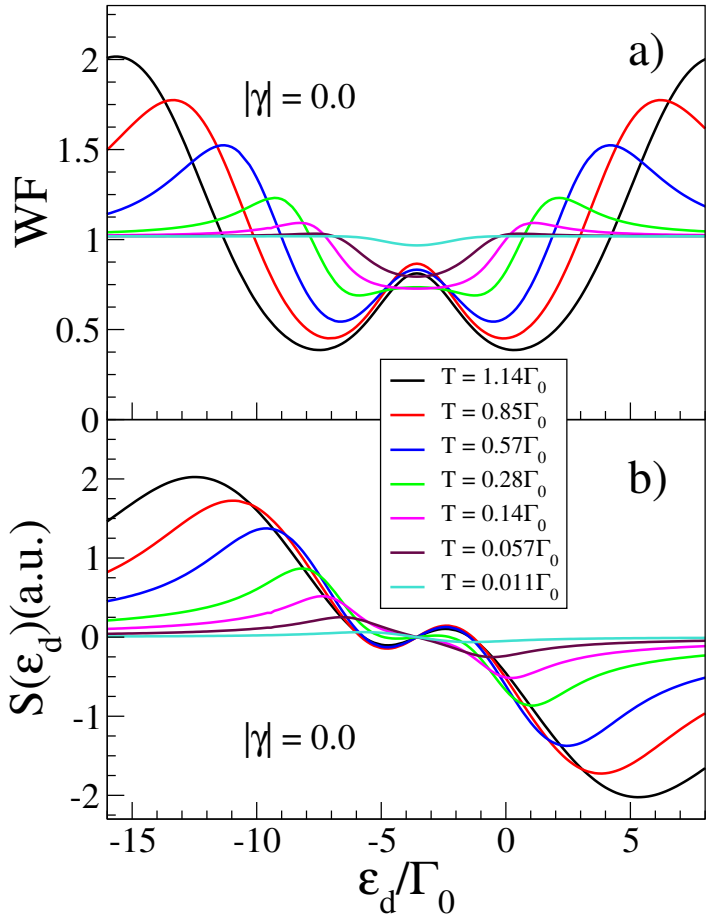

Figure 7.25: (a) Wiedemann-Franz law (in units of the Lorenz number, L_o) and (b) Thermopower S, as a function of ϵ_d, for several values of temperature (in units of Γ_0), for $U = 7.0\Gamma_0$ and $|\gamma| = 0.0$.

as shown in Figure 7.26(a), for $|\gamma| = 0.0$ and several temperatures.

In panels (b) and (c) in Figure 7.26, we show the dimensionless TE figure of merit ZT as a function of ϵ_d, at various temperatures, for finite SOC, $|\gamma| = 0.25$ and 0.5, respectively. When compared to Figure 7.26(a), for $|\gamma| = 0.0$, we observe a sizable enhancement of ZT with SOC, which results from the increase of $S(T)$ with SOC, as indicated in the $S(T)$ maps in Figure 7.20. We notice that, compared to the $|\gamma| = 0.0$ maximum value of $ZT \approx 4.0$ in Figure 7.26(a) ($T = 1.14\Gamma_0$), the $ZT \approx 10.0$ obtained for $|\gamma| = 0.5$, for the same temperature, represents an improvement in ZT of ≈ 2.5 times.

Finally, we should note that, as previously mentioned, in the calculation of these ZT results, we do not consider any phononic contribution, which tends to compete with

the electronic contribution to decrease the ZT values as the temperature is increased. However, note that we kept the maximum temperature studied at a low enough value that justifies the neglect of phonons.

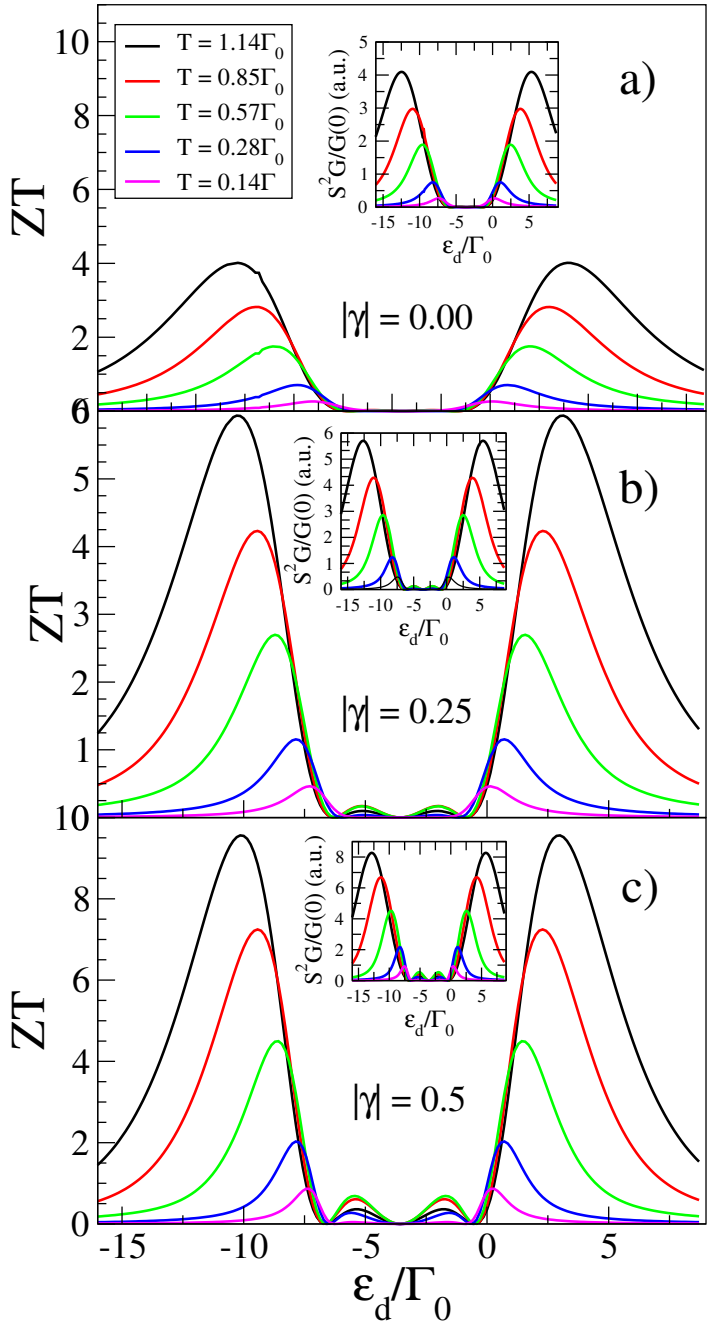

Figure 7.26: Dimensionless TE figure o merit ZT as a function of ϵ_d, for several values of temperature (both in units of Γ_0) and $U = 7.0\Gamma_0$. Panels (a), (b), and (c) are for $|\gamma| = 0.0$, 0.25, and 0.5, respectively.

Chapter 8

Conclusions

8.1 Summary of thesis achievements

- Based on the results presented in Chap. 3 and Sec. 7.1, we have shown, through a physically motivated change of basis, that the 1D finite-SOC SIAM Hamiltonian is similar to that for the zero-SOC SIAM. The form of the 1D finite-SOC SIAM Hamiltonian (for both the S_z and helicity bases) seems to be inappropriate to deal with Kondo physics, since conduction channels with opposite quantum numbers (either $\sigma = \uparrow\downarrow$ or $\nu = \pm$) are mixed (either by SOC, or by the impurity itself). This issue can be circumvented if one exploits the fact that time-reversal symmetry is not broken. Indeed, it is the time-reversal symmetry that renders the finite-SOC hybridization matrix diagonal and spin-independent (in any spin basis), thus a scalar, like the zero-SOC hybridization function. This can be seen in a more clear way once *both* the impurity and the conduction electrons are rotated to the σ_r basis, where it becomes clear that the spin channels are not mixed neither by SOC, nor by the impurity, allowing a simple analytical treatment of the renormalized $\tilde{T}_K$, through the use of the Haldane expression, which is corroborated by NRG calculations in the wide-band regime ($D \gg U, \Delta, |\epsilon_0|$). In addition, NRG results for the intermediate regime ($U = D > \Delta$, with Fermi energy close to the bottom of the band), in qualitative agreement with QMC results presented in Ref. [62], indicate that it is the proximity of the Fermi energy to the structure at the bottom of the hybridization function (a singularity) that causes the deviation of the results from what one expects from Haldane's expression. Finally, it is shown

that the 1D SOC-SIAM Hamiltonian, for arbitrary values of α_R and β, has a PSH SU(2) symmetry, in contrast to the 2D SOC Fermi sea, where the PSH state is restricted to the $\alpha_R = \beta$ case.

- We have studied the effect of 1D conduction band SOC over the TE transport properties of an SET. This was done, using NRG, through the calculation of temperature maps of the TE properties. We have shown that SOC drives the system deeper into the Kondo regime. We also showed that the Kondo regime universality of thermal and electrical conductances is maintained in the presence of SOC. We also show the interesting result that $S(T)$, which is universal in the Kondo regime at zero-SOC, presents a more universal behavior (for different γ) in the intermediate valence regime, when compared to the Kondo regime. More importantly, we have shown that the large increases in the thermopower, caused by SOC (see Fig. 7.20), translate into notable SOC-caused enhancements of the TE figure of merit ZT (see Fig. 7.26) for an embedded SET coupled to 1D leads.

8.2 Perspectives

- Interesting points to consider in future research are (i) application of the present work formalism to a three-terminal TE device that directly transforms thermal into electrical energy [51]; (ii) determining what is the role played by the leads dimensionality in the sizable increase of the figure of merit observed for 1D leads; (iii) the Rashba and Dresselhaus conduction band SOC results obtained here can be extended to study two-dimensional (2D) systems, like the surface states of the Kondo insulators SmB_6 and $FeSb_2$ [17–20]. Some recent experimental results point out that a combination of Rashba- and Dresselhaus-like SOC [119–122] can describe the states around the X point of the Brillouin zone; (iv) finally, we would like to study the TE properties of an SET embedded in a 2D electron gas at the Persistent Spin Helix point ($\alpha_R = \beta$) [96].

Appendix A

Density of state in the helical space

The change on the energy band leads us to think and to do the question, how the density of states of the conduction electrons is modified by the SOC presence in the base S_z?.

Then, to answer the previous question, the density of states is the imaginary part of the Green function to free conduction electrons such as defined (A.1). The quantum wire Hamiltonian is diagonal in quantum number ν with eigenvalues (3.14) and eigenstates (3.15), and as consequence, ν is a good quantum number to the system without impurity. In this new basis each states $|k\nu\rangle$ are a linear superposition of the states $|k\sigma\rangle$ such as observed in the equation (3.15). Then, the SOC effect changes the spin direction through a phase ϕ, which we will analyze later together with space ν. So, the retarded Green function to the free electron at the state $|k\nu\rangle$ can be defined as

$$G^{\nu}_{kk'}(\omega) = \frac{\delta_{kk'}}{\omega - \epsilon^{\nu}_{k} + i\eta}, \tag{A.1}$$

as can be noticed from (A.1), the Green function of one particle without interaction has its singularity poles at the eigenvalues of the Hamiltonian, and the density of states is

$$\rho^{\nu}(\omega) = -\frac{1}{\pi} Im\{G^{\nu}_{kk}(\omega)\}. \tag{A.2}$$

To integrate the imaginary part of $G^{\nu}_{kk}(\omega)$, the relation dispersion (3.14) we have

expressed as $-2|z|\cos(ka-\nu\vartheta_k)$, where $\vartheta_k=(-\frac{|\gamma|}{t};k<0)$, and $\vartheta_k=(\frac{|\gamma|}{t};k>0)$, the number z is a complex number defined as $t+i\ sgn(k)|\gamma|$, in this integration process we change the integral variable k to the energy variable $dk\rightarrow[\frac{\partial\epsilon_k^\nu}{\partial k}]^{-1}d\epsilon_k^\nu$, from where we obtained

$$\rho^{-}_{(\omega)}=\begin{cases}\frac{2}{\pi\sqrt{4|z|^2-\omega^2}}, & 2t < \omega < 2|z| \\ \frac{1}{\pi\sqrt{4|z|^2-\omega^2}}, & -2t \leq \omega \leq 2t \\ 0, & -2|z| < \omega \leq -2t\end{cases}, \tag{A.3}$$

$$\rho^{+}_{(\omega)}=\begin{cases}0, & 2t < \omega \leq 2|z| \\ \frac{1}{\pi\sqrt{4|z|^2-\omega^2}}, & -2t < \omega \leq 2t \\ \frac{2}{\pi\sqrt{4|z|^2-\omega^2}}, & -2|z| \leq \omega \leq -2t\end{cases}. \tag{A.4}$$

This results can be seen in figure A.1 further of the $\rho^{\pm}(\omega)$ we graphics the $\rho_0(\omega)$ for the physical system without SOC, the $\rho_0(\omega)$ is defined within the interval $[-2t:2t]$.

The change observed in the dispersion relation (3.14) also can be observed in the density of state $\rho^{\nu}(\omega)$, where to the case $\rho^{-}(\omega)$ the energy states was moved to the top edge band, in this interval region $[2t:2|z|\rangle$ the density of states is two times $\rho_0(\omega)$ and the $\rho^{+}(\omega)=0$; by the other hand $\rho^{+}(\omega)$ shown that the energy states has been moved to bottom edge band, where $\rho^{+}(\omega)$ is two times $\rho_0(\omega)$ interval where $\rho^{-}(\omega)$ becomes zero; while in the interval $[-2t:2t]$ both densities $\rho^{+}(\omega)$ and the $\rho^{-}(\omega)$ shown the same behavior and they are same. Then, the SOC effect for conduction electrons rearranges the energy states to the edge band, (be it bottom or top of the band) in the space ν, that, due to this rearrangement of the states the density of states is zero on the opposite edge of the band respect to the edge where the rearrangement occurs, which is showed in the figure A.1.

A.1 Helicity operator

The helicity operator, in a system with spin-full relativistic particles, describes the spin projection in the momentum $\hbar\boldsymbol{k}$ direction. In the Dirac equation, the operator is given simply by $\hat{p}\cdot\sigma$ [123]. But, in the non-relativistic limit, for a system with finite SOC,

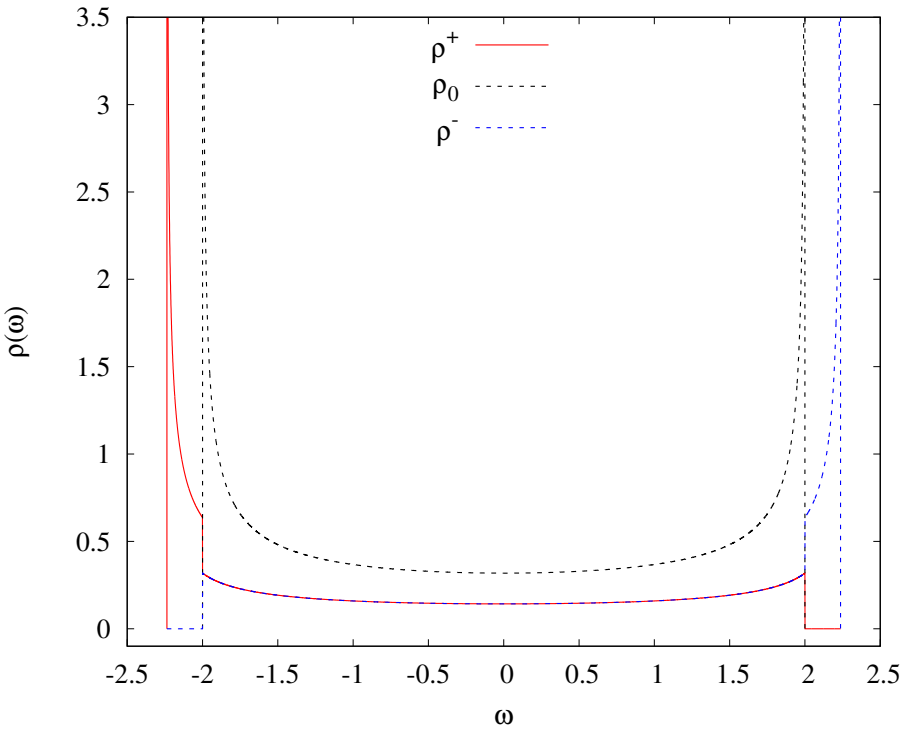

Figure A.1: Density of states in the space ν showing the SOC effect to $|\gamma| = 0.5$. The densities ρ^+, ρ^- and ρ_0 are showed by the curves red, blue and black color respectively. ρ_0 represent the case where $|\gamma| = 0.0$, and both densities ρ^-, ρ^+ are degenerates in this interval.

the spin does not necessarily is projected into the direction of the momentum. It is projected instead into a direction orthogonal to $\hat{p}$, dependent on the specific type of SOC interaction the electron is subjected to.

In the specific case of having both Rashba and Dresselhaus SOC, we define the helicity operator [124], as

$$\hat{h} = s_k \left(\cos(\phi)\sigma_x + \sin(\phi)\sigma_y\right) = s_k \begin{pmatrix} 0 & e^{-i\phi} \\ e^{i\phi} & 0 \end{pmatrix}, \tag{A.5}$$

where σ_x and σ_y are Pauli's matrices, the S_k is defined by the equation (3.16). The helical operator satisfy the relations $[H_0; \hat{h}] = 0$, $[H_{soc}; \hat{h}] = 0$, and its eigenstates are

$$|h\pm\rangle = \frac{1}{\sqrt{2}} \left(|\uparrow\rangle \pm s_k e^{i\phi} |\downarrow\rangle\right). \tag{A.6}$$

We can notice that the expression (A.6) is the same spin wave function of the eigenstates (3.15), and consequently we defined the states $|k\sigma\rangle$ and $|k\pm\rangle$ are creates by the operators $c^{\dagger}_{k\sigma}$ and $c^{\dagger}_{k\pm}$, respectively, therefore we can write $|k\sigma\rangle = c^{\dagger}_{k\sigma}|0\rangle$ and $|k\pm\rangle = c^{\dagger}_{k\pm}|0\rangle$. Then, the operator $\hat{h}$ in the second quantization can be

$$\hat{h} = s_k(e^{-i\phi}c^{\dagger}_{k\uparrow}c_{k\downarrow} + e^{i\phi}c^{\dagger}_{k\downarrow}c_{k\uparrow}). \tag{A.7}$$

The operators $c^{\dagger}_{k\pm}$, creates conduction electrons with momento k and quantum number ν, while $c^{\dagger}_{k\sigma}$ is the creation electron operator in the base S_z. Then, the helicity space and the spin space are related by an unitary transformation U defined as

$$U = \frac{1}{\sqrt{2}}\begin{pmatrix} 1 & S_k e^{i\phi} \\ 1 & -S_k e^{i\phi} \end{pmatrix} \tag{A.8}$$

where $UU^{\dagger} = 1$, and the operators $c^{\dagger}_{k\pm}$ and $c^{\dagger}_{k\sigma}$ are related by

$$\begin{pmatrix} c^{\dagger}_{k+} \\ c^{\dagger}_{k-} \end{pmatrix} = U \begin{pmatrix} c^{\dagger}_{k\uparrow} \\ c^{\dagger}_{k\downarrow} \end{pmatrix}. \tag{A.9}$$

The expression (A.7) under transformation (A.9) the helicity operator can be write as

$$\hat{h} = \sum_{\nu} \nu S_k n_{k\nu}. \tag{A.10}$$

Bibliography

[1] C. B. Vining, *Semiconductors are cool*, Nature **413**, 577–578 (2001).

[2] W. de Haas, J. de Boer, and G. van dën Berg, *The electrical resistance of gold, copper and lead at low temperatures*, Physica **1**, 1115–1124 (1934).

[3] A. Clogston, B. Matthias, M. Peter, H. Williams, E. Corenzwit, and R. Sherwood, *Local magnetic moment associated with an iron atom dissolved in various transition metal alloys*, Physical Review **125**, 541 (1962).

[4] M. Sarachik, E. Corenzwit, and L. Longinotti, *Resistivity of mo-nb and mo-re alloys containing 1% fe*, Physical Review **135**, A1041 (1964).

[5] Y. Nagaoka, *Self-consistent treatment of Kondo's effect in dilute alloys*, Physical Review **138**, A1112 (1965).

[6] P. W. Anderson, *Localized magnetic states in metals*, Physical Review **124**, 41 (1961).

[7] T. Lobo, M. Figueira, and M. Foglio, *The atomic approach to the Anderson model for the finite U case: application to a quantum dot*, Nanotechnology **21**, 274007 (2010).

[8] T. Costi and V. Zlatić, *Thermoelectric transport through strongly correlated quantum dots*, Physical Review B **81**, 235127 (2010).

[9] L. Kouwenhoven and L. Glazman, *Revival of the Kondo effect*, Physics world **14**, 33 (2001).

[10] D. Goldhaber-Gordon, J. Göres, M. A. Kastner, H. Shtrikman, D. Mahalu, and U. Meirav, *From the Kondo Regime to the Mixed-Valence Regime in a Single-Electron Transistor*, Phys. Rev. Lett. **81**, 5225–5228 (1998).

[11] D. Sánchez and R. López, *Nonlinear phenomena in quantum thermoelectrics and heat*, C. R. Phys. **17**, 1060 – 1071 (2016).

[12] T. Tritt. *Thermoelectric Materials: Principles, Structure, Properties, and Applications*. In K. J. Buschow, R. W. Cahn, M. C. Flemings, B. Ilschner, E. J. Kramer, S. Mahajan, and P. Veyssiere, editors, *Encyclopedia of Materials: Science and Technology*, page 1. Elsevier, Oxford, (2002).

[13] A. Shakouri, *Recent Developments in Semiconductor Thermoelectric Physics and Materials*, Annu. Rev. Mater. Res. **41**, 399 (2011).

[14] T. M. Tritt, *Thermoelectric Phenomena, Materials, and Applications*, Annu. Rev. Mater. Res. **41**, 433 (2011).

[15] H. J. Goldsmid and R. W. Douglas, *The use of semiconductors in thermoelectric refrigeration*, Br. J. Appl. Phys. **5**, 386 (1954).

[16] Y. L. Chen, J. G. Analytis, J.-H. Chu, Z. K. Liu, S.-K. Mo, X. L. Qi, H. J. Zhang, D. H. Lu, X. Dai, Z. Fang, S. C. Zhang, I. R. Fisher, Z. Hussain, and Z.-X. Shen, *Experimental Realization of a Three-Dimensional Topological Insulator, Bi2Te3*, Science **325**, 178 (2009).

[17] N. Xu, Y. Xu, and J. Zhu, *Topological insulators for thermoelectrics*, npj Quantum Mater. **2**, 51 (2017).

[18] K.-J. Xu, S.-D. Chen, Y. He, J. He, S. Tang, C. Jia, E. Yue Ma, S.-K. Mo, D. Lu, M. Hashimoto, T. P. Devereaux, and Z.-X. Shen, *Metallic surface states in a correlated d-electron topological Kondo insulator candidate FeSb2*, Proc. Natl. Acad. Sci. U.S.A. **117**, 15409 (2020).

[19] Figueira, M.S., Silva-Valencia, J., and Franco, R., *Thermoelectric properties of the Kondo insulator FeSb2*, Eur. Phys. J. B **85**, 203 (2012).

[20] J. Gooth, G. Schierning, C. Felser, and K. Nielsch, *Quantum materials for thermoelectricity*, MRS Bull. **43**, 187–192 (2018).

[21] A. Manchon, H. C. Koo, J. Nitta, S. Frolov, and R. Duine, *New perspectives for Rashba spin–orbit coupling*, Nature materials **14**, 871 (2015).

[22] M. Ahmad, K. Agarwal, and B. R. Mehta, *An anomalously high Seebeck coefficient and power factor in ultrathin Bi2Te3 film: Spin–orbit interaction*, J. Appl. Phys. **128**, 035108 (2020).

[23] R. Takahashi and S. Murakami, *Thermoelectric transport in topological insulators*, Semicond. Sci. Technol. **27**, 124005 (2012).

[24] M. Cassinelli, S. Müller, K.-O. Voss, C. Trautmann, F. Völklein, J. Gooth, K. Nielsch, and M. E. Toimil-Molares, *Influence of surface states and size effects on the Seebeck coefficient and electrical resistance of Bi1-xSbx nanowire arrays*, Nanoscale **9**, 3169–3179 (2017).

[25] J. V. V. Cassiano and G. B. Martins, *Electric-field-generated topological states in a silicene nanotube*, J. Phys. Condens. Matter **33**, 175301 (2021).

[26] J. He and T. M. Tritt, *Advances in thermoelectric materials research: Looking back and moving forward*, Science **357**, 1369 (2017).

[27] N. Jaziri, A. Boughamoura, J. Müller, B. Mezghani, F. Tounsi, and M. Ismail, *A comprehensive review of Thermoelectric Generators: Technologies and common applications*, Energy Rep. **6**, 264 (2020).

[28] M. Barrubeeah, M. Rady, A. Attar, F. Albatati, and A. Abuhabaya, *Design, modeling and parametric optimization of thermoelectric cooling systems for high power density electronic devices*, International Journal of Low-Carbon Technologies (2021).

[29] G. J. Snyder and E. S. Toberer, *Complex thermoelectric materials*, Materials for sustainable energy: a collection of peer-reviewed research and review articles from Nature Publishing Group , 101–110 (2011).

[30] L. D. Hicks and M. S. Dresselhaus, *Effect of quantum-well structures on the thermoelectric figure of merit*, Phys. Rev. B **47**, 12727–12731 (1993).

[31] L. D. Hicks and M. S. Dresselhaus, *Thermoelectric figure of merit of a one-dimensional conductor*, Phys. Rev. B **47**, 16631–16634 (1993).

[32] D. Boese and R. Fazio, *Thermoelectric effects in Kondo-correlated quantum dots*, Europhysics Letters (EPL) **56**, 576–582 (2001).

[33] M. Yoshida and L. N. d. Oliveira, *Thermoelectric effects in quantum dots*, Physica B: Condensed Matter **404**, 3312–3315 (2009).

[34] S. Hershfield, K. A. Muttalib, and B. J. Nartowt, *Nonlinear thermoelectric transport: A class of nanodevices for high efficiency and large power output*, Phys. Rev. B **88**, 085426 (2013).

[35] S. Donsa, S. Andergassen, and K. Held, *Double quantum dot as a minimal thermoelectric generator*, Phys. Rev. B **89**, 125103 (2014).

[36] V. Talbo, J. Saint-Martin, S. Retailleau, and P. Dollfus, *Non-linear effects and thermoelectric efficiency of quantum dot-based single-electron transistors*, Sci. Rep. **7**, 14783 (2017).

[37] T. A. Costi, *Magnetic field dependence of the thermopower of Kondo-correlated quantum dots*, Phys. Rev. B **100**, 161106 (2019).

[38] T. A. Costi, *Magnetic field dependence of the thermopower of Kondo-correlated quantum dots: Comparison with experiment*, Phys. Rev. B **100**, 155126 (2019).

[39] Y. Kleeorin, H. Thierschmann, H. Buhmann, A. Georges, L. W. Molenkamp, and Y. Meir, *How to measure the entropy of a mesoscopic system via thermoelectric transport*, Nat. Commun. **10**, 5801 (2019).

[40] U. Eckern and K. I. Wysokiński, *Two- and three-terminal far-from-equilibrium thermoelectric nano-devices in the Kondo regime*, New J. Phys. **22**, 013045 (2020).

[41] J. P. Heremans, C. M. Thrush, and D. T. Morelli, *Thermopower enhancement in lead telluride nanostructures*, Phys. Rev. B **70**, 115334 (2004).

[42] R. Scheibner, H. Buhmann, D. Reuter, M. Kiselev, and L. Molenkamp, *Thermopower of a Kondo spin-correlated quantum dot*, Phys. Rev. Lett. **95**, 176602 (2005).

[43] R. Scheibner, E. G. Novik, T. Borzenko, M. König, D. Reuter, A. D. Wieck, H. Buhmann, and L. W. Molenkamp, *Sequential and cotunneling behavior in the temperature-dependent thermopower of few-electron quantum dots*, Phys. Rev. B **75**, 041301 (2007).

[44] R. Scheibner, M. König, D. Reuter, A. Wieck, C. Gould, H. Buhmann, and L. Molenkamp, *Quantum dot as thermal rectifier*, New J. Phys. **10**, 083016 (2008).

[45] E. A. Hoffmann, H. A. Nilsson, J. E. Matthews, N. Nakpathomkun, A. I. Persson, L. Samuelson, and H. Linke, *Measuring Temperature Gradients over Nanometer Length Scales*, Nano Lett. **9**, 779–783 (2009).

[46] B. Dutta, J. T. Peltonen, D. S. Antonenko, M. Meschke, M. A. Skvortsov, B. Kubala, J. König, C. B. Winkelmann, H. Courtois, and J. P. Pekola, *Thermal Conductance of a Single-Electron Transistor*, Phys. Rev. Lett. **119**, 077701 (2017).

[47] N. Hartman, C. Olsen, S. Lüscher, M. Samani, S. Fallahi, G. C. Gardner, M. Manfra, and J. Folk, *Direct entropy measurement in a mesoscopic quantum system*, Nat. Phys. **14**, 1083–1086 (2018).

[48] A. Svilans, M. Josefsson, A. M. Burke, S. Fahlvik, C. Thelander, H. Linke, and M. Leijnse, *Thermoelectric Characterization of the Kondo Resonance in Nanowire Quantum Dots*, Phys. Rev. Lett. **121**, 206801 (2018).

[49] B. Dutta, D. Majidi, A. García Corral, P. A. Erdman, S. Florens, T. A. Costi, H. Courtois, and C. B. Winkelmann, *Direct Probe of the Seebeck Coefficient in a Kondo-Correlated Single-Quantum-Dot Transistor*, Nano Lett. **19**, 506–511 (2019).

[50] G. Benenti, G. Casati, K. Saito, and R. S. Whitney, *Fundamental aspects of steady-state conversion of heat to work at the nanoscale*, Phys. Rep. **694**, 1 – 124 (2017).

[51] R. Sánchez and M. Büttiker, *Optimal energy quanta to current conversion*, Phys. Rev. B **83**, 085428 (2011).

[52] B. Sothmann, R. Sánchez, and A. N. Jordan, *Thermoelectric energy harvesting with quantum dots*, Nanotechnology **26**, 032001 (2014).

[53] J. Yuan, Y. Cai, L. Shen, Y. Xiao, J.-C. Ren, A. Wang, Y. P. Feng, and X. Yan, *One-dimensional thermoelectrics induced by Rashba spin-orbit coupling in two-dimensional BiSb monolayer*, Nano Energy **52**, 163–170 (2018).

[54] Y. Meir and N. S. Wingreen, *Spin-orbit scattering and the Kondo effect*, Phys. Rev. B **50**, 4947–4950 (1994).

[55] J. Malecki, *The two dimensional Kondo model with Rashba spin-orbit coupling*, Journal of Statistical Physics **129**, 741–757 (2007).

[56] R. Žitko and J. Bonča, *Kondo effect in the presence of Rashba spin-orbit interaction*, Phys. Rev. B **84**, 193411 (2011).

[57] M. Zarea, S. E. Ulloa, and N. Sandler, *Enhancement of the Kondo Effect through Rashba Spin-Orbit Interactions*, Phys. Rev. Lett. **108**, 046601 (2012).

[58] D. Mastrogiuseppe, A. Wong, K. Ingersent, S. E. Ulloa, and N. Sandler, *Kondo effect in graphene with Rashba spin-orbit coupling*, Phys. Rev. B **90**, 035426 (2014).

[59] A. Wong, S. E. Ulloa, N. Sandler, and K. Ingersent, *Influence of Rashba spin-orbit coupling on the Kondo effect*, Phys. Rev. B **93**, 075148 (2016).

[60] L. Chen, J. Sun, H.-K. Tang, and H.-Q. Lin, *The Kondo temperature of a two-dimensional electron gas with Rashba spin-orbit coupling*, J. Phys. Condens. Matter **28**, 396005 (2016).

[61] G. de Sousa, J. F. Silva, and E. Vernek, *Kondo effect in a quantum wire with spin-orbit coupling*, Physical Review B **94**, 125115 (2016).

[62] L. Chen and R.-S. Han, *Kondo temperature of Anderson impurity model in a quantum wire with spin-orbit coupling*, arXiv preprint arXiv:1711.05505 (2017).

[63] V. Lopes, G. B. Martins, M. A. Manya, and E. V. Anda, *Kondo effect under the influence of spin–orbit coupling in a quantum wire*, Journal of Physics: Condensed Matter **32**, 435604 (2020).

[64] P. Dutta, A. Saha, and A. M. Jayannavar, *Thermoelectric properties of a ferromagnet-superconductor hybrid junction: Role of interfacial Rashba spin-orbit interaction*, Phys. Rev. B **96**, 115404 (2017).

[65] L. Karwacki and J. Barnaś, *Thermoelectric properties of a quantum dot coupled to magnetic leads by Rashba spin-orbit interaction*, Phys. Rev. B **98**, 075413 (2018).

[66] R. Bulla, T. A. Costi, and T. Pruschke, *Numerical renormalization group method for quantum impurity systems*, Reviews of Modern Physics **80**, 395 (2008).

[67] A. C. Hewson, *The Kondo problem to heavy fermions*, Cambridge university press (1997).

[68] A. C. Seridonio, M. Yoshida, and L. N. Oliveira, *Thermal dependence of the zero-bias conductance through a nanostructure*, EPL **86**, 67006 (2009).

[69] M. Yoshida, A. C. Seridonio, and L. N. Oliveira, *Universal zero-bias conductance for the single-electron transistor*, Phys. Rev. B **80**, 235317 (2009).

[70] A. C. Seridonio, M. Yoshida, and L. N. Oliveira, *Universal zero-bias conductance through a quantum wire side-coupled to a quantum dot*, Phys. Rev. B **80**, 235318 (2009).

[71] L. N. Oliveira, M. Yoshida, and A. C. Seridonio, *Universal conductance for the Anderson model*, J. Phys. Conf. Ser. **200**, 052020 (2010).

[72] D. F. Aranguren-Quintero, E. Ramos, J. Silva-Valencia, M. S. Figueira, L. N. Oliveira, and R. Franco, *Universality and thermoelectric transport properties of quantum dot systems*, Phys. Rev. B **103**, 085112 (2021).

[73] X. Zianni, *Effect of electron-phonon coupling on the thermoelectric efficiency of single-quantum-dot devices*, Phys. Rev. B **82**, 165302 (2010).

[74] E. Ramos, J. Silva-Valencia, R. Franco, and M. S. Figueira, *The thermoelectric figure of merit for the single electron transistor*, Int. J. Thermal Sci. **86**, 387 – 393 (2014).

[75] C. J. Vineis, A. Shakouri, A. Majumdar, and M. G. Kanatzidis, *Nanostructured Thermoelectrics: Big Efficiency Gains from Small Features*, Adv. Mater. **22**, 3970 (2010).

[76] J. Friedel, *Metallic alloys*, Il Nuovo Cimento (1955-1965) **7**, 287–311 (1958).

[77] A. Heeger. *Localized moments and nonmoments in metals: the Kondo effect.* In *Solid state physics*, volume 23, pages 283–411. Elsevier, (1970).

[78] *The specific heat of pure copper and of some dilute copper-iron alloys showing a minimum in the electrical resistance at low temperatures*, (1961).

[79] J. Kondo, *Resistance minimum in dilute magnetic alloys*, Progress of theoretical physics **32**, 37–49 (1964).

[80] B. Matthias, M. Peter, H. Williams, A. Clogston, E. Corenzwit, and R. Sherwood, *Magnetic moment of transition metal atoms in dilute solution and their effect on superconducting transition temperature*, Physical Review Letters **5**, 542 (1960).

[81] D. Zubarev, *Double-time Green functions in statistical physics*, Sov. Phys. Usp **3**, 320–345 (1960).

[82] W. De Haas, J. De Boer, and G. Van den Berg, *The electrical resistance of gold, copper and lead at low temperatures*, Physica **1**, 1115–1124 (1934).

[83] W. De Haas and G. Van den Berg, *The electrical resistance of gold and silver at low temperatures*, Physica **3**, 440–449 (1936).

[84] C. Zener, *Interaction between the d shells in the transition metals*, Physical Review **81**, 440 (1951).

[85] H. Suhl, *Dispersion theory of the Kondo effect*, Physical Review **138**, A515 (1965).

[86] K. G. Wilson, *The renormalization group: Critical phenomena and the Kondo problem*, Reviews of modern physics **47**, 773 (1975).

[87] L. H. Thomas, *The motion of the spinning electron*, Nature **117**, 514–514 (1926).

[88] J. D. Jackson. *Classical electrodynamics*, (1999).

[89] J. J. Sakurai, *Advanced quantum mechanics*, Pearson Education India (1967).

[90] R. Winkler, S. Papadakis, E. De Poortere, and M. Shayegan, *Spin-Orbit Coupling in Two-Dimensional Electron and Hole Systems*, Springer (2003).

[91] G. Dresselhaus, *Spin-orbit coupling effects in zinc blende structures*, Physical Review **100**, 580 (1955).

[92] Y. A. Bychkov and É. I. Rashba, *Properties of a 2D electron gas with lifted spectral degeneracy*, JETP lett **39**, 78 (1984).

[93] F. J. Ohkawa and Y. Uemura, *Quantized surface states of a narrow-gap semiconductor*, Journal of the Physical Society of Japan **37**, 1325–1333 (1974).

[94] F. Mireles and G. Kirczenow, *Ballistic spin-polarized transport and Rashba spin precession in semiconductor nanowires*, Physical Review B **64**, 024426 (2001).

[95] F. Haldane, *Theory of the atomic limit of the Anderson model. I. Perturbation expansions re-examined*, Journal of Physics C: Solid State Physics **11**, 5015 (1978).

[96] B. A. Bernevig, J. Orenstein, and S.-C. Zhang, *Exact SU (2) symmetry and persistent spin helix in a spin-orbit coupled system*, Physical review letters **97**, 236601 (2006).

[97] A. Allerdt, A. E. Feiguin, and G. B. Martins, *Spatial structure of correlations around a quantum impurity at the edge of a two-dimensional topological insulator*, Phys. Rev. B **96**, 035109 (2017).

[98] G. D. Mahan, *Many-Particle Physics*, Plenum, NY **28**, 227 (1990).

[99] J. M. Ziman, *Principles of the Theory of Solids*, Principles of the Theory of Solids - Cambridge University Press , 229–239 (1999).

[100] We add a subscript e to the thermal conductivity, κ_e, to indicate that we refer to energy transport by electrons, excluding any contribution from phonons.

[101] B. Dong and X. Lei, *Effect of the Kondo correlation on the thermopower in a quantum dot*, Journal of Physics: Condensed Matter **14**, 11747 (2002).

[102] M. Foglio, T. Lobo, and M. Figueira, *General derivation of the Green's functions for the atomic approach of the Anderson model: application to a single electron transistor (SET)*, Aip Advances **2**, 5225 (2012).

[103] P. Anderson, *A poor man's derivation of scaling laws for the Kondo problem*, Journal of Physics C: Solid State Physics **3**, 2436 (1970).

[104] H. Krishna-Murthy, J. Wilkins, and K. Wilson, *Renormalization-group approach to the Anderson model of dilute magnetic alloys. I. Static properties for the symmetric case*, Physical Review B **21**, 1003 (1980).

[105] R. Bulla, N.-H. Tong, and M. Vojta, *Numerical Renormalization Group for Bosonic Systems and Application to the Sub-Ohmic Spin-Boson Model*, Phys. Rev. Lett. **91**, 170601 (2003).

[106] M. Sindel. *Numerical Renormalization Group studies of Quantum Impurity Models in the Strong Coupling Limit*. PhD thesis, lmu, (2005).

[107] R. Bulla, T. Pruschke, and A. Hewson, *Anderson impurity in pseudo-gap Fermi systems*, Journal of Physics: Condensed Matter **9**, 10463 (1997).

[108] J. K. Cullum and R. A. Willoughby, *Lanczos algorithms for large symmetric eigenvalue computations: Vol. I: Theory*, SIAM (2002).

[109] R. Žitko, *SNEG – Mathematica package for symbolic calculations with second-quantization-operator expressions*, Computer Physics Communications **182**, 2259 – 2264 (2011).

[110] K. Ingersent, *Behavior of magnetic impurities in gapless Fermi systems*, Physical Review B **54**, 11936 (1996).

[111] V. L. Campo Jr and L. N. Oliveira, *Alternative discretization in the numerical renormalization-group method*, Physical Review B **72**, 104432 (2005).

[112] T. Pruschke et al., *Energy resolution and discretization artifacts in the numerical renormalization group*, Physical Review B **79**, 085106 (2009).

[113] F. Haldane, *Scaling theory of the asymmetric Anderson model*, Physical Review Letters **40**, 416 (1978).

[114] M. A. Manya, G. B. Martins, and M. S. Figueira. *Spin-orbit coupling effects over thermoelectric transport properties in quantum dots*, (2021).

[115] The meaning of this statement is the following: the choice of V is such that the *zero-SOC* hybridization function at the Fermi energy, Γ_0, is 0.007 [see Eq. (7.3)]. This same V is used for the finite-SOC calculations, resulting in a hybridization that decreases with SOC (see Fig. 7.4).

[116] Our unit of energy will be the half-bandwidth at zero-SOC, i.e., $D_0 = 1$.

[117] D. Vollhardt, *Characteristic crossing points in specific heat curves of correlated systems*, Physical review letters **78**, 1307 (1997).

[118] T. A. Costi and A. C. Hewson, *Transport coefficients of the Anderson model*, J. Phys.: Condens. Matter **5**, L361 (1993).

[119] N. Xu, P. K. Biswas, J. H. Dil, R. S. Dhaka, G. Landolt, S. Muff, C. E. Matt, X. Shi, N. C. Plumb, M. Radović, E. Pomjakushina, K. Conder, A. Amato, S. V. Borisenko, R. Yu, H.-M. Weng, Z. Fang, X. Dai, J. Mesot, H. Ding, and M. Shi, *Direct observation of the spin texture in SmB6 as evidence of the topological Kondo insulator*, Nat. Commun. **5**, 4566 (2014).

[120] G.-B. Zhu and H.-M. Yang, *Transport properties of the topological Kondo insulator SmB6 under the irradiation of light*, Chin. Phys. B **25**, 107303 (2016).

[121] L. Li, K. Sun, C. Kurdak, and J. W. Allen, *Emergent mystery in the Kondo insulator samarium hexaboride*, Nat. Rev. Phys. **2**, 463 (2020).

[122] D.-C. Ryu, C.-J. Kang, J. Kim, K. Kim, G. Kotliar, J.-S. Kang, J. D. Denlinger, and B. I. Min, *Topological surface states on the nonpolar (110) and (111) surfaces of* SmB_6, Phys. Rev. B **103**, 125101 (2021).

[123] W. Greiner et al., *Relativistic quantum mechanics*, Springer (1990).

[124] V. M. Edelstein, *Magnetoelectric effect in polar superconductors*, Physical review letters **75**, 2004 (1995).